

A014 412

NRL Report 7914

Creeping Waves and Lateral Waves in Acoustic Scattering by Large Elastic Cylinders

GEORGE VLADIMIR FRISK

*Propagation Branch
Acoustics Division*

July 1, 1975



NAVAL RESEARCH LABORATORY
Washington, D.C.

Approved for public release; distribution unlimited.

This dissertation was approved by

Wm as director

and by *Thomas J. Eiser* and

Frank Anderson as readers.

This report is a facsimile of a dissertation submitted in partial fulfillment
of the requirements for the degree of Doctor of Philosophy in the Graduate
School of Arts and Sciences, Catholic University of America, 1975.

UNCLASSIFIED

SECURITY CLASSIFICATION OF THIS PAGE (When Data Entered)

DD FORM 1 JAN 73 1473

EDITION OF 1 NOV 65 IS OBSOLETE
S/N 0102-014-6601

UNCLASSIFIED

i SECURITY CLASSIFICATION OF THIS PAGE (When Data Entered)

UNCLASSIFIED

SECURITY CLASSIFICATION OF THIS PAGE (When Data Entered)

the Rayleigh and Stoneley waves on a flat elastic half-space, while the Franz mode wave numbers tend toward the wave number of sound in the fluid. The longitudinal and transverse Whispering Gallery mode wave numbers tend toward the longitudinal and transverse wave numbers in the solid. Graphical results are presented for an aluminum cylinder in water (and in one case, also in vacuum) and show good agreement with existing numerical results.

Then, using the Watson-Sommerfeld transformation, the limiting behavior of the solution to the problem of the scattering of a cylindrical wave from a cylinder whose radius tends to infinity is investigated. Using the analytic expressions for the creeping wave numbers, it is shown that the residue sums corresponding to the different classes of circumferential waves tend individually toward the different types of surface waves found on the flat surface.

UNCLASSIFIED

ii SECURITY CLASSIFICATION OF THIS PAGE (When Data Entered)

Table of Contents

	<u>Page</u>
Introduction	1
Chapter I. Surface Wave Modes on Elastic Cylinders	4
A. The Rayleigh Zero	7
B. The Stoneley Zero	10
C. The Franz Zeros	13
D. The Whispering Gallery Zeros	19
1. The Transverse Whispering Gallery Zeros	19
2. The Longitudinal Whispering Gallery Zeros	22
E. Discussion of Results	25
Chapter II. The Scattering of a Cylindrical Wave by a Large, Solid Elastic Cylinder	30
A. The Residue Sum P_2	34
B. The Residue Sum P_1	37
Conclusions	46
Appendix A. Asymptotic Expansions of Cylinder Functions	48
Appendix B. The Reflection of a Cylindrical Wave at a Plane Fluid-Solid Interface	53
Appendix C. Creeping Waves and Lateral Waves for the Fluid Cylinder	57
List of Illustrations	59
Illustrations	64
Bibliography	92

Dedication

This dissertation is dedicated to the memory of my father, Vladimir George Frisk.

Acknowledgments

I am grateful for the grant of an Edison Memorial Fellowship at the Naval Research Laboratory, under which most of this work was performed. I would like to thank Mr. Burton G. Hurdle, Head of the Propagation Branch, and Mr. Kenneth D. Flowers, Head of the Scattering Section in the Acoustics Division at the Naval Research Laboratory, for their cooperation and encouragement. The interest and cooperation of Professor Frank A. Andrews [Captain, U. S. Navy (Ret.)], Director of the Catholic University Interdisciplinary Acoustics Program, are also acknowledged. I am indebted to Mrs. Diane O'Neill for her patient and careful typing of the manuscript. Above all, I would like to express my sincere gratitude to Professor Herbert Überall for his patient guidance, constant encouragement, and constructive criticism in the preparation of this dissertation.

Introduction

Phenomena of acoustic reflection on plane boundaries between fluid and elastic media have been studied in the literature both theoretically and experimentally.^{1,2} A striking feature is the appearance of the so-called Rayleigh wave, a surface wave generated in the elastic medium at a critical angle of incidence, and propagating with a speed usually below and close to the shear wave speed in the solid. Most of its energy is concentrated in the solid near the boundary, but part of it leaks into the fluid, causing an attenuation (complex wave number) in the propagation direction along the surface.

An additional type of surface wave was shown to exist by Stoneley.³ This wave has a propagation speed close to that of sound in the fluid, is unattenuated in the direction of propagation, and most of its energy is concentrated in the fluid along the boundary.

In addition to these genuine surface waves, there also exist two types of lateral waves on a flat boundary between solid and fluid, which propagate with the compressional and shear speeds, respectively, of bulk waves in the solid.¹

Scattering from solid elastic cylinders has been investigated by means of the Watson-Sommerfeld transformation applied to the normal-mode series.^{1,4} In this case, one finds "creeping waves" with a surface wave type behavior, divided into two classes: those with speeds close to the elastic bulk speeds

(Rayleigh and Whispering Gallery waves), and those with speeds close to the sound speed in the fluid (Stoneley and Franz waves). Previously, the Rayleigh and Stoneley-type waves (i.e., those tending toward the Rayleigh and Stoneley waves in the flat limit) were studied by Grace and Goodman⁵ and by Lapin⁶ by analytic methods, while numerical discussions of the Rayleigh and Whispering Gallery modes (higher order modes which arise because of the curvature of the surface) were given by Dcolittle, et al.⁴ The latter authors also treated the Franz waves,⁷ i.e., higher order modes in the fluid which arise because of the curvature of the boundary (and which also exist on an impenetrable surface).

In the present work, we shall establish the connection between creeping wave and flat surface wave theory by investigating the limit of acoustic scattering from an elastic cylinder whose radius tends to infinity. In Chapter I, we calculate the behavior of the circumferential wave modes for large cylinder radii. Accordingly, the appropriate Debye- or Airy-type asymptotic expansions for the cylinder functions are used to solve the secular determinant for the complex surface wave numbers. Numerical results for the Rayleigh, Stoneley, Franz, and Whispering Gallery wave numbers are obtained as a function of fluid wave number times cylinder radius for a solid aluminum cylinder in water, and in one case, also in vacuum. In Chapter II, using the Watson-Sommerfeld transformation, we examine the behavior of the solution for the problem of a cylinder scattering radiation from a line source in the fluid as the cylinder radius tends to infinity. In this limit, the residue sums corresponding to

the different classes of circumferential waves found in Chapter I are shown to tend individually toward the different types of surface waves found on the flat surface. In this way, the transition of creeping wave to surface wave theory, as the scattering object tends toward a flat surface, is established.

Chapter I. Surface Wave Modes on Elastic Cylinders

The complex wave numbers of circumferential waves on an elastic cylinder in a fluid are obtained as the roots of a 3×3 determinant which may be derived in various ways. One way consists in assuming interior and exterior solutions in a form describing circumferential propagation⁸ [with a time factor $\exp(-i\omega t)$ suppressed]:

$$\Psi = \Psi_y^{(\omega)} e^{iy\phi} J_y(k_L r) \quad (1a)$$

$$A_z = A_y^{(\omega)} e^{iy\phi} J_y(k_T r) \quad (1b)$$

and

$$\Phi = \Phi_y^{(\omega)} e^{iy\phi} H_y^{(1)}(kr) \quad (1c)$$

where Ψ , A_z are the elastic potentials and Φ is the velocity potential in the fluid; k is the acoustic wave number in the fluid, and k_L and k_T are the wave numbers of bulk longitudinal (compressional) and transverse (shear) waves in the solid, respectively. Matching boundary conditions on the cylinder surface⁵ then leads to the secular determinant. Alternately, when the problem of sound scattering by a cylinder is solved using the Watson-Sommerfeld transformation,⁴ the same determinant appears in the denominator of the scattered field, and its zeros give pole-type contributions which represent

circumferential waves. The scattering problem is discussed in Chapter II.

The determinant in question, as a function of ν , is⁴ given by

$$D(\nu) = \begin{vmatrix} a^2 H_y^{(1)}(x) & \alpha_y^{L1} & \alpha_y^{T1} \\ x H_y^{(1)'}(x) & \alpha_y^{L2} & \alpha_y^{T2} \\ 0 & \alpha_y^{L3} & \alpha_y^{T3} \end{vmatrix} \quad (2a)$$

where

$$\alpha_y^{L1} = x_L^2 [\lambda J_y(x_L) - 2\mu J_y''(x_L)]$$

$$\alpha_y^{L2} = \rho_1 \omega^2 x_L J_y'(x_L)$$

$$\alpha_y^{L3} = 2\nu [J_y(x_L) - x_L J_y'(x_L)] \quad (2b)$$

$$\alpha_y^{T1} = 2\mu\nu [J_y(x_T) - x_T J_y'(x_T)]$$

$$\alpha_y^{T2} = \rho_1 \omega^2 y J_y(x_T)$$

$$\alpha_y^{T3} = -x_T^2 [J_y(x_T) + 2 J_y''(x_T)]. \quad (2c)$$

Here, a is the cylinder radius; $x = ka = \omega a/c$ where c is the sound velocity in the fluid; $x_{L,T} = k_{L,T} a = \omega a/c_{L,T}$ where $c_{L,T}$ are the bulk elastic velocities

$$c_L^2 = (\lambda + 2\mu)/\rho_2, \quad c_T^2 = \mu/\rho_2 \quad (3)$$

that depend on the Lamé constants λ, μ and on the density ρ_2 of the cylinder material, while ρ_1 is the density of the ambient fluid. The primes on the cylinder functions denote derivatives with respect to their argument.

Our subsequent analysis shows the existence of different classes of zeros, corresponding to physically different types of surface waves which have been classified in the Introduction.

Each complex root $\nu = \nu_r + i\nu_i$ of the equation $D(\nu) = 0$, inserted in Eqs. (1), yields a circumferential wave with wave number ν/a , phase velocity $C = \omega a / \nu_r$ and linear attenuation ν_i/a . Excitation and re-radiation of these surface waves take place at a critical angle θ given by $\sin \theta = C/C$.

We shall be concerned with the case of large cylinder radii, or large values of the parameters ν , $x (\gtrsim 10)$, x_L and x_T . For this purpose, it will be necessary to utilize asymptotic expansions of the cylinder functions, which assume different forms in different regions of the complex ν -plane, mainly separated by anti-Stokes lines. In our case, the appropriate division of the complex ν -plane is shown in Figure 1. Only zeros in the first quadrant need to be considered, those in the second and fourth quadrant leading to exponentially increasing waves, and those in the third quadrant differing from those in the first only in their sense of circumnavigation. Regions 1-4 are separated by the anti-Stokes lines of $H_\nu^{(1)}(x_L)$, $H_\nu^{(0)}(x_T)$, and $H_\nu^{(0)}(x)$, respectively, on which also the zeros of these functions and of their derivatives are located. The circles, with radii determined by

$$|\nu - x_i| = \delta(x_i^{1/3}), \quad |\nu - x| = \delta(x^{1/3}) \quad (4)$$

($x_i = x_L$ or x_T), define regions within which Airy-type asymptotic expansions are more accurate. Outside, Debye-type expansions are appropriate; of these, transition-type forms must be used near their corresponding anti-Stokes lines.

In addition, anti-Stokes lines for $J_\nu(x_{L,T})$ originate at $x_{L,T}$ and run along the real axis to the left, with the zeros of $J_\nu(x_{L,T})$ being located along them.

In the following, we shall consider physically different types of surface waves, corresponding to different types of zeros of $D(\nu)$ in an individual fashion.

IA. The Rayleigh Zero

In the limiting case of the cylinder radius $a \rightarrow \infty$, corresponding to the case of a flat elastic half-space bounded by a fluid, the speed C_R of the Rayleigh wave is known for practical cases to lie somewhat below the speed C_T of the elastic shear bulk wave.¹ The corresponding zero ν_R of $D(\nu)$, in the case of large but finite radius of curvature, will then lie to the right of x_T in Figure 1, with an imaginary part that puts it above the real axis. In this case, the appropriate asymptotic expansions of all the cylinder functions appearing in $D(\nu)$ are of Debye type; cf. Appendix A.

Equation (2a) when set equal to zero, can in general be rewritten in the form

$$x h(x) = a^2 \rho_i \omega^2 \left\{ x_L x_T^2 f(x_L) [1 + 2g(x_T)] + 2\nu^2 [1 - x_L f(x_L)] \right\} / \left\{ x_L^2 x_T^2 [\lambda - 2\mu g(x_L)] [1 + 2g(x_T)] + 4\mu \nu^2 [1 - x_L f(x_L)] [1 - x_T f(x_T)] \right\} \quad (5)$$

where

$$f(x_i) = J_\nu'(x_i) / J_\nu(x_i), \quad (6a)$$

$$g(x_i) = J_\nu''(x_i) / J_\nu(x_i) \quad (6a)$$

$$\equiv -\left(1/x_i\right) f(x_i) + \left(\nu/x_i\right)^2 - 1, \quad (6b)$$

$$h(x) = H_y^{(1)}(x)/H_y^{(0)}(x) . \quad (6c)$$

If the appropriate Debye expansions of Appendix A are inserted, we obtain

$$f(x_i) \sim (\xi_i^2 - 1)^{1/2} + \frac{1}{2(\xi_i^2 - 1)x_i} + \frac{1}{8(\xi_i^2 - 1)^{3/2}x_i^2} \left[1 - \frac{5\xi_i^2}{(\xi_i^2 - 1)} \right] + \mathcal{O}(x_i^{-3}) \quad (7a)$$

$$g(x_i) \sim \xi_i^2 - 1 - \frac{(\xi_i^2 - 1)^{1/2}}{x_i} - \frac{1}{2(\xi_i^2 - 1)x_i^2} + \mathcal{O}(x_i^{-3}) \quad (7b)$$

$$h(x) \sim i(1 - \xi^2)^{1/2} - \frac{1}{2(1 - \xi^2)x} + \frac{i}{8(1 - \xi^2)^{3/2}x^2} \left[1 - \frac{5\xi^2}{(1 - \xi^2)} \right] + \mathcal{O}(x^{-3}) \quad (7c)$$

where $\xi_i = v/x_i$, $\xi = \gamma/x$ both being $\sim \mathcal{O}(1)$. Using these expansions and calculating Eq. (5) to lowest order in x_i , writing $v = k_R a + \mathcal{O}(1)$ yields the well-known generalized Rayleigh equation for the flat half-space bounded by a fluid,¹

$$\left[1 - 2\left(\frac{k_R}{k_T}\right)^2 \right]^2 - 4\frac{k_R^2}{k_T^2} \left(\frac{k_R^2}{k_T^2} - \frac{k_L^2}{k_T^2} \right)^{1/2} \left(\frac{k_R^2}{k_T^2} - 1 \right)^{1/2} = -i \frac{\rho_1}{\rho_2} \frac{(k_R^2 - k_L^2)^{1/2}}{(k^2 - k_R^2)^{1/2}} \quad (8)$$

which has as one solution the (complex) Rayleigh wave number $k_R = \omega/c_R$ to be considered in this section.

The behavior of the Rayleigh wave number k_R on a cylindrically curved surface of large radius of curvature is obtained by retaining terms of order x_i^{-1} in Eq. (5) when inserting Eqs. (7) into it. With an iterative procedure that starts from the flat-limit Rayleigh wave number

$$k_{R'} = k_R + (\epsilon_R/a) + \mathcal{O}(a^{-2}) \quad (9)$$

the result for ϵ_R is found as

$$\begin{aligned} \epsilon_R = & \left\{ -8 \frac{\rho_2}{\rho_1} \frac{kk_R}{k_T^4} \left[k_T^2 - 2k_R^2 + \chi_{RL}\chi_{RT} + \frac{1}{2} k_R^2 \left(\frac{\chi_{RT}}{\chi_{RL}} + \frac{\chi_{RL}}{\chi_{RT}} \right) \right] \right. \\ & \left. + i \frac{kk_R}{\chi_R} \left(\frac{\chi_{RL}}{\chi_R^2} + \frac{1}{\chi_{RL}} \right) \right\}^{-1} \\ & \times \left\{ -\frac{1}{2} k^3 \frac{\chi_{RL}}{\chi_R^4} - 2 \frac{\rho_2}{\rho_1} \frac{k}{k_T^2} \left[\chi_{RT} + \chi_{RL} - \frac{k_R^2 \chi_{RL}}{\chi_{RT}^2} - \frac{k_L^2 k_R^2 \chi_{RT}}{k_T^2 \chi_{RL}^2} \right] \right. \\ & \left. + 2i \frac{k_L}{\chi_R} \left[\frac{kk_R^2}{k_L k_T^2} - \frac{kk_L}{4\chi_{RL}^2} - \frac{k}{k_L k_T^2} \chi_{RL} \chi_{RT} \right] \right\} \end{aligned} \quad (10a)$$

where

$$\chi_{Ri} = (k_R^2 - k_i^2)^{1/2}, \quad \chi_R = (k^2 - k_R^2)^{1/2} \quad (10b)$$

($i=L, T$). This agrees with an expression obtained previously by Lapin⁶. The derivation of Eq. (10a) involved expansions which are valid under the conditions

$$\left| \frac{\epsilon_R}{ka} \right| < \frac{1}{2} \frac{k_i}{k} \left| \frac{k_R}{k_i} - \frac{k_i}{k_R} \right|, \quad (10c)$$

$$\left| \frac{\epsilon_R}{ka} \right| < \frac{1}{2} \left| \frac{k_R}{k} - \frac{k}{k_R} \right|. \quad (10d)$$

Of these, the case $k_i = k_T$ is most stringent because of the proximity of k_R to k_T in physical cases of interest.

For the case of a solid aluminum cylinder in water ($c=1493$ m/sec, $c_L = 6420$ m/sec, $c_T = 3040$ m/sec, $\rho_1 = 1$ g/cm³, $\rho_2 = 2.7$ g/cm³), we calculated the flat Rayleigh limit by solving Eq. (8) numerically, with the result

$$k_R/k = 0.522 + 0.0155i \quad (11)$$

Subsequently, we calculated ϵ_R from Eq. (10a), using this value for k_R . The results are shown in Figure 2, where the trajectory of k_R/k as a function of the parameter ka is plotted as crosses in the complex plane. The conditions of Eq. (10c) would indicate that the most reliable results are those for $ka \geq 70$. Also shown in the figure are points of the trajectory obtained by Uginčius^{4,9} who used convergent expansions of the cylinder functions for $ka \leq 25$, and Debye expansions for $ka > 25$ for a numerical evaluation of the roots when Eq. (2a) is set equal to zero.

The present results, for large values of ka , appear to be a natural continuation of Uginčius' zero trajectory, while the present low- ka values might be less reliable because of the approximations used as mentioned. Note that our results were obtained as an expansion away from the Rayleigh limit, while those of Uginčius tend towards it without having assumed it as a limit.

It might be noted that in the limit of an elastic cylinder in a vacuum ($\rho, \rightarrow 0$), the flat Rayleigh wave number k_R as well as the correction term ϵ_R become purely real, indicating no radiative losses of the Rayleigh wave in this case.

IB. The Stoneley Zero

In the limit of the flat elastic half-space, the other solution of Eq. (8) of physical interest is the Stoneley zero,³ a real root corresponding to a speed somewhat less than the speed of sound in the fluid.¹ Accordingly, in order to obtain

an extension of the Stoneley zero to the case of a finitely curved cylinder, the transition-Debye asymptotic forms (as outlined in Appendix A) were used in the left-hand side of Eq. (5) because of the expected vicinity of the zero to the anti-Stokes line between Regions 3 and 4 of Figure 1. Debye forms, rather than Airy forms which are more appropriate in the circle of Region 7, are used since we again want to obtain the Stoneley zero in the curved case by expanding about the known flat-limit Stoneley zero. Sufficiently close to zero curvature, the radius of the Airy circle in the ν/ka plane ("reduced plane") becomes small enough for the Stoneley zero to lie outside of it. (Even inside the circle, Debye forms are not incorrect; they just become less accurate).

Ordinary (non-transition) Debye expansions were used for the other cylinder functions in Eq. (5), so that the same expressions as in Eqs. (7a, b) were inserted in Eq. (5). However, the transition-Debye expansion

$$H_{\nu}^{(0)}(x) \sim \left(\frac{2}{\pi}\right)^{1/2} (y^2 - x^2)^{-1/4} \left\{ e^{-(y^2 - x^2)^{1/2} - \nu \cosh^{-1} \nu/x} - i e^{-(y^2 - x^2)^{1/2} + \nu \cosh^{-1} \nu/x} \right\} \left\{ 1 + \theta(x^{-1}) \right\} \quad (12)$$

leads to the expression

$$h(x) \sim -(\xi^2 - 1)^{1/2} + \frac{1}{2(\xi^2 - 1)x} + \theta(x^{-2}) + 2i(\xi^2 - 1)^{1/2} e^{2(y^2 - x^2)^{1/2} - 2\nu \cosh^{-1} \nu/x} \quad (13)$$

now to be used in Eq. (5). Retention of the lowest-order subdominant part in the transition-Debye form yields the exponential in Eq. (13).

Using an approach analogous to that for the Rayleigh zero, we find the Stoneley wave number $k_{s'}$ as

$$k_{s'} = k_s + (\epsilon_s/a) + \mathcal{O}(a^{-2}) \quad (14)$$

where k_s is the flat-limit wave number, and where

$$\begin{aligned} \epsilon_s = & \left\{ -8 \frac{\rho_2}{\rho_1} \frac{hk_s}{k_T^4} \left[k_T^2 - 2k_s^2 + \chi_{SL}\chi_{ST} + \frac{1}{2} k_s^2 \left(\frac{\chi_{ST}}{\chi_{SL}} + \frac{\chi_{SL}}{\chi_{ST}} \right) \right] \right. \\ & \left. + \frac{hk_s}{\chi_s} \left(\frac{\chi_{SL}}{\chi_s^2} + \frac{1}{\chi_{SL}} \right) \right\}^{-1} \left\{ -\frac{k^3}{2} \frac{\chi_{SL}}{\chi_s^4} - 2 \frac{\rho_2}{\rho_1} \frac{k}{k_T^2} [\chi_{ST} + \chi_{SL} \right. \\ & \left. - \frac{k_s^2 \chi_{SL}}{\chi_{ST}^2} - \frac{k_L^2 k_s^2 \chi_{ST}}{k_T^2 \chi_{SL}^2}] + 2 \frac{k_L}{\chi_s} \left[\frac{hk_s^2}{k_L k_T^2} - \frac{hk_L}{4\chi_{SL}^2} - \frac{k}{k_L k_T^2} \chi_{SL} \chi_{ST} \right] \right. \\ & \left. - 2ika \frac{\chi_{SL}}{\chi_s} e^{-2k_s a [\tanh^{-1}(\chi_s/k_s) - (\chi_s/k_s)]} \right\}, \end{aligned} \quad (15a)$$

with

$$\chi_{s_i} = (k_s^2 - k_i^2)^{1/2}, \quad \chi_s = (k_s^2 - k^2)^{1/2} \quad (15b)$$

($i = L, T$). This expression differs from a previous one given by Lapin⁶ in some details. It is valid under conditions similar to Eqs. (10c, d) with k_R replaced by k_s ; the most stringent one is the analog of Eq. (10d).

It is important to note that the only imaginary correction term to the (real) Stoneley wave number for the flat case is the exponential in Eq. (15a), which resulted from retaining the subdominant term in the transition-Debye expansion of $H_y^{(1)}(x)$. Physically, it corresponds to the fact

that on a cylinder the Stoneley wave radiates off tangentially into the surrounding fluid while on a flat surface, its wave number is real and it cannot radiate off any energy.

For the solid aluminum cylinder in water, we solved Eq. (8) numerically and obtained

$$k_s/k = 1.0025 \quad (16)$$

which agrees with earlier results.¹⁰ Inserting into Eq. (15a) yields the points presented in Figure 3, plotted as a trajectory in the complex k_s/k plane with values of ka as a parameter. The imaginary scale of the figure is greatly expanded because of the smallness of the imaginary part of the zero. Due to the mentioned conditions of validity of the approximations, the points in the horizontal portion of the figure may not be numerically reliable. It should be noted that Lapin's⁶ formula would give the imaginary parts of the Stoneley zeros only half as large as given by us, but we believe this to be due to an error in Lapin's printed expression.

IC. The Franz Zeros

This type of zeros arises due to the finite curvature of the surface, and therefore exists even in the case of impenetrable objects. The corresponding surface waves get on and off the surface tangentially,¹ and they are no longer present in the limit of a flat surface. Therefore, one cannot expand the positions of the zeros about the flat limit, as had been done in the preceding sections. Instead, we shall expand about the known positions of the zeros for either a soft or a rigid

cylinder with finite curvature. The latter are given by the complex zeros of $H_{\nu}^{(n)}(x)$ or $H_{\nu}^{(n)}(x)$, respectively,⁷ which are located along the anti-Stokes line between Regions 3 and 4 in Figure 1. Explicitly, they are¹¹ ($n = 1, 2, \dots$):

$$\nu_{\text{rigid},n} = x - \bar{\eta}_n e^{i\pi/3} (x/2)^{1/3} + e^{i2\pi/3} \left[\bar{\eta}_n^2/60 - 1/(10\bar{\eta}_n) \right] (2/x)^{1/3} + \theta(x^{-1}) \quad (17a)$$

$$\nu_{\text{soft},n} = x - \eta_n e^{i\pi/3} (x/2)^{1/3} + e^{i2\pi/3} (\eta_n^2/60) (2/x)^{1/3} + \theta(x^{-1}) \quad (17b)$$

where η_n are the zeros of the Airy function, and $\bar{\eta}_n$ those of its derivative:

$$Ai(\eta_n) = 0, \quad Ai'(\bar{\eta}_n) = 0. \quad (17c)$$

For the case of the elastic cylinder, we use the ordinary Debye expansions for the cylinder functions in $f(x_i)$, $g(x_i)$ of Eqs. (6), but the Airy-type asymptotic expansions (Appendix A) for $h(x)$. The latter are valid inside the circle of Region 7 in Figure 1 and had also been used to obtain Eqs. (17), but the results link up smoothly with those for the zeros outside the circle, in the transition region between Regions 3 and 4 where transition Debye expansions are used.¹² In fact, in the reduced ν/ka plane, the radius of the circle shrinks with increasing ka at the same rate at which the zeros tend towards its center.

One finds in this way:¹³

$$h(x) \sim -\frac{1}{3x} + \frac{1}{P} \frac{\partial P}{\partial x} - e^{-i\pi/3} \frac{\partial g}{\partial x} \frac{Ai'(-qe^{-i\pi/3})}{Ai(-qe^{-i\pi/3})} + \theta(x^{-1-2m/3}) \quad (18)$$

with ρ, q and m defined in Appendix A. When this is substituted in Eq. (5), we obtain the equation

$$Ai'(-q e^{-i\pi/3})/Ai(-q e^{-i\pi/3}) = \Gamma \quad (19a)$$

where

$$\begin{aligned} \Gamma = & -\frac{e^{i\pi/3}}{\partial q/\partial x} \left[-(\rho_1 c c_L/\delta) (\xi_L^2 - 1)^{1/2} + (1/3x) - \frac{1}{\rho} \frac{\partial \rho}{\partial x} \right] \\ & + \mathcal{O}(x^{-1/3}) \end{aligned} \quad (19b)$$

and

$$\begin{aligned} \delta = & \rho_2 \left\{ -(1 - 2\xi_T^2)(c_L^2 - 2c_T^2\xi_L^2) \right. \\ & \left. + 4c_T^2\xi_L\xi_T [(\xi_L^2 - 1)(\xi_T^2 - 1)]^{1/2} \right\}. \end{aligned} \quad (19c)$$

The method to be used for solving Eq. (19a) will depend on the magnitude of Γ . Using Eqs. (A8) and the relations

$$\begin{aligned} y &= x + \mathcal{O}(x^{1/3}) \\ (\partial q/\partial x)^{-1} &= -(x/2)^{1/3} + \mathcal{O}(x^{-1/3}), \end{aligned}$$

we obtain from Eq. (19b), to lowest order in the quantity $x^{-1/3}$:

$$\Gamma = \mathcal{O}(x^{1/3} \alpha_{L,T}^2 \rho_1/\rho_2) \quad (20)$$

where $\alpha_i = k_i/k$ ($i=L,T$). For typical fluid-solid interfaces one has $\alpha_L^2 \rho_1/\rho_2 < 0.1$, so that $\Gamma < 1$ for $x = x_c \sim 10^3$ (for an aluminum cylinder in water, $x_c \approx 6000$). In this case, we follow a method of Streifer and Kodis¹³⁻¹⁵ and, letting $\eta = -q e^{-i\pi/3}$, we expand $Ai'(\eta)$ and $Ai(\eta)$ about $\bar{\eta}_n$, defined in Eq. (17c) as the zeros of $Ai'(\eta)$. Subsequently, the quantity $\eta - \bar{\eta}_n$ is expanded in powers of $W \equiv -i\Gamma \exp(-i\pi/3)$, and we obtain

from Eq. (19a) :

$$g(x, y) = -\bar{\eta}_n e^{i\pi/3} + i e^{-i\pi/3} W/\bar{\eta}_n + \frac{1}{2} W^2/\bar{\eta}_n^3 - i e^{i\pi/3} W^3 \left[\frac{1}{(3\bar{\eta}_n^2)} + \frac{1}{(2\bar{\eta}_n^5)} \right] + \mathcal{O}(x^{-4/3}). \quad (21)$$

Using Eq. (A8d), an iterative solution of this equation gives the result for the Franz wave numbers (labeled by $n = 1, 2, \dots$) :

$$k_{Fn} = \gamma_{Fn}/\alpha \quad (22a)$$

where

$$\begin{aligned} \gamma_{Fn} = & x - \bar{\eta}_n e^{i\pi/3} \left(\frac{x}{2} \right)^{1/3} + \frac{e^{2i\pi/3}}{10} \left(\frac{\bar{\eta}_n^2}{6} - \frac{1}{\bar{\eta}_n} \right) \left(\frac{2}{x} \right)^{1/3} \\ & + \frac{z}{\bar{\eta}_n} e^{-i\pi/3} \left(\frac{x}{2} \right)^{2/3} - \frac{z^2}{2\bar{\eta}_n^3} \left(\frac{x}{2} \right) \\ & + z \left[\frac{1}{10} \left(1 - \frac{1}{\bar{\eta}_n^3} \right) - \frac{t}{5} - \frac{k^2}{2\chi_L^2} \right] \\ & + z^3 e^{i\pi/3} \left(\frac{1}{3\bar{\eta}_n^2} + \frac{1}{2\bar{\eta}_n^5} \right) \left(\frac{x}{2} \right)^{4/3} + \mathcal{O}(x^{-1}), \quad (x < x_c) \end{aligned} \quad (22b)$$

with

$$\chi_i = (k^2 - k_i^2)^{1/2} \quad (i = L, T) \quad (22c)$$

$$z = \frac{\rho_1}{\rho_2} \frac{\alpha_T^4}{s} \frac{\chi_L}{k} \quad (22d)$$

$$s = \alpha_T^4 - 4\alpha_T^2 + 4 - 4\chi_L \chi_T / k^2 \quad (22e)$$

$$t = 4\alpha_T^2 - 8 + 4\chi_L \chi_T / k^2 + 2k^2 \frac{(2 - \alpha_L^2 - \alpha_T^2)}{\chi_L \chi_T}. \quad (22f)$$

This result was arrived at after one iteration, assuming that $\alpha_L < \alpha_T < 1$, and that $z = \mathcal{O}(x^{-2/3})$. These conditions are

met for the material parameters of typical fluid-solid cases. Accordingly, the above asymptotic expression for γ_{F_n} constitutes a series whose terms decrease as powers of $x^{-1/3}$.

Note that in Eq. (22b), the first three terms agree exactly with those of the rigid zeros, Eq. (17a), and that the material properties enter only through higher-order terms.

As in the previous cases of the Rayleigh and Stoneley zeros, the binomial expansions used in obtaining Eqs. (22a, b) are valid under the conditions

$$x > 2 \left| \bar{\eta}_n / (1 - \alpha_i^2) \right|^{3/2}, \quad (23a)$$

$$x > 2 \left| 2\bar{\eta}_n / 15 \right|^{3/2}, \quad (23b)$$

$$x > 2 \left| \bar{\eta}_n t / s \right|^{3/2}. \quad (23c)$$

They impose lower limits on x , depending on the order of the zero. In practice, these are found not to be very stringent, the most stringent one being Eq. (23a) with $i=T$. In fact, the lower limits of validity were found to be as low as ka^3 for F1, and e.g. ka^60 for F5, for an aluminum cylinder in water.

Equation (22b) will be a useful expansion for a large range of x , as long as the numerical value of z is such that subsequent terms decrease. However, if x becomes very large, $x > x_c$ (including the flat limit $x \rightarrow \infty$), we will have $\Gamma > 1$ from Eq. (20). In this case, we expand $Ai'(\eta)$ and $Ai(\eta)$ in Eq. (19a) about η_n , i.e., about the zeros of $Ai(\eta)$ defined in Eq. (17c).

Then, the quantity $\eta - \eta_n$ may be expanded in powers of $1/W$, yielding

$$g(x, y) = -\eta_n e^{i\pi/3} + iW^{-1} + (i\eta_n/3) e^{i\pi/3} W^{-3} + O(x^{-4/3}). \quad (24)$$

Using Eq. (A8d) and iterating again, we obtain for the Franz wave numbers Eq. (22a) with

$$\begin{aligned} \gamma_{Fn} = & x - \eta_n e^{i\pi/3} \left(\frac{x}{2}\right)^{1/3} + \frac{\eta_n^2}{60} e^{i2\pi/3} \left(\frac{2}{x}\right)^{1/3} - \frac{1}{z} \\ & + \frac{\eta_n e^{i\pi/3}}{z} \left[-\frac{t}{s} + \frac{1}{6} - \frac{k^2}{2\chi_L^2} + \frac{1}{3z^2} \right] \left(\frac{z}{x}\right)^{2/3} + O(x^{-1}), \end{aligned} \quad (x > x_c) \quad (25)$$

which was arrived at after one iteration, assuming $\alpha_L \ll \alpha_T \ll 1$ and $z = O(1)$. With this assumption, Eq. (25) again represents a series whose terms decrease as powers of $x^{-1/3}$. The first three terms, in this case, agree exactly with those of the soft zeros, Eq. (17b), and the material properties enter only in higher order terms. Conditions of validity are now Eqs. (23) with $\bar{\eta}_n$ replaced by η_n .

Numerical values of Eq. (22b) are shown in Figures 4a and 4b for the two lowest Franz zeros, F1 and F2, for an aluminum cylinder in water, as compared to the zeros for soft and rigid cylinders in water. The zeros are plotted as trajectories in the complex k_{Fn}/k plane with values of ka as a parameter. Only those soft-cylinder zeros are shown which do not interfere with the rest of the figure. It is seen that in the range of x presented here, the elastic-cylinder zeros lie close to those for the rigid cylinder as expected. For increasing mode number, corresponding elastic and rigid zeros move closer together.

ID. The Whispering Gallery Zeros

This type of zeros also arises due to the finite curvature of the surface, but is associated with the material properties of the elastic solid, and therefore does not exist in the case of impenetrable objects. Since they are no longer present in the limit of a flat surface, we cannot expand the position of the zeros about the flat limit. Instead, we find the positions of the longitudinal and transverse Whispering Gallery zeros by expanding about the known positions of the zeros of $J_V(x_L)$ and $J_V(x_T)$, respectively. The latter are located on the real axis in Figure 1, to the left of x_L and x_T , respectively, and are given by¹⁴ ($n=1,2,\dots$):

$$x_{L,T,n} = x_{L,T} + \eta_n (x_{L,T}/2)^{1/3} + (\eta_n^2/60) (2/x_{L,T})^{1/3} + \theta(x_{L,T}^{-1}) \quad (26)$$

where η_n are defined in Eq. (17c).

ID1. The Transverse Whispering Gallery Zeros

In this case, we calculate the trajectories for the zeros which tend toward x_T for large cylinder radii. The region of interest in Figure 1 is Region 6, where we use the ordinary Debye expansions of Eqs. (7) for $f(x_L)$, $g(x_L)$, and $h(x)$, but the Airy-type asymptotic expansion (Appendix A) for $f(x_T)$:

$$f(x_T) \sim -\frac{1}{3x_T} + \frac{1}{P} \frac{\partial P}{\partial x_T} + \frac{\partial g}{\partial x_T} \frac{Ai'(g)}{Ai(g)} + \theta(x_T^{-1-2m/3}) \quad (27)$$

with P, g and m defined in Appendix A. One can write $g(x_T)$ in terms of $f(x_T)$ in Eq. (5) using Eq. (6b). Substituting these expansions into Eq. (5), we obtain the equation

$$Ai'(g)/Ai(g) = \Gamma_T \quad (28.1)$$

where

$$\Gamma_T = \frac{1}{\partial g / \partial x_T} \left\{ \frac{1}{\xi^2} \left[\frac{(\xi^2 - \frac{1}{2} \alpha_T^2)^2}{\alpha_T (\xi^2 - \alpha_L^2)^{1/2}} + i \frac{\rho_1}{\rho_2} \frac{\alpha_T^3}{4(1 - \xi^2)^{1/2}} \right] - \frac{1}{3x_T} + \frac{1}{P} \frac{\partial P}{\partial x_T} \right\} + \mathcal{O}(x_T^{-5/3}). \quad (28b)$$

Using Eqs. (A8) and the relations

$$y = x_T + \mathcal{O}(x_T^{1/3})$$

$$\left(\frac{\partial g}{\partial x_T} \right)^{-1} = -\left(\frac{x_T}{2} \right)^{1/3} + \mathcal{O}(x_T^{-1/3}),$$

we obtain from Eq. (28b), to lowest order in the quantity $x_T^{-4/3}$:

$$\Gamma_T = \mathcal{O}(x_T^{1/3}). \quad (29)$$

Therefore $\Gamma_T > 1$ for all $x_T > 1$, and letting $\eta = g$, we expand $Ai'(\eta)$ and $Ai(\eta)$ about η_n . Then the quantity $\eta - \eta_n$ is expanded in powers of $1/\Gamma_T$ yielding

$$g(x_T, y) = \eta_n + \Gamma_T^{-1} + (\eta_n/3)\Gamma_T^{-3} + \mathcal{O}(x_T^{-4/3}). \quad (30)$$

Using Eq. (A8d), an iterative solution of this equation gives the following result for the transverse Whispering Gallery wave numbers ($n = 1, 2, \dots$):

$$k_{WT,n} = \gamma_{WT,n}/a \quad (31a)$$

where

$$\gamma_{WT,n} = x_T + \eta_n \left(\frac{x_T}{2} \right)^{1/3} + \left(\frac{\eta_n^2}{60} \right) \left(\frac{2}{x_T} \right)^{1/3} + u_T + \eta_n u_T \left(\frac{7}{6} - \frac{u_T}{2} + \frac{1}{3} u_T^2 \right) \left(\frac{2}{x_T} \right)^{2/3} + \mathcal{O}(x_T^{-1}) \quad (31b)$$

with χ_T defined in Eq. (22c) and

$$U_T = -4 \left\{ \alpha_T \left[(\alpha_T^2 - \alpha_L^2)^{-1/2} + i \frac{\rho_1}{\rho_2} k \chi_T^{-1} \right] \right\}^{-1} \quad (31c)$$

$$v_T = \frac{1}{2} \frac{\rho_2 \chi_T^3 (7\alpha_T^2 - 8\alpha_L^2) + i \rho_1 k^3 \alpha_T^2 (\alpha_T^2 - \alpha_L^2)^{3/2}}{\rho_2 \chi_T^3 (\alpha_T^2 - \alpha_L^2) + i \rho_1 k \chi_T^2 (\alpha_T^2 - \alpha_L^2)^{3/2}}. \quad (31d)$$

This result was arrived at after one iteration, assuming that $\alpha_L \ll \alpha_T \ll 1$. The first three terms agree exactly with those of the zeros of $J_\nu(x_T)$, Eq. (26), and the material properties enter only in higher order terms.

The binomial expansions used in obtaining Eqs. (31a, b) are valid under the conditions

$$x > 2 \alpha_T^2 \left| \frac{\eta_n}{\alpha_T^2 - \alpha_L^2} \right|^{3/2}, \quad (32a)$$

$$x > 2 \frac{k^3 \alpha_T^2}{\chi_T^3} |\eta_n|^{3/2}, \quad (32b)$$

$$x > \frac{2}{\alpha_T} |\eta_n v_T|^{3/2}. \quad (32c)$$

They impose lower limits on x , depending on the order of the zero, the most stringent condition being Eq. (32c). For an aluminum cylinder in water, the lower limits of validity were found to be $ka \sim 87$ for $WT,1$ and e.g. $ka \sim 547$ for $WT,5$. Numerical values of Eqs. (31) for this case are presented in Section IE.

1D2. The Longitudinal Whispering Gallery Zeros

In this case, we calculate the trajectories for the zeros which tend toward x_L for large cylinder radii. The region of interest in Figure 1 is Region 5, where we use the ordinary Debye expansion of Eq. (7c) for $h(x)$, and the Airy-type asymptotic expansion (Appendix A) for $f(x_L)$:

$$f(x_L) \sim -\frac{1}{3x_L} + \frac{1}{P} \frac{\partial p}{\partial x_L} + \frac{\partial q}{\partial x_L} \frac{Ai'(q)}{Ai(q)} + \theta(x_L^{-1-2m/3}) \quad (33)$$

with p, q and m defined in Appendix A. The method used for finding the longitudinal zeros involves an expansion about the zeros of $J_\nu(x_L)$ which lie on the anti-Stokes line for $J_\nu(x_T)$ (cf. Appendix A and Figure 1), and, therefore, would necessitate the use of the transition Debye expansion (Appendix A) for $f(x_T)$:

$$f(x_T) \sim -(1 - \xi_T^2)^{1/2} \tan \left\{ (x_T^2 - y^2)^{1/2} - y \cos^{-1} \xi_T - \pi/4 \right\} + \theta(x_T^{-1}). \quad (34)$$

However, the use of Eq. (34) renders the solution of Eq. (5) intractable analytically because of the presence of an overlapping double infinity of zeros. One group arises from the Airy function of x_L and the other from the tangent function of x_T . The latter group corresponds to the transverse Whispering Gallery zeros which lie outside the circle of Region 6, and they link up smoothly with our results, Eqs. (31), for the zeros inside the circle. We, therefore, approximate $f(x_T)$ in Eq. (34) by the appropriate non-transition Debye expansion (Appendix A):

$$f(x_T) \approx i(1 - \xi_T^2)^{1/2} + \theta(x_T^{-1}). \quad (35)$$

We will determine the validity of this approximation by a self-consistent check after we have calculated the desired zero positions.

Writing $g(x_L)$ in terms of $f(x_L)$ using Eq. (6b) and substituting these expansions into Eq. (5), we obtain the equation

$$Ai'(g)/Ai(g) = \Gamma_L \quad (36a)$$

where

$$\Gamma_L = \frac{1}{\partial g / \partial x_L} \left\{ \frac{1}{\alpha_L} \left[\frac{p_2 \alpha_T i (2\zeta^2 - \alpha_T^2) (2\zeta_T^2 - 1) (1 - \zeta^2)^{1/2}}{p_1 \alpha_T^3 - 4p_2 \zeta^2 (1 - \zeta^2)^{1/2} (1 - \zeta_T^2)^{1/2}} \right] - \frac{1}{3x_L} + \frac{1}{P} \frac{\partial P}{\partial x_L} \right\} + \mathcal{O}(x_L^{-5/3}). \quad (36b)$$

Using Eqs. (A8) and the relations

$$\nu = x_L + \mathcal{O}(x_L^{1/3})$$

$$(\partial g / \partial x_L)^{-1} = -(x_L/2)^{1/3} + \mathcal{O}(x_L^{-1/3}),$$

we obtain from Eq. (36b), to lowest order in the quantity $x_L^{-7/3}$:

$$\Gamma_L = \mathcal{O}\left(\frac{\alpha_T^3}{\alpha_L^3} x_L^{1/3}\right). \quad (37)$$

Therefore, for $\alpha_L < \alpha_T < 1$, $\Gamma_L > 1$ for all $x_L > 1$, and letting $\eta = g$, we expand $Ai'(\eta)$ and $Ai(\eta)$ about η_n . Then the quantity $\eta - \eta_n$ is expanded in powers of $1/\Gamma_L$, yielding

$$g(x_L, \nu) = \eta_n + \Gamma_L^{-1} + (\eta_n/3) \Gamma_L^{-3} + \mathcal{O}(x_L^{-4/3}). \quad (38)$$

Using Eq. (A8d), an iterative solution of this equation gives the following result for the longitudinal Whispering Gallery wave numbers ($n=1, 2, \dots$):

$$k_{WL,n} = \nu_{WL,n} / a \quad (39a)$$

where

$$\begin{aligned}
 x_{nL,n} = & x_L + \eta_n \left(\frac{x_L}{2} \right)^{1/3} + \frac{\eta_n^2}{60} \left(\frac{2}{x_L} \right)^{1/3} + i \frac{\rho_1 \alpha_L \alpha_T u_L}{\rho_2 (2\alpha_L^2 - \alpha_T^2)^2} \\
 & + i \frac{\rho_1 \alpha_L \alpha_T \eta_n}{\rho_2 (2\alpha_L^2 - \alpha_T^2)^2} \left\{ \frac{1}{6} u_L + v_L \right. \\
 & \left. - \frac{1}{3} \left[\frac{\rho_1 \alpha_L \alpha_T u_L}{\rho_2 (2\alpha_L^2 - \alpha_T^2)^2} \right]^2 \right\} \left(\frac{2}{x_L} \right)^{2/3} + \theta(x_L^{-1})
 \end{aligned}$$

(39b)

with χ_L defined in Eq. (22c) and

$$u_L = \frac{k \alpha_T^3}{\chi_L} - 4 \frac{\rho_2}{\rho_1} \frac{\alpha_L^2}{\alpha_T} (\alpha_T^2 - \alpha_L^2)^{1/2} \quad (39c)$$

$$v_L = \alpha_L^2 \left[\frac{k^3 (10\alpha_L^2 - \alpha_T^2 - 8)}{2\chi_L^3 (2\alpha_L^2 - \alpha_T^2)} - \frac{2\rho_2 (2\alpha_L^4 - 2\alpha_T^4 - \alpha_L^2 \alpha_T^2)}{\rho_1 \alpha_T (\alpha_T^2 - \alpha_L^2)^{1/2} (2\alpha_L^2 - \alpha_T^2)} \right]. \quad (39d)$$

(39d)

This result was arrived at after one iteration, assuming that $\alpha_L \ll \alpha_T \ll 1$. The first three terms agree exactly with those of the zeros of $J_v(x_L)$, Eq. (26), and the material properties enter only in higher order terms.

The binomial expansions used in obtaining Eqs. (39a, b) are valid under the conditions

$$x > 2\alpha_L^2 \left| \frac{\eta_n}{\alpha_T^2 - \alpha_L^2} \right|^{3/2} \quad (40a)$$

$$x > 2 \frac{k^3 \alpha_L^2}{\chi_L^3} |\eta_n|^{3/2}, \quad (40b)$$

$$x > 2\alpha_L^2 \left| \frac{2\eta_n}{2\alpha_L^2 - \alpha_T^2} \right|^{3/2}. \quad (40c)$$

They impose lower limits on X , depending on the order of the zero, the most stringent condition being Eq. (40c). For an aluminum cylinder in water, the lower limits of validity were found to be $ka \approx 23$ for $WL, 1$ and e.g. $ka \approx 141$ for $WL, 5$.

In order to determine the validity of our approximation for $f(x_T)$, we substitute our result for $\gamma_{WL,n}$, Eq. (39b), into the exact expression, Eq. (34), and into the approximate expression, Eq. (35), and compare the two for the case of an aluminum cylinder in water. We find that the approximation imposes an upper limit on x which increases monotonically with mode number n . This result is illustrated in Figure 5, where we have plotted, as a function of n , the value of ka at which the absolute value of the relative error in the approximation begins to exceed 25 percent. Numerical values of Eqs. (39) are presented in Section IE.

IE. Discussion of Results

In this section, we present a graphical comparison, for the specific example of a solid aluminum cylinder in water (and in one case, also in vacuum), between our analytic results for the various zeros and the results of Dickey,¹⁶ who used numerical methods to solve for the roots of $D(y)=0$. Dickey did not use Eqs. (7), but calculated the asymptotic expansions of the cylinder functions directly using the Airy-type expansions of Appendix A or Watson's formulation¹⁷ of the Debye expansions. It is found that the two methods complement each other insofar as the analytic results can be more easily carried to very high values of ka (where both methods become more

accurate, but where the numerical trajectories of one type of zero often become hard to determine and to identify among the variety of other zeros), while the numerical results retain their accuracy down to lower values of ka than the analytic ones, due to the various approximations made in the latter method. For the case of the Franz zeros, both methods are accurate down to very low values of ka and the agreement between the corresponding results is excellent. For the Rayleigh, Stoneley, and transverse Whispering Gallery zeros, an apparently smooth transition is obtained from the numerical results below $ka \sim 100$ (below $ka \sim 200$ for the Whispering Gallery zeros) to the analytic results for the higher values of ka up to $ka \rightarrow \infty$. Numerical results for the longitudinal Whispering Gallery zeros are not yet available.

Figure 6 presents the complex trajectories of k_r'/k for the Rayleigh zero as a function of the parameter ka . The circles represent the numerical and the crosses the analytic results (the latter being also shown in Figure 2). The agreement becomes better as ka increases. The circles appear to tend towards the calculated flat Rayleigh limit for $ka \rightarrow \infty$ (square), which had been used as the anchor point for the analytic calculation, but which has no connection with the numerical calculation.

In Figures 7, dispersion curves for the Rayleigh zeros are shown for aluminum cylinders in water (Figure 7a) or in air and vacuum (Figure 7b). The Rayleigh wave phase velocity c_r' is plotted in Figure 7a relative to the sound speed in water;

i.e., essentially the quantity $c_R'/c \equiv k/k_R'r$ is plotted, where $k_R'r \equiv \text{Re}(k_R)$. The results (circles: numerical results; curve: analytic result) tend towards the flat limit, c_R/c , as $ka \rightarrow \infty$. In Figure 7b, we plot the numerical Rayleigh zeros (circles) for the case of an aluminum cylinder in air ($c = 330$ m/sec, $\rho_1 = 0.00129 \text{ g/cm}^3$) and the analytic results (curve) as well as some previous results of Viktorov^{8,18} (crosses) for the aluminum cylinder in a vacuum. Here, the values of c_R'/c_R (i.e., normalized to the flat Rayleigh speed) are plotted vs. $k_R a$. The flat limit for aluminum-vacuum used here was taken¹⁸ as $c_R = 0.933c_T = 2836$ m/sec.

Figure 8 presents the numerical results (solid circles) and the analytic results (crosses) for the Stoneley wave phase velocity, c_S'/c , approaching the flat Stoneley limit $c_S/c = 0.9975$ (calculated by our numerical solution of the flat Rayleigh equation) as $ka \rightarrow \infty$. For values up to $ka = 100$, the agreement is not as close as for the case of the Rayleigh zero, but as pointed out earlier, the analytic method should become valid for the Stoneley zero only at relatively higher values of ka as compared to the Rayleigh pole.

The first five Franz zeros, together with the Stoneley zero again, are shown in Figure 9; here, Figure 9a presents dispersion curves of c_F/c and c_S'/c plotted vs. ka and Figure 9b shows the normalized attenuations or imaginary parts of the wave numbers, γ_{F_i}/ka and $\gamma_{S_i'}/ka$, plotted vs. ka . The agreement between the solid curves (analytic results) and the

circles (numerical results) is excellent, reflecting the increased overlap in the range of validity of the two methods for this case.

Results for the Stoneley zero (solid circles and crosses) have been entered in Figures 9a and 9b also. While its dispersion curve is very similar to that of one of the lower Franz zeros, it may nevertheless be clearly distinguished from the latter by its much lower attenuation as seen in Figure 9b.

In Figure 10a, the dispersion curves of ω_{WT}/c for the first five transverse Whispering Gallery zeros and ω_R/c for the Rayleigh zero are plotted vs. ka . The solid curves are the numerical results, while the long dashes correspond to the analytic results for which the previously mentioned conditions of validity, Eqs. (10c) and (32c), are satisfied; the short dashes represent the analytic results for which these conditions are not satisfied. There is a smooth transition from the numerical to the analytic results, with the value of ka for which they link up increasing with mode number, as expected. In Figure 10b, the normalized attenuations $\gamma_i/ka)_{WT}$ are plotted vs. ka . The numerical results (solid curves) are shown for the first four zeros, while the analytic results (long dashes) are shown for the first two. Although the agreement between the two methods is not as good here as it was in the dispersion curves, there is, nevertheless, a smooth transition from the extrapolated numerical (short dashes) to the analytic results at high ka 's.

The analytic results for the first seven longitudinal Whispering Gallery zeros are shown in Figure 11. The dispersion curves of ω_{WL}/c vs. ka are given in Figure 11a, and the normalized attenuations $\nu_i/ka)_{WL}$ vs. ka are plotted in Figure 11b. For each mode, the region of greatest accuracy is shown as a solid curve whose lower limit is determined from Eq. (40c) and whose upper limit is ka_{max} from Figure 5.

Thus, our analytic and Dickey's numerical results, arrived at independently, are in good agreement with each other, increasingly so at high values of ka where the quantities tend toward their expected flat limits.

Chapter II. The Scattering of a Cylindrical Wave
by a Large, Solid Elastic Cylinder

If a cylindrical wave, emanating from an infinite line source of unit strength at $S(r_0, \phi)$ in the fluid, is incident upon a solid elastic cylinder of radius a (Figure 12), the total acoustic pressure at point $P(r, \phi)$ in the fluid is^{1,19} [with a time factor $\exp(-i\omega t)$ suppressed]

$$p = \frac{i}{8} \sum_{n=0}^{\infty} \epsilon_n \cos n\phi \left(B_n / D_n \right) H_n^{(1)}(kr_0), \quad r < r_0 \quad (41a)$$

where

$$\epsilon_0 = 1; \quad \epsilon_n = 2, \quad n > 0,$$

$$B_n = D_n H_n^{(2)}(kr) + b_n H_n^{(1)}(kr),$$

(41b)

$$b_n = - \begin{vmatrix} a^2 H_n^{(2)}(x) & \alpha_n^{L1} & \alpha_n^{T1} \\ x H_n^{(2)'}(x) & \alpha_n^{L2} & \alpha_n^{T2} \\ 0 & \alpha_n^{L3} & \alpha_n^{T3} \end{vmatrix},$$

(41c)

and D_n , α_n^{Li} , and α_n^{Ti} ($i=1, 2, 3$) are defined in Eqs. (2).

Application of the Watson-Sommerfeld transformation^{1,19} to the series solution then leads to

$$P = P_I + P_{II}$$

(42a)

where

$$P_I = -\frac{1}{8} P \int_{C'} \frac{dv}{\sin \pi v} \cos v(\pi - \phi) \frac{B_v}{D_v} H_v^{(1)}(kr_0),$$

(42b)

$$P_{II} = -\frac{1}{8} \int_{C_0} \frac{dv}{\sin \pi v} \cos v(\pi - \phi) \frac{B_v}{D_v} H_v^{(1)}(kr_0),$$

(42c)

and the contours C' and C_0 are shown in Figure 13 and result from opening up the original contour C of the Watson transformation. The contribution of the "background integral" P_I has been shown to be small²⁰ and will be neglected. The contour C_0 surrounds the zeros of D_v (first-order poles of the integrand) discussed in Chapter I. Splitting P_{II} into integrals over contours C_1 and C_2 (Figure 14) and applying Imai's transformation^{1,19}

$$\cos v(\pi - \phi) = e^{iv\pi} \cos v\phi - ie^{iv\phi} \sin v\pi$$

(43)

to the integral over C_2 serves to split off the geometrical part of the solution (which no longer has $1/\sin \gamma y$ in the integrand), thus yielding residue sums which converge on both the insonified and shadow sides of the cylinder. The geometrical part P_g can be evaluated using the saddle point method (corresponding to the far-field approximation $r, r_0 \rightarrow \infty$), where the saddle point contour C_s is drawn in Figure 14. Also shown is the saddle point (to the right of ka) which yields the incident wave and the saddle point y_s which yields the geometrically reflected wave^{1,19} and separates the two types of residue sums P_1 and P_2 (arising from the integrals around contours C_1 and C_2). Higher-order saddle points yield waves which are transmitted through the cylinder²⁰. We then have

$$P_{\pi} = P_1 + P_2 + P_g \quad (44a)$$

with

$$P_1 = -\frac{\pi i}{4} \sum_n \frac{\cos \gamma_n(\pi - \phi)}{\sin \pi \gamma_n} \frac{b_{\gamma_n}}{D_{\gamma_n}} H_{\gamma_n}^{(1)}(kr) H_{\gamma_n}^{(1)}(kr_0), \quad \text{Re } \gamma_n < y_s \quad (44b)$$

$$P_2 = -\frac{\pi i}{4} \sum_n \frac{\cos \gamma_n \phi}{\sin \pi \gamma_n} e^{i\pi n} \frac{b_{\gamma_n}}{D_{\gamma_n}} H_{\gamma_n}^{(1)}(kr) H_{\gamma_n}^{(1)}(kr_0), \quad \text{Re } \gamma_n > y_s \quad (44c)$$

$$P_g = \frac{i}{8} \int_{C_s} dy e^{i\pi \phi} \frac{B_y}{D_y} H_y^{(1)}(kr_0), \quad (44d)$$

where

$$\dot{D}_y = \partial D / \partial y. \quad (44e)$$

In the limit of infinite radius, it can be shown that P_2 yields the corresponding geometrical portions of the field (i.e., incident, geometrically reflected, and transmitted waves) for the flat elastic half-space (cf. Appendix B and Brill^{20,21}). We are concerned here with the residue sums P_1 and P_2 , which yield circumferential waves, in the limit of zero curvature.

We first examine the limiting behavior of the saddle point y_s , since its position determines which residue sum is used. The equation which y_s satisfies is:¹⁹

$$\cos^{-1} \frac{y_s}{kr} + \cos^{-1} \frac{y_s}{kr_0} = 2 \cos^{-1} \frac{y_s}{ka} + \phi \quad (45)$$

In taking the limit of Eq. (45), the following changes of variable are used²² (and will be useful later on):

$$y = ka \sin \theta, \quad (46a)$$

$$s = a \phi, \quad (46b)$$

$$R = r - a, \quad R_0 = r_0 - a, \quad (46c)$$

where θ is the angle of incidence on the flat elastic half-space. Thus, a , r , and r_0 tend toward infinity while the source-surface and receiver-surface distances remain constant. Keeping terms in Eq. (45) through $\theta(a^{-1})$, we then find that:

$$\sin \theta_s = \frac{s}{[s^2 + (R + R_0)^2]^{1/2}} \quad (47)$$

When we make the associations

$$s \rightarrow x, \quad R \rightarrow z, \quad R_0 \rightarrow z_0, \quad (48)$$

it is clear that Eq. (47) is exactly the equation satisfied by the saddle point θ_0 for the flat elastic half-space (cf. Appendix B and Fig. B1). Thus, the saddle point y_s which yields the geometrically reflected wave in the cylindrical case tends toward the saddle point θ_0 which yields the geometrical reflection in the flat case; the two are related by the transformation Eq. (46a) between the y - and θ -planes. We will investigate the case where $Re k_R \alpha < y_s < x$ (cf. Figure 14) which, in the limit, maps into the flat case shown in Figure B2 and discussed in Appendix B. Thus, we consider a source-surface-receiver geometry for which, in the flat limit, all the surface waves (except the Stoneley) contribute to the field at the observation point. From Figure 14, it is clear that residue sum P_1 includes the Rayleigh and Whispering Gallery poles, while residue sum P_2 includes the Stoneley and Franz poles.

IIA. The Residue Sum P_2

Using the expansion¹

$$\frac{1}{\sin \theta y_n} = -2ie^{i\theta y_n} \sum_{m=0}^{\infty} e^{2im\theta y_n} \quad , \quad (49)$$

we can rewrite P_2 as

$$P_2 = -\frac{\pi i}{4} \sum_n \sum_{m=0}^{\infty} \left[e^{iy_n(\theta + 2\pi + 2m\pi)} + e^{-iy_n(\theta - 2\pi - 2m\pi)} \right] \times \frac{b_{y_n}}{D_n} H_{y_n}^{(1)}(kr) H_{y_n}^{(1)}(kr_0), \quad Re y_n > y_s \quad (50)$$

We then separate P_2 into the sums $P_{2,F}$ over the Franz poles and $P_{2,S'}$ over the Stoneley pole. Using the Franz pole positions γ_{Fn} of Eq. (25), the appropriate Debye expansions (cf. Appendix A) for the Hankel functions of r and r_0 , and Eq. (46b) along with the relations (cf. Figs. 15)

$$d = (r^2 - a^2)^{1/2}, \quad d_0 = (r_0^2 - a^2)^{1/2}, \quad (50a)$$

$$\phi' = \cos^{-1} \frac{a}{r}, \quad \phi_0 = \cos^{-1} \frac{a}{r_0}, \quad (50b)$$

we find the following asymptotic expression for the Franz waves:

$$P_{2,F} \sim \frac{i}{2} \sum_{n=1}^{\infty} \sum_{m=0}^{\infty} \frac{1}{k(d_0)^{1/2}} \left\{ e^{i[k(d_0 + d) + (k + k_r)s] - k_i s} + e^{i[k(d_0 + d) + (k + k_r)s'] - k_i s'} \right\} \times e^{\frac{2im\pi\gamma_{Fn}}{D_{\gamma_{Fn}}}} \frac{b_{\gamma_{Fn}}}{D_{\gamma_{Fn}}} \quad (51a)$$

where

$$k_r = \frac{1}{2} |\eta_n| \left(\frac{k}{2} \right)^{1/3} a^{-2/3}, \quad (51b)$$

$$k_i = \sqrt{3} k_r, \quad (51c)$$

and the arc lengths s and s' are shown in Figures 15.

The term b_{Fn}/D_{Fn} contributes an algebraic (non-exponential) factor (e.g., see Nussenzveig's calculation for the soft sphere²³). Thus, the n^{th} Franz wave gets on the cylinder tangentially, creeps clockwise as in Figure 15a (or counter-clockwise as in Figure 15b) around the cylinder [traversing the arc length s (or s')] with speed $\omega/(k+k_r)$ and attenuation k_s , and gets off tangentially after m circumnavigations. As a tends toward infinity, $k_s s$ and $k_s s'$ also become infinite, so that in the limit of zero curvature, the Franz waves are exponentially damped out and never reach the observation point. Thus, they do not contribute to the field in the flat case.

In an analogous manner, we find the following asymptotic expression for the Stoneley wave (cf. Figures 15):

$$\begin{aligned}
 P_{2,s'} \sim & \frac{i}{2} \sum_{m=0}^{\infty} \frac{1}{k(d_d)^{1/2}} \left\{ e^{i[k(d_0+d) + k_{sr}s] - k_s s} \right. \\
 & \left. + e^{i[k(d_0+d) + k_{sr}s'] - k_s s'} \right\} \\
 & \times e^{2im\pi\gamma_s} \frac{b_{s'}}{D_{s'}} ,
 \end{aligned} \tag{52}$$

where we have assumed that the fluid is slightly lossy so that the flat Stoneley wave number k_s is complex ($k_s = k_{sr} + ik_s$). Thus, the Stoneley wave is also exponentially damped out and never reaches the observer. As the cylinder radius tends toward infinity, the Stoneley wave contributes to the field only in the case of glancing incidence ($\gamma_s \approx ka$), in which case

the method of steepest descent must be modified to take into account the effect of a pole near the saddle point γ_s (cf. Appendix B).

IIB. The Residue Sum P_1

Using the expansion of Eq. (49), we can rewrite P_1 as

$$P_1 = \frac{\pi}{4} \sum_n \sum_{m=0}^{\infty} \left[e^{i\gamma_n(\varphi+2m\pi)} + e^{-i\gamma_n(\varphi-2\pi-2m\pi)} \right] \frac{H_{\gamma_n}^{(2)}(x)}{H_{\gamma_n}^{(1)}(x)} \frac{\frac{f_2(\gamma_n)}{\frac{\partial}{\partial y} f_1(y)|_{y=\gamma_n}}}{H_{\gamma_n}^{(1)}(ky) H_{\gamma_n}^{(1)}(ky_0)},$$

$\operatorname{Re} \gamma_n < \gamma_s,$ (53a)

where

$$f_i(\gamma_n) = x \frac{H_{\gamma_n}^{(i)}(x)}{H_{\gamma_n}^{(1)}(x)} - a^2 \frac{D_i(\gamma_n)}{D_2(\gamma_n)} \quad (i=1,2), \quad (53b)$$

$$D_1(y) = \begin{vmatrix} \alpha_y^{L2} & \alpha_y^{T2} \\ \alpha_y^{L3} & \alpha_y^{T3} \end{vmatrix}, \quad D_2(y) = \begin{vmatrix} \alpha_y^{L1} & \alpha_y^{T1} \\ \alpha_y^{L3} & \alpha_y^{T3} \end{vmatrix}, \quad (53c)$$

and $\alpha_y^{L_i}$ and $\alpha_y^{T_i}$ ($i=1,2,3$) are defined in Eqs. (2). We note that Eq. (5), which we solved for the pole positions, corresponds exactly to $f_1(y)$ set equal to zero. We separate P_1 into the sums $P_{1,R'}$ over the Rayleigh pole and $P_{1,L}$ and $P_{1,T}$ over the longitudinal and transverse Whispering Gallery poles, respectively.

We calculate $P_{1,R'}$ first. Using the pole position

$$\gamma_{R'} = k_{R'} a, \quad (54)$$

where $k_{R'}$ is given in Eqs. (9) and (10), the appropriate Devye expansions (cf. Appendix A) for the Hankel functions

of x , r , and r_0 , and Eq. (46c), we find that

$$\frac{H_{Y_R'}^{(2)}(x)}{H_{Y_R'}^{(1)}(x)} \sim e^{-2i[\chi_{Rd} - \gamma_R \cos^{-1} \frac{k_R}{k} - \frac{\pi}{4}]} \quad (55a)$$

$$H_{Y_R'}^{(1)}(kr) H_{Y_R'}^{(1)}(kr_0) \sim \frac{2}{\pi a \chi_R} e^{2i[\chi_{Rd} - \gamma_R \cos^{-1} \frac{k_R}{k} - \frac{\pi}{4}]} \times e^{i\chi_R(R+R_0)} \quad (55b)$$

where (cf. Appendix B)

$$\chi_R = (k^2 - k_R^2)^{1/2} = k \cos \theta_R. \quad (55c)$$

Since $f_2(y)$ set equal to zero and calculated to lowest order in x corresponds to the generalized Rayleigh Eq. (8), it can be shown that, using Eq. (46a),

$$\frac{f_2(y_R)}{\frac{\partial}{\partial y} f_1(y)|_{y=y_R}} \sim -k a \cos \theta_R \frac{D_-(\theta_R)}{D_+(\theta_R)}, \quad (56)$$

where D_{\pm} is defined in Eq. (B3c). Combining Eqs. (55) and (56), and using Eq. (46b) along with the fact that asymptotically (cf. Figure 16)

$$\sin \theta_R \sim \sin \theta_R = \frac{s_0}{d_0} = \frac{s}{d}, \quad (57a)$$

$$\cos \theta_R \sim \cos \theta_R = \frac{R_0}{d_0} = \frac{R}{d}, \quad (57b)$$

we find the following asymptotic expression for the Rayleigh Wave

$$P_{z,R'} \sim -\frac{1}{2} \frac{D_-(\theta_R)}{D_+(\theta_R)} \left\{ e^{i[\bar{k}(d_0+d) + k_R s_R]} + e^{i[\bar{k}(d_0+d) + k_R s'_R]} \right\} \sum_{m=0}^{\infty} e^{2im\bar{k}y_R}, \quad (58)$$

where the arc lengths s_R and s'_R are shown in Figure 16. Thus, the Rayleigh wave is excited at the critical angle $(Re) \theta_R$ creeps clockwise (s_R) or counterclockwise (s'_R) around the cylinder with speed $\omega_{Re} k_R$ and attenuation $Im k_R$ and radiates off the cylinder at the same angle after m circumnavigations. As a tends toward infinity, s'_R also becomes infinite, and therefore the imaginary part of k_R causes the wave which creeps around the shadow side of the cylinder to be exponentially damped out, so that it never reaches the observer. The same argument holds true for the multiple circumnavigations ($m \neq 0$) and therefore the only wave which reaches the observation point in the limit of infinite radius is the one which traverses the finite arc length s_R and corresponds exactly to the Rayleigh wave for the flat elastic half-space [cf. Eqs. (B8)]:

$$P_{1,R'} \sim -\frac{1}{2} \frac{D_-(\theta_R)}{D_+(\theta_R)} e^{i[k(d_0+d) + k_R s_R]} \quad (59)$$

By using the Wronskian relation²⁴

$$\frac{H_{y_n}^{(2)}(x)}{H_{y_n}^{(1)}(x)} = \frac{H_{y_n}^{(1)}(x)}{H_{y_n}^{(2)}(x)} - \frac{4i}{\pi x} \frac{1}{H_{y_n}^{(1)}(x) H_{y_n}^{(2)}(x)} \quad (60a)$$

and the fact that [cf. Eq. (53b)]

$$f_1(y_n) = 0, \quad (60b)$$

we can further simplify our expression for P_1 :

$$P_1 = -i \sum_n \sum_{m=0}^{\infty} \left[e^{iy_n(\phi + 2m\pi)} + e^{-iy_n(\phi - 2\pi - 2m\pi)} \right] \frac{1}{[H_{y_n}^{(1)}(x)]^2} \frac{H_{y_n}^{(1)}(kx) H_{y_n}^{(2)}(kx)}{\frac{\partial}{\partial y} f_1(y) \Big|_{y=y_n}} > \quad Re y_n < y_s. \quad (61)$$

We calculate the limiting behavior ($x \rightarrow \infty$) of $P_{1,L}$ using the pole positions $\gamma_{WL,n}$ of Eqs. (39) even though the method used to calculate them imposed an upper limit on x which increased with mode number n (cf. Chapter ID2. and Figure 5). The justification for this procedure will be seen later in the calculation. For $P_{1,T}$ we use the pole positions $\gamma_{WT,n}$ of Eqs. (31). Then, using Eq. (46c) and the appropriate Debye expansions (cf. Appendix A) for the Hankel functions of x , r , and r_0 , and keeping one more order of accuracy of γ_n in the phase terms than in the algebraic factors, we find that

$$\frac{1}{[H_{\gamma_n}(x)]^2} \sim \frac{\pi}{2} \alpha \chi_{L,T} \exp \left\{ -2i \left[\chi_{L,T} a - \frac{2\gamma_n (k_{L,T})^{4/3}}{\chi_{L,T}} a^{1/3} - \gamma_n \cos^{-1} \alpha_{L,T} - \frac{\pi}{4} \right] \right\}, \quad (62a)$$

$$H_{\gamma_n}^{(1)}(kr) H_{\gamma_n}^{(1)}(kr_0) \sim \frac{2}{\pi \alpha \chi_{L,T}} \exp \left\{ 2i \left[\chi_{L,T} a - \frac{2\gamma_n (k_{L,T})^{4/3}}{\chi_{L,T}} a^{1/3} - \gamma_n \cos^{-1} \alpha_{L,T} - \frac{\pi}{4} \right] \right\} \exp \left\{ i(R+R_0) \left[\chi_{L,T} - \frac{2\gamma_n (k_{L,T})^{4/3}}{\chi_{L,T}} a^{-2/3} \right] \right\}, \quad \gamma_n = \gamma_{WL,WT,n}, \quad (62b)$$

where (cf. Appendix B)

$$\chi_{L,T} = (k^2 - k_{L,T}^2)^{1/2} = k \cos \theta_{L,T}. \quad (62c)$$

In order to calculate the quantity

$$\left[f_1'(\gamma_n) \right]^{-1} = \frac{1}{\frac{\partial}{\partial \gamma} f_1(\gamma) \Big|_{\gamma=\gamma_n}}, \quad (63)$$

we use the following asymptotic expression for $a^2 D_1/D_2$ [i.e., right hand side of Eq. (5)]:

$$\frac{a^2 D_1(\gamma)}{D_2(\gamma)} \sim - \frac{f_1 c^2 x}{\alpha_L} \left\{ \left[f(x_L) \right]^{-1} \left[\lambda + 2\mu(1 - \xi_L^2) \right] \left[2\xi_T^2 - 1 \right] + 4\mu \xi_L \xi_T f(x_T) \right\}^{-1} \quad (64)$$

where $\xi_i = y_i/x$ and $f(x_i)$, $i=L,T$, is defined in Eq. (6a).

The following Airy-type asymptotic expressions for $f(x_i)$ and its derivative will also be helpful [cf. Eqs. (27) and (33)]:

$$f(x_i) \sim \frac{\partial \xi}{\partial x_i} \frac{Ai'(q)}{Ai(q)} \sim -\left(\frac{2}{x_i}\right)^{1/2} \frac{Ai'(q)}{Ai(q)} \quad (65a)$$

$$\begin{aligned} \frac{\partial}{\partial y} f(x_i) &\sim \frac{Ai'(q)}{Ai(q)} \frac{\partial}{\partial y} \frac{\partial \xi}{\partial x_i} + \left\{ q - \left[\frac{Ai'(q)}{Ai(q)} \right]^2 \right\} \frac{\partial \xi}{\partial x_i} \frac{\partial \xi}{\partial y} \\ &\sim -\frac{\partial \xi}{\partial x_i} \frac{\partial q}{\partial y} \left[\frac{Ai'(q)}{Ai(q)} \right]^2 \sim -\left[\left(\frac{2}{x_i} \right)^{1/2} \frac{Ai'(q)}{Ai(q)} \right]^2 \end{aligned} \quad (65b)$$

where we have calculated the leading order behavior of these quantities. Then $[f_1'(y_n)]^{-1}$ for $y_n = y_{WL,n}$ is found by using the asymptotic expansions of Chapter ID2. and Eqs. (64) and (65) along with the fact that [cf. Eqs. (36)]

$$f(x_L) \Big|_{\substack{y=y_{WL,n} \\ \sim x_L}} = \frac{1}{\alpha_L \alpha_T} \left[\frac{\rho_2 i (2\alpha_L^2 - \alpha_T^2)^2 (1 - \alpha_L^2)^{1/2}}{\rho_1 \alpha_T^3 - 4\rho_2 \alpha_L^2 (1 - \alpha_L^2)^{1/2} (1 - \frac{\alpha_L^2}{\alpha_T^2})^{1/2}} \right]. \quad (66)$$

The result is

$$[f_1'(y_{WL,n})]^{-1} \sim -\frac{\rho_1 \alpha_L}{\rho_2 (1 - \alpha_L^2)} \frac{\alpha_T^4}{(2\alpha_L^2 - \alpha_T^2)^2} \frac{1}{x}. \quad (67)$$

Similarly, $[f_1'(y_n)]^{-1}$ for $y_n = y_{WT,n}$ is found by using the asymptotic expansions of Chapter ID1. and Eqs. (64) and (65) along with [cf. Eqs. (28)]

$$f(x_T) \Big|_{\substack{y=y_{WT,n} \\ \sim x_T}} = \frac{\alpha_T}{4\alpha_L \left(\frac{\alpha_T^2}{\alpha_L^2} - 1 \right)^{1/2}} + i \frac{\rho_1 \alpha_T}{4\rho_2 (1 - \alpha_T^2)^{1/2}}, \quad (68)$$

and the result is

$$[f_1'(y_{WT,n})]^{-1} \sim -\frac{4\rho_2}{\rho_1 \alpha_T} \frac{(\alpha_T^2 - \alpha_L^2)}{\left[\frac{\rho_2}{\rho_1} (1 - \alpha_T^2)^{1/2} + i (\alpha_T^2 - \alpha_L^2)^{1/2} \right]^2} \frac{1}{x}. \quad (69)$$

Finally, using Eqs. (62) and (46b) and the fact that asymptotically (cf. Figure 17)

$$\sin \theta_{L,T}^n \sim \sin \theta_{L,T} = \frac{s_0}{d_0} = \frac{s}{d}, \quad (70a)$$

$$\cos \theta_{L,T}^n \sim \cos \theta_{L,T} = \frac{R_0}{d_0} = \frac{R}{d}, \quad (70b)$$

(where $\theta_{L,T}^n$ is the excitation angle of the n^{th} Whispering Gallery wave) we find the following asymptotic expression for the longitudinal and transverse Whispering Gallery waves:

$$\begin{aligned} p_1^{L,T} \sim & -i [f_1'(y_{L,T})]^{-1} \left\{ e^{i[k(d_0+d) + k_{L,T} s_{L,T}]} \sum_{n=1}^{N_{L,T}} e^{i\eta_n \left(\frac{k_{L,T}}{2}\right)^{1/3} a^{-2/3} s_{L,T}} \right. \\ & \left. + e^{i[k(d_0+d) + k_{L,T} s'_{L,T}]} \sum_{n=1}^{N_{L,T}} e^{i\eta_n \left(\frac{k_{L,T}}{2}\right)^{1/3} a^{-2/3} s'_{L,T}} \right\} \\ & \times \sum_{m=0}^{\infty} e^{2im\pi y_{L,T,n}} \end{aligned} \quad (71)$$

where $[f_1'(y_{L,T})]^{-1}$ is defined in Eqs. (67) and (69), N_L (N_T) is the number of longitudinal (transverse) Whispering Gallery poles in the first quadrant of the y -plane (cf. Figure 14), and the arc lengths $s_{L,T}$ and $s'_{L,T}$ are shown in Figure 17. Thus, the n^{th} longitudinal or transverse Whispering Gallery wave is excited at the critical angle $\theta_{L,T}^n$ given by

$$\sin \theta_{L,T}^n = \frac{1}{k} \left[k_{L,T} + \eta_n \left(\frac{k_{L,T}}{2} \right)^{1/3} a^{-2/3} \right], \quad (72)$$

creeps clockwise ($s_{L,T}$) or counterclockwise ($s'_{L,T}$) around the cylinder with speed $\omega/k \sin \theta_{L,T}^n$ and radiates off at the same angle after m circumnavigations. If we assume that the cylinder is slightly lossy, so that $k_{L,T}$ has a small imaginary

part, then as a tends toward infinity, $s_{L,T}'$ also becomes infinite, and the waves which creep around the shadow side of the cylinder [including the multiple circumnavigations ($m \neq 0$)] are exponentially damped out and never reach the observer. The waves which remain are those which traverse the finite arc length $s_{L,T}$:

$$P_1^{L,T} \sim -i \left[f_1'(y_{L,T}) \right]^{-1} e^{i[k(d_0+d) + k_{L,T} s_{L,T}]} \sum_{n=1}^{N_{L,T}} e^{i\eta_n \left(\frac{k_{L,T}}{2} \right)^{1/3} a^{-2/3} s_{L,T}} \quad (73)$$

We now approximate the residue sum in Eq. (73) by an integral:

$$\sum_{n=1}^{N_{L,T}} e^{i\eta_n \left(\frac{k_{L,T}}{2} \right)^{1/3} a^{-2/3} s_{L,T}} \approx \int_0^\infty dn e^{-i \left[\frac{3\pi(4n-1)}{8a} \right]^{2/3} \left(\frac{k_{L,T}}{2} \right)^{1/3} s_{L,T}} \quad (74)$$

where we have used the approximation²⁴ for η_n that holds for large n :

$$\eta_n \approx -\left[\frac{3\pi(4n-1)}{8} \right]^{2/3} \quad (75)$$

The approximation of the sum by an integral is justified because $N_{L,T}$ goes to infinity as a tends toward infinity and because the function in the sum oscillates less rapidly as n increases, so that the contributions to the sum (integral) for small n tend to cancel out. Thus, the primary contribution to the residue sum (integral) comes from the higher order poles. We are, therefore, also completely justified in using the pole positions $y_{L,T,n}$ of Eqs. (39), since the method used to calculate them imposed an upper limit on X which increased monotonically with mode number n (cf. Chapter ID2. and Figure 5).

We point out that the method of approximating the residue sum by an integral is similar to that used by Tamir and Felsen²⁵ for the dielectric slab problem. Rulf,²² on the other hand, in considering the fluid-fluid (with $\rho_1 = \rho_2$) cylinder problem, did not use the explicit pole positions to evaluate the residue sum, but converted it back to a contour integral surrounding the poles. We treat the fluid-fluid case using our method in Appendix C.

In order to evaluate the integral in Eq. (74), first we change variables

$$y = \left[\frac{3\pi(4n-1)}{8a} \right]^{1/3} \quad (76a)$$

and then we evaluate the resultant integral:

$$\begin{aligned} & \int_0^\infty dne^{-i\left[\frac{3\pi(4n-1)}{8a}\right]^{2/3}\left(\frac{k_{L,T}}{2}\right)^{1/3}S_{L,T}} \\ &= \frac{2a}{\pi} \int_0^\infty dy y^2 e^{-i\left(\frac{k_{L,T}}{2}\right)^{1/3}S_{L,T}y^2} = -\frac{ia}{\sqrt{2\pi}} e^{-i\pi/4} \frac{1}{\sqrt{k_{L,T}S_{L,T}^{3/2}}}, \end{aligned} \quad (76b)$$

where we can assume that $k_{L,T}$ has a small imaginary part to assure convergence.²⁶

In the limit of infinite radius, the expressions for $P_{1,L}$ and $P_{1,T}$ then correspond exactly to the expressions for the longitudinal and transverse lateral waves for a flat elastic half-space [cf. Eqs. (B9)]:

$$P_{1,L} \sim \frac{e^{-i\pi/4}}{\sqrt{2\pi}} \frac{\alpha_L^2 \alpha_T^4}{m(1-\alpha_L^2)(\alpha_T^2 - 2\alpha_L^2)^2} \frac{e^{i[k(d_0+d) + k_L S_L]}}{(k_L S_L)^{3/2}} \quad (77a)$$

$$P_{1,T} \sim 2\sqrt{\frac{2}{\pi}} e^{-i\pi/4} \frac{m(\alpha_T^2 - \alpha_L^2)}{[m(1 - \alpha_T^2)^{1/2} + i(\alpha_T^2 - \alpha_L^2)^{1/2}]^2} \frac{e^{i[k(d_0 + d) + k_T s_T]}}{(k_T s_T)^{3/2}} \quad (77b)$$

with

$$m = \rho_2/\rho_1 .$$

Conclusions

We have established the connection between creeping wave and flat surface wave theory by investigating the limit of acoustic scattering from a solid elastic cylinder, imbedded in a fluid, whose radius tends to infinity.

First, we calculated the asymptotic behavior of the complex circumferential wave numbers by substituting the appropriate Debye-or Airy-type asymptotic expansions into the 3×3 secular determinant and solving it using iterative techniques. The creeping wave modes fall into two classes: those with speeds close to the sound speed in the fluid (Stoneley and Franz waves) and those with speeds close to the bulk wave speeds in the solid (Rayleigh and Whispering Gallery waves). It was found that, in the limit of infinite cylinder radius, the wave numbers of the Rayleigh and Stoneley modes tend toward those of the Rayleigh and Stoneley waves on a flat elastic half-space, while the Franz mode wave numbers tend toward the wave number of sound in the fluid. The longitudinal and transverse Whispering Gallery mode wave numbers tend toward the longitudinal and transverse wave numbers in the solid. Graphical results were presented for an aluminum cylinder in water (and in one case, also in vacuum) in the form of trajectories in the complex wave number plane, phase velocities, and attenuations, all as functions of fluid wave number times cylinder radius. The results show good agreement with existing numerical results.

Then, using the Watson-Sommerfeld transformation, we investigated the limiting behavior of the solution to the problem of the scattering of a cylindrical wave from a cylinder whose radius tends to infinity. Using the analytic expressions for the creeping wave numbers, we calculated the asymptotic behavior of the residue sums corresponding to the different classes of circumferential waves. It was found that, in the limit of infinite cylinder radius, the Rayleigh wave for the cylinder goes over to the Rayleigh wave on the flat elastic half-space, while the Franz and Stoneley waves are exponentially damped out (the Stoneley wave contributes to the field in the flat case only at glancing incidence, which is a special case mathematically, and was not discussed). In the limit, the longitudinal and transverse Whispering Gallery waves combine to form the longitudinal and transverse lateral waves, respectively, for the flat elastic half-space.

Thus, the transition of creeping wave to surface wave theory, as the scattering object tends toward a flat surface, has been established.

Appendix A

Asymptotic Expansions of Cylinder Functions^{13, 14, 17, 23}

In the following, we present asymptotic expansions of cylinder functions where both the values of the (real) argument, y , and of the modulus of the (complex) index, v , are large.

1. Debye asymptotic expansions

Debye expansions are appropriate for large values of $|v-y| = \theta(y)$, and are used outside the circles shown in Figure A1 whose radii are determined by $|v-y| = \theta(y^{1/3})$. The Debye expansions

$$H_v^{(1)}(y) \sim \frac{(2)^{1/2}}{\pi} \frac{\exp\left\{i(y^2-v^2)^{1/2} - iy\cos^{-1}v/y - i\pi/4\right\}}{(y^2-v^2)^{1/4}} \times \left\{1 - \frac{i}{(y^2-v^2)^{1/2}} \left[\frac{1}{8} - \frac{5y^2}{24(y^2-v^2)} \right] + \theta(y^{-2})\right\}, \quad (\text{Ala})$$

$$H_v^{(2)}(y) \sim \frac{(2)^{1/2}}{\pi} \frac{\exp\left\{-i(y^2-v^2)^{1/2} + iy\cos^{-1}v/y + i\pi/4\right\}}{(y^2-v^2)^{1/4}} \times \left\{1 + \frac{i}{(y^2-v^2)^{1/2}} \left[\frac{1}{8} - \frac{5y^2}{24(y^2-v^2)} \right] + \theta(y^{-2})\right\} \quad (\text{Alb})$$

are valid in Regions I and II of Figure A1, with

$$\begin{aligned} |\arg(y^2-v^2)^{1/2}| &< \pi/2 \\ 0 \leq \operatorname{Re}(\cos^{-1}v/y) &\leq \pi \\ \operatorname{Im}(\cos^{-1}v/y) &< 0 \quad (\text{Region I}) \\ &> 0 \quad (\text{Region II}). \end{aligned}$$

(Alc)

These regions are separated by the curves

$$\operatorname{Im}[(y^2 - y^4)^{1/2} - y \cos^{-1} y/y] = 0 \quad (\text{A2})$$

and by the portions of the real axis as indicated in the figure. The roots of $H_y^{(0)}(y)$ and of $H_y^{(1)}(y)$ lie on the curves labeled $h_{\pm 1}$ in Figure A1, those of $H_y^{(2)}(y)$ and $H_y^{(3)}(y)$ on the curves labeled $h_{\pm 2}$.

In Region III, one has instead

$$H_y^{(0)}(y) \sim -i \left(\frac{2}{\pi}\right)^{1/2} \exp \left\{ -\frac{(y^2 - y^4)^{1/2} + y \cosh^{-1} y/y}{(y^2 - y^4)^{1/4}} \right\} \times \left\{ 1 - \frac{1}{(y^2 - y^4)^{1/2}} \left[\frac{1}{8} - \frac{5y^2}{24(y^2 - y^4)} \right] + \mathcal{O}(y^{-2}) \right\}, \quad (\text{A3a})$$

$$H_y^{(1)}(y) \sim -H_y^{(0)}(y) \quad (\text{A3b})$$

with

$$|\arg(y^2 - y^4)^{1/2}| < \pi/2$$

$$\operatorname{Re}(\cosh^{-1} y/y) > 0$$

$$|\operatorname{Im}(\cosh^{-1} y/y)| < \pi/2.$$

(A3c)

In Regions IV and V, the appropriate results are obtained by using

$$H_{-y}^{(0)}(y) = e^{iy\pi} H_y^{(0)}(y) \\ H_{-y}^{(1)}(y) = e^{-iy\pi} H_y^{(1)}(y). \quad (\text{A4})$$

The curves $h_{\pm 1}$ are the anti-Stokes lines for the asymptotic expansions of $H_y^{(0)}(y)$, and the curves $h_{\pm 2}$ those for $H_y^{(1)}(y)$. In the vicinity of these lines (the "transition

region"), the sum of the asymptotic expansions for the two adjacent regions has to be used. In the ensuing "transition Debye forms," the two exponentials then combine to form trigonometric functions, while outside the transition regions, one of the two exponentials is dominant and the other subdominant.

Debye asymptotic expansions for the Bessel functions are, for Region III

$$J_v(y) \sim (2\pi)^{-1/2} \frac{\exp\left\{(y^2-y^2)^{1/2} - v \cosh^{-1} y/y\right\}}{(y^2-y^2)^{1/4}} \times \left\{ 1 + \frac{1}{(y^2-y^2)^{1/2}} \left[\frac{1}{8} - \frac{5y^2}{24(y^2-y^2)} \right] + \delta(y^{-2}) \right\} \quad (A5a)$$

with

$$\begin{aligned} |\arg(y^2-y^2)^{1/2}| &< \pi/2 \\ \operatorname{Re}(\cosh^{-1} y/y) &> 0 \\ |\operatorname{Im}(\cosh^{-1} y/y)| &< \pi/2. \end{aligned} \quad (A5b)$$

In all other regions, the appropriate expansions are found by using

$$J_v(y) = \frac{1}{2} [H_v^{(1)}(y) + H_v^{(2)}(y)] \quad (A6)$$

together with the previously stated results for $H_v^{(1)}(y)$.

The zeros of $J_v(y)$ are located on the real axis in Figure A1, to the left of y . This portion of the real axis forms the anti-Stokes line for $J_v(y)$, and in the surrounding transition region, one must use

$$J_v(y) \sim \left(\frac{2}{\pi}\right)^{1/2} \frac{1}{(y^2-y^2)^{1/4}} \left\{ \cos \omega + \frac{1}{(y^2-y^2)^{1/2}} \left[\frac{1}{8} - \frac{5y^2}{24(y^2-y^2)} \right] \right. \\ \left. \times \sin \omega + \delta(y^{-2}) \right\} \quad (A7a)$$

with

$$W = (\gamma^2 - y^2)^{1/2} - y \cos^{-1} y / \gamma - i\pi/4, \quad (A7b)$$

where

$$|\arg(\gamma^2 - y^2)^{1/2}| < \pi/2$$

$$0 \leq \operatorname{Re}(\cos^{-1} y / \gamma) \leq \pi. \quad (A7c)$$

2. Airy-type asymptotic expansions

For the case that $|y - \gamma| = \theta(y^{1/3})$, asymptotic expansions of the cylinder functions which are expressed in terms of the Airy function are appropriate. They are valid inside the circles of Figure A1. We have^{13, 14}

$$H_y^{(1)}(y) \sim 2 \left(\frac{2}{y}\right)^{1/3} P e^{-i\pi/3} Ai(-q e^{-i\pi/3}) + \theta \left[x^{-2/3(m+1)}\right] \quad (A8a)$$

$$H_y^{(2)}(y) \sim 2 \left(\frac{2}{y}\right)^{1/3} P e^{i\pi/3} Ai(-q e^{i\pi/3}) + \theta \left[x^{-2/3(m+1)}\right] \quad (A8b)$$

where

$$P(y, v) = \sum_{j=0}^m (-1)^j P_j(\tilde{v}) \left(\frac{2}{y}\right)^{2j+3}, \quad (A8c)$$

$$q(y, v) = \sum_{j=0}^m (-1)^j Q_j(\tilde{v}) \left(\frac{2}{y}\right)^{2j+3} \quad (A8d)$$

with

$$\tilde{v} = (y - \gamma) \left(\frac{2}{y}\right)^{1/3} \quad (A8e)$$

and

$$P_0(\tilde{v}) = 1, \quad P_1(\tilde{v}) = \frac{1}{15} \tilde{v}, \dots, \quad (A8f)$$

$$Q_0(\tilde{v}) = \tilde{v}, \quad Q_1(\tilde{v}) = \frac{1}{60} \tilde{v}^2, \dots, \quad (A8g)$$

and where the Airy function is given by

$$Ai(-z) = \frac{z^{1/2}}{3} [J_{1/3}(\zeta) + J_{-1/3}(\zeta)], \quad (A9a)$$

$$\zeta = \frac{2}{3} z^{3/2}, \quad (A9b)$$

it satisfies Airy's equation,

$$Ai''(z) - z Ai(z) = 0. \quad (A10)$$

For $J_v(y)$, one finds the compact expression

$$J_v(y) \sim \left(\frac{2}{y}\right)^{1/3} P Ai(\xi) + O\left[y^{-\frac{2}{3}(m+1)}\right]. \quad (A11)$$

Appendix B

The Reflection of a Cylindrical Wave at a Plane

Fluid-Solid Interface

In this section, we calculate the total acoustic field due to a line source in the presence of a plane fluid-solid interface, where both source and receiver are situated in the fluid. The analysis follows that of Brekhovskikh² and Überall,¹ who considered the fluid-fluid and fluid-solid cases for a point source, respectively. The field can be resolved into the incident wave, the geometrically reflected wave, and surface and lateral waves which propagate along the boundary and radiate into the fluid.

The geometry of the problem is shown in Figure B1. An infinite line source of unit strength is located at S. The incident pressure wave at the observation point P is, therefore⁸¹ [with a time factor $\exp(-i\omega t)$ suppressed]

$$P_{\text{inc}} = \frac{i}{4} H_0^{(1)}(k\rho). \quad (\text{B1})$$

Using the Sommerfeld representation^{1,2} for the Hankel function, we can write the incident field as a decomposition into plane waves⁸² with angle of incidence θ :

$$P_{\text{inc}} = \frac{i}{4\pi} \int_C d\theta e^{ik(x\sin\theta + |z-z_0|\cos\theta)} \quad (\text{B2})$$

where the contour C is drawn in Figure B2. The reflected wave is then given by^{1,2}

$$P_{\text{refl}} = \frac{i}{4\pi} \int_C d\theta R(\theta) e^{ik[x\sin\theta + (z+z_0)\cos\theta]} \quad (\text{B3a})$$

where $R(\theta)$ is the plane wave reflection coefficient for a plane fluid-solid interface:¹

$$R = D_- / D_+ , \quad (B3b)$$

with

$$D_{\pm} = \rho_2 \cos \theta \left[(b_T^2 - \sin^2 \theta)^2 + 4 b_L b_T \sin^2 \theta \right] \pm \rho_1 b_L (b_T^2 + \sin^2 \theta)^2 \quad (B3c)$$

and

$$b_{L,T} = (\alpha_{L,T}^2 - \sin^2 \theta)^{1/2}, \quad \alpha_{L,T} = k_{L,T} / k . \quad (B3d)$$

Equation (B3a) for the reflected wave can be rewritten as

$$P_{\text{refl}} = \frac{i}{4\pi} \int_C d\theta R(\theta) e^{ik\rho' \cos(\theta - \theta_0)} \quad (B4)$$

where ρ' is the distance from the image source S' to the observation point P .

The integral in Eq. (B4) is evaluated using the method of steepest descent^{1,2}, where we assume $k\rho' \gg 1$. The path of steepest descent C_s and the saddle point θ_0 (corresponding to the angle of incidence or reflection of the geometrically reflected wave) are shown in Figure B2. The result for the geometrically reflected wave is then

$$P_{\text{g.r.}} = \frac{1}{4} \sqrt{\frac{2}{\pi}} e^{i k \theta_0} R(\theta_0) \frac{e^{i k \rho'}}{\sqrt{k \rho''}} \quad (B5)$$

as expected from geometrical acoustics.

Additional contributions to the reflected field arise from any singularities of $R(\theta)$ which are crossed as contour

C is deformed into contour C_3 . Branch point singularities, provided by the radicals b_L, b_T , are found at

$$\theta_L = \pm \sin^{-1} \alpha_L, \quad \theta_T = \pm \sin^{-1} \alpha_T \quad (B6)$$

while poles [corresponding to solutions of $D_+ = 0$, which is completely equivalent to the generalized Rayleigh Eq. (8)] of physical interest occur at

$$\theta_R = \sin^{-1}(k_R/k), \quad \theta_S = \sin^{-1}(k_S/k) \quad (B7)$$

where k_R and k_S are the Rayleigh and Stoneley wave numbers [e.g., Eqs. (11) and (16) for the water-aluminum interface]. These branch points (and the corresponding branch cuts) and poles are shown in Figure B2.

The angles $\text{Re}\theta_R$, $\text{Re}\theta_S$, θ_L , and θ_T are the critical angles of incidence for excitation of the Rayleigh, Stoneley, and longitudinal and transverse lateral waves, respectively (for the water-aluminum interface: $\theta_L = 13^\circ 26'$, $\theta_T = 29^\circ 20'$, $\text{Re}\theta_R = 31^\circ 36'$, $\text{Re}\theta_S = 90^\circ$). When $\theta_o \geq \text{Re}\theta_R$, θ_L , and θ_T , as in Figure B2, then the Rayleigh and lateral waves contribute to the field at the observation point P. The Rayleigh wave contribution is found from the residue at the Rayleigh pole, while the longitudinal and transverse lateral wave contributions arise from integrals around the branch cuts originating at θ_L and θ_T , respectively. The resulting expressions are:

Rayleigh Wave:

$$P_R = -\frac{1}{2} \frac{D_-(\theta_R)}{D_+(\theta_R)} e^{i[k(L_o + L) + k_R L_R]} \quad (B8a)$$

where

$$L_0 = z_0 / \cos \theta_R, \quad L = z / \cos \theta_R, \quad D_+(\theta) = \partial D_+(\theta) / \partial \theta \quad (B8b)$$

Longitudinal Lateral Wave:

$$P_L = \frac{e^{-i\pi/4}}{\sqrt{2\pi}} \frac{\alpha_L^2 \alpha_T^4}{m(1-\alpha_L^2)(\alpha_T^2 - 2\alpha_L^2)^2} \frac{e^{i[k(L_0+L) + k_L L_L]}}{(k_L L_L)^{3/2}} \quad (B9a)$$

Transverse Lateral Wave:

$$P_T = 2\sqrt{\frac{2}{\pi}} e^{-i\pi/4} \frac{m(\alpha_T^2 - \alpha_L^2)}{[m(1-\alpha_T^2)^{1/2} + i(\alpha_T^2 - \alpha_L^2)^{1/2}]^2} \frac{e^{i[k(L_0+L) + k_T L_T]}}{(k_T L_T)^{3/2}} \quad (B9b)$$

where

$$L_0 = z_0 / \cos \theta_{L,T}, \quad L = z / \cos \theta_{L,T}, \quad m = \rho_2 / \rho_1. \quad (B9c)$$

The geometrical meaning of these results is clear from inspection of the phases and Figures B3 and B4. In each case, the wave is excited at its critical angle, propagates along the interface, and reaches the observation point P by radiating into the fluid at the same angle.

The Stoneley wave is not excited unless $\theta \approx \pi/2$ (glancing incidence), in which case the method of steepest descent must be modified to take into account the effect of a pole near the saddle point.² This case will not be discussed here.

Appendix C
Creeping Waves and Lateral Waves
for the Fluid Cylinder

In the case of scattering by a fluid cylinder ($C_T \rightarrow 0$) we have the residue sum P_1 of Eqs. (53) or (61) with

$$f_i(y_n) = x \frac{H_{y_n}^{(i)}(x)}{H_{y_n}^{(i)}(x)} - \frac{\rho_1}{\rho_2} x_L \frac{J_{y_n}'(x_L)}{J_{y_n}(x_L)} \quad (i=1,2). \quad (C1)$$

The Whispering Gallery pole positions are given by¹⁴

$$y_{w_{L,n}} = x_L + \eta_n \left(\frac{x_L}{2} \right)^{1/3} + \mathcal{O}(1) \quad (C2)$$

where, as in the case of the solid, the material properties enter only in higher order terms. Using the appropriate Debye expansions for the Hankel functions of x and Airy-type expansions for the Bessel functions of x_L (cf. Appendix A) along with Eqs. (65) and the fact that

$$\left. \frac{J_y'(x_L)}{J_y(x_L)} \right|_{\substack{y=y_{w_{L,n}} \\ \sim x_L}} = i \frac{\rho_2}{\rho_1 \alpha_L} (1 - \alpha_L^2)^{1/2}, \quad (C3)$$

we obtain the result

$$\left[f_1'(y_{w_{L,n}}) \right]^{-1} \sim - \frac{\rho_1 \alpha_L}{\rho_2 (1 - \alpha_L^2)} \frac{1}{x}, \quad (C4)$$

which is just the limit of Eq. (67) for the solid as α_T goes to infinity. Then, using Eqs. (62), (46b), (70), and (C4), and approximating the residue sum by an integral as before, we find that

$$P_{1,L} \sim \frac{e^{-i\pi/4}}{\sqrt{2\pi}} \frac{\alpha_L^2}{m(1 - \alpha_L^2)} \frac{e^{i[k(d_0 + d) + k_L s_L]}}{(k_L s_L)^{3/2}}, \quad (C5)$$

which is just the limit of Eq. (77a) as α_T goes to infinity and corresponds exactly to the expression for the lateral wave for a flat fluid half-space^{2,22}.

List of Illustrations

Fig. 1 Complex γ -plane with various regions in which different asymptotic expansions of cylinder functions are employed in our analytic calculation.

Fig. 2 Rayleigh zero trajectory in the complex plane k_R'/k at varying values of the parameter ka , for the case of an aluminum cylinder in water.

Crosses: present work; solid circles: numerical results of Uginčius⁹; solid square: flat Rayleigh limit. Also shown is the location of k_T/k , whose (real) numerical value is 0.491.

Fig. 3 Stoneley zero trajectory in the complex plane k_S'/k at varying values of the parameter ka , for the case of an aluminum cylinder in water.

Fig. 4 Franz zero trajectories in the complex plane k_{Fn}/k at varying values of the parameter ka , for the cases of soft (■), rigid (●), and aluminum cylinders (x) in water: (a) first Franz zero, $n=1$, (b) second Franz zero, $n=2$.

Fig. 5 The value of ka , as a function of mode number n , at which the absolute value of the relative error in the approximation to the tangent function, used to

calculate the longitudinal Whispering Gallery zeros, begins to exceed 25 percent.

Fig. 6 Rayleigh zero trajectory in the complex plane k_R'/k at varying values of the parameter ka , for the case of an aluminum cylinder in water. Crosses: analytic results; square: flat Rayleigh limit ($ka \rightarrow \infty$). Circles: numerical results.

Fig. 7 (a) Normalized phase velocity c_R'/c of the Rayleigh wave for an aluminum cylinder in water, plotted vs. ka . Circles: Numerical results, curve: analytic results.

(b) Normalized phase velocity c_R'/c_R of the Rayleigh wave, plotted vs. $k_R a$. Circles: numerical results for aluminum cylinder in air. Curve: analytic results, and crosses: Viktorov's^{8,18} results, both for aluminum cylinder in a vacuum.

Fig. 8 Dispersion curve for the Stoneley wave on an aluminum cylinder in water. Solid circles: numerical results. Crosses: analytic results.

Fig. 9 Stoneley and first five Franz zeros for an aluminum cylinder in water. (a) Dispersion curves, (b) normalized attenuation. For the Franz zeros, analytic

results are given by solid curves, numerical results by open circles. For the Stoneley zero, analytic results are given by crosses, numerical results by solid circles.

Fig. 10 (a) Dispersion curves for the first five transverse Whispering Gallery zeros and the Rayleigh zero for an aluminum cylinder in water. The numerical results are given by solid curves; the analytic results are shown as long dashes where they are most accurate and short dashes where they are less reliable.

(b) Normalized attenuations for the Whispering Gallery zeros. Solid curves: numerical results for first four zeros. Short dashes: extrapolated numerical results. Long dashes: analytic results for first two zeros.

Fig. 11 The first seven longitudinal Whispering Gallery zeros for an aluminum cylinder in water. (a) Dispersion curves, (b) normalized attenuation. The analytic results are shown as solid curves where they are most accurate and dashes where they are less reliable.

Fig. 12 Geometry of the cylinder scattering problem; line source at S, observer at P.

Fig. 13 The complex ν -plane showing contours for the Watson-Sommerfeld transformation used in the elastic cylinder

scattering problem [Figure taken from Doolittle, et al.⁴ with permission of the American Institute of Physics].

Fig. 14 The complex ν -plane showing contours for separating out the geometrical wave. Also shown schematically are the positions of the saddle point ν_s and the Rayleigh ($k_R a$), Stoneley ($k_S a$), Franz (ν_F), and longitudinal (ν_{WL}) and transverse (ν_{WT}) Whispering Gallery poles for a large, fixed value of ka .

Fig. 15 Franz or Stoneley wave getting on the cylinder tangentially, creeping clockwise (Fig. 15a) or counterclockwise (Figure 15b) around it, and getting off the cylinder tangentially.

Fig. 16 Rayleigh wave being excited at the critical angle θ_R , creeping clockwise or counterclockwise around the cylinder, and radiating off at the same angle.

Fig. 17 Longitudinal or transverse Whispering Gallery wave being excited at the critical angle $\theta_{L,T}$, creeping clockwise or counterclockwise around the cylinder, and radiating off at the same angle.

Fig. A1 Complex ν -plane showing regions of validity for different asymptotic expansions of the cylinder functions, used in the analytic calculation.

Fig. B1 Geometry of an observer at P receiving a cylindrical wave from a line source at S and a reflected wave from the image source at S'.

Fig. B2 Integration path C for the incident and reflected waves in the complex θ -plane; saddle point θ_s with path of steepest descent C_s ; Rayleigh pole θ_k , Stoneley pole θ_s , and branch points θ_L, θ_r with corresponding branch cuts (dashed lines).

Fig. B3 Cylindrical wave from source S exciting Rayleigh wave at point A, which propagates along interface and reaches observation point P by radiating into fluid at point B.

Fig. B4 Cylindrical wave from source S exciting longitudinal or transverse lateral wave at point A, which propagates along interface and reaches observation point P by radiating into fluid at point B.

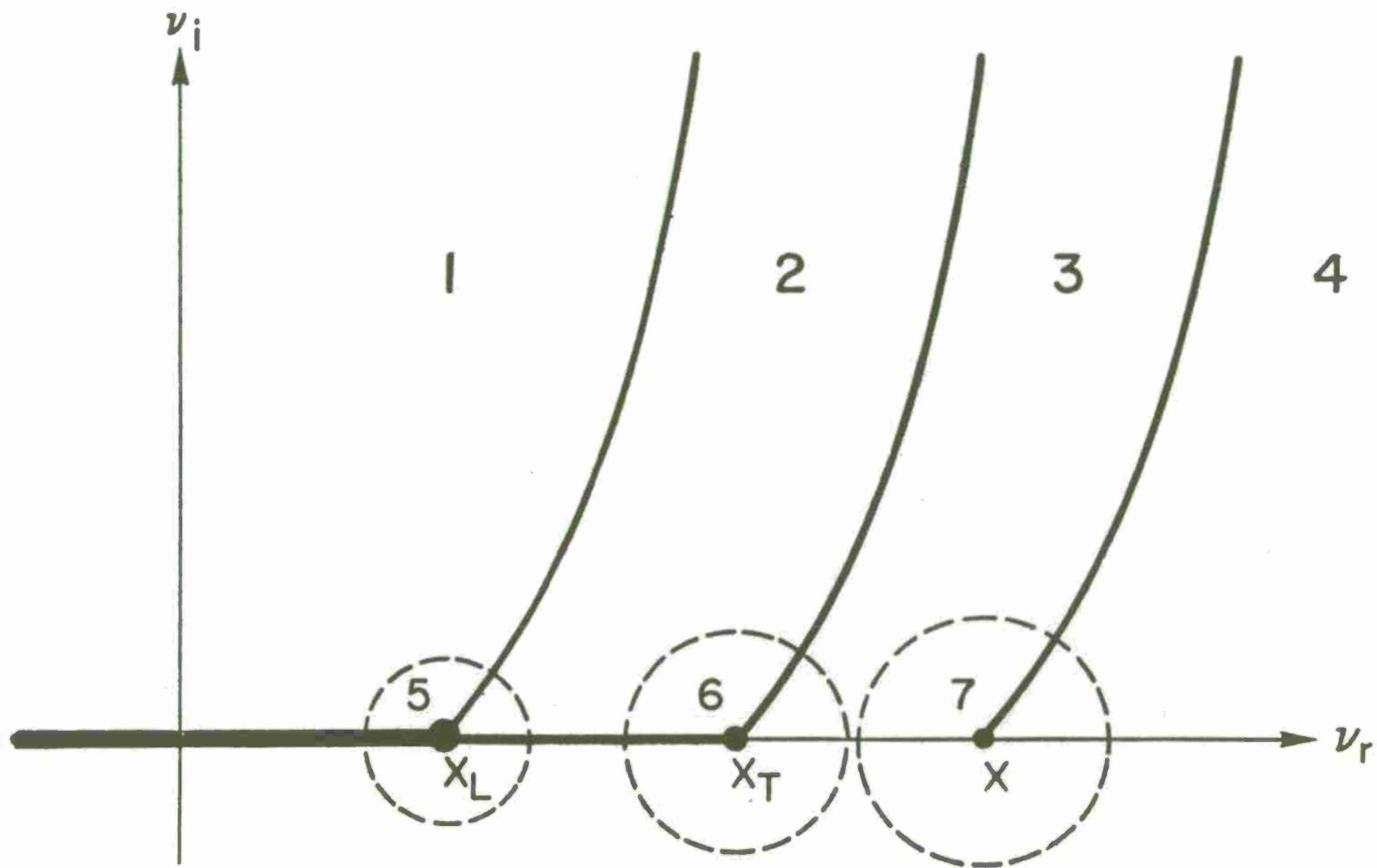
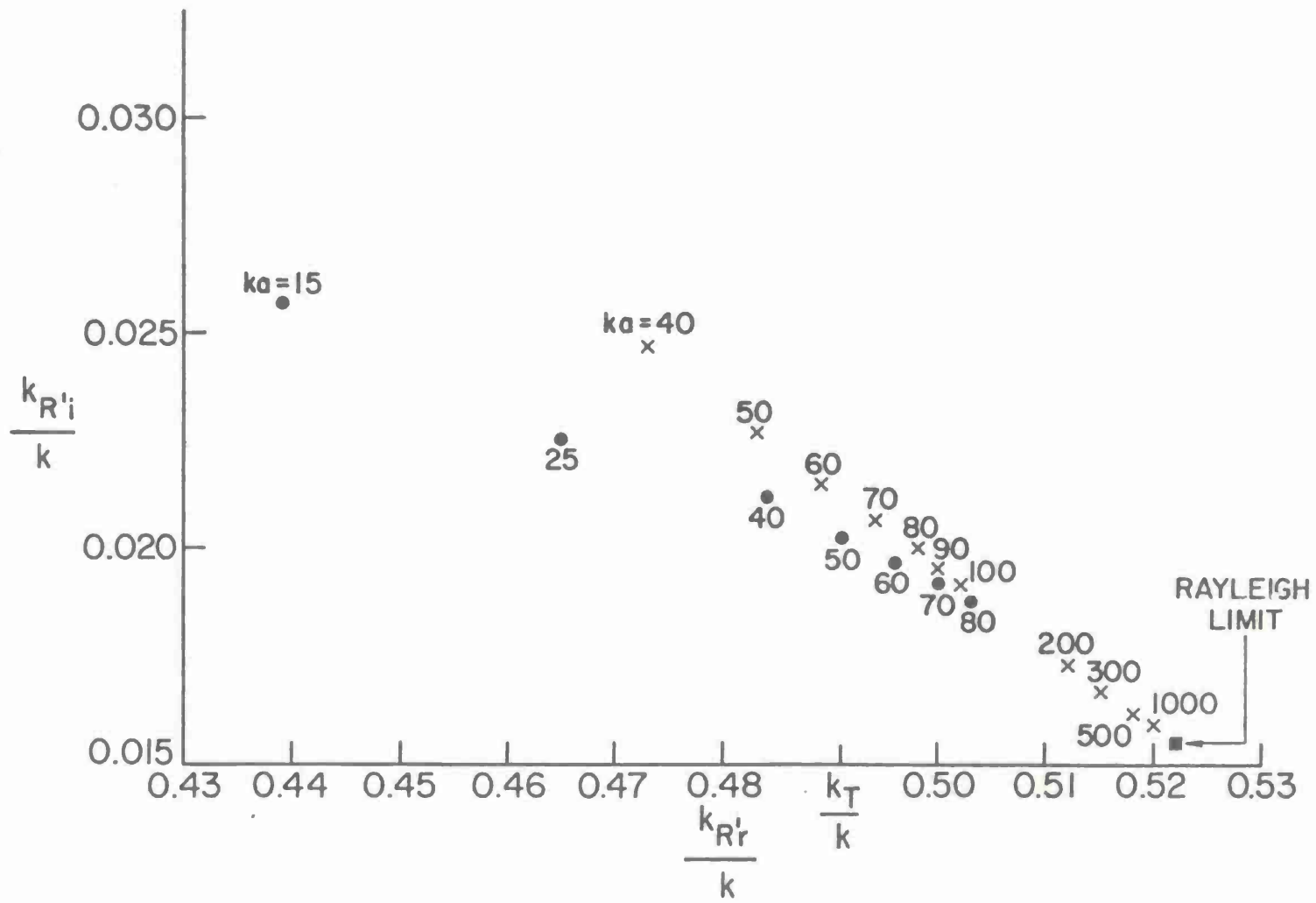


Fig. 1



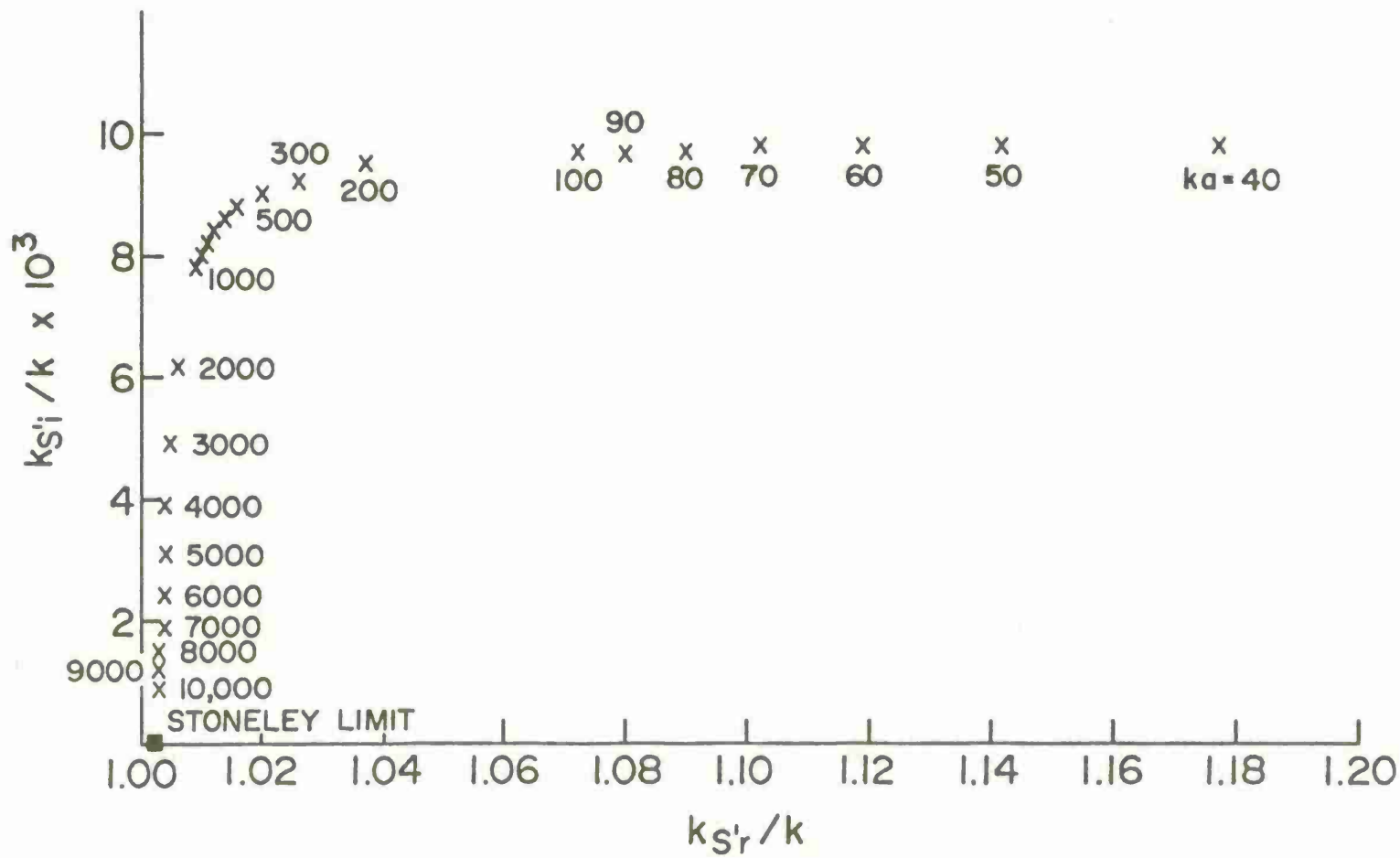
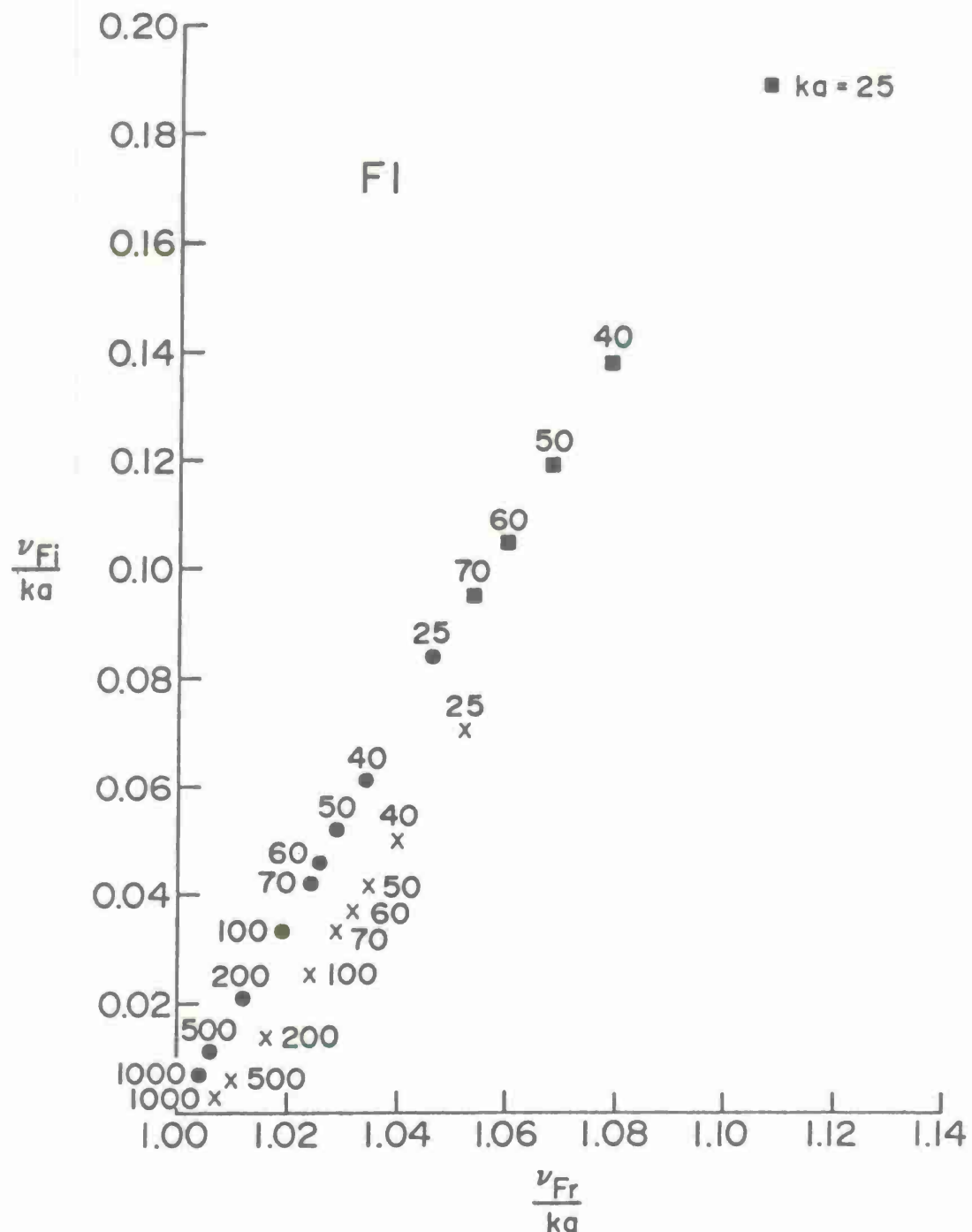
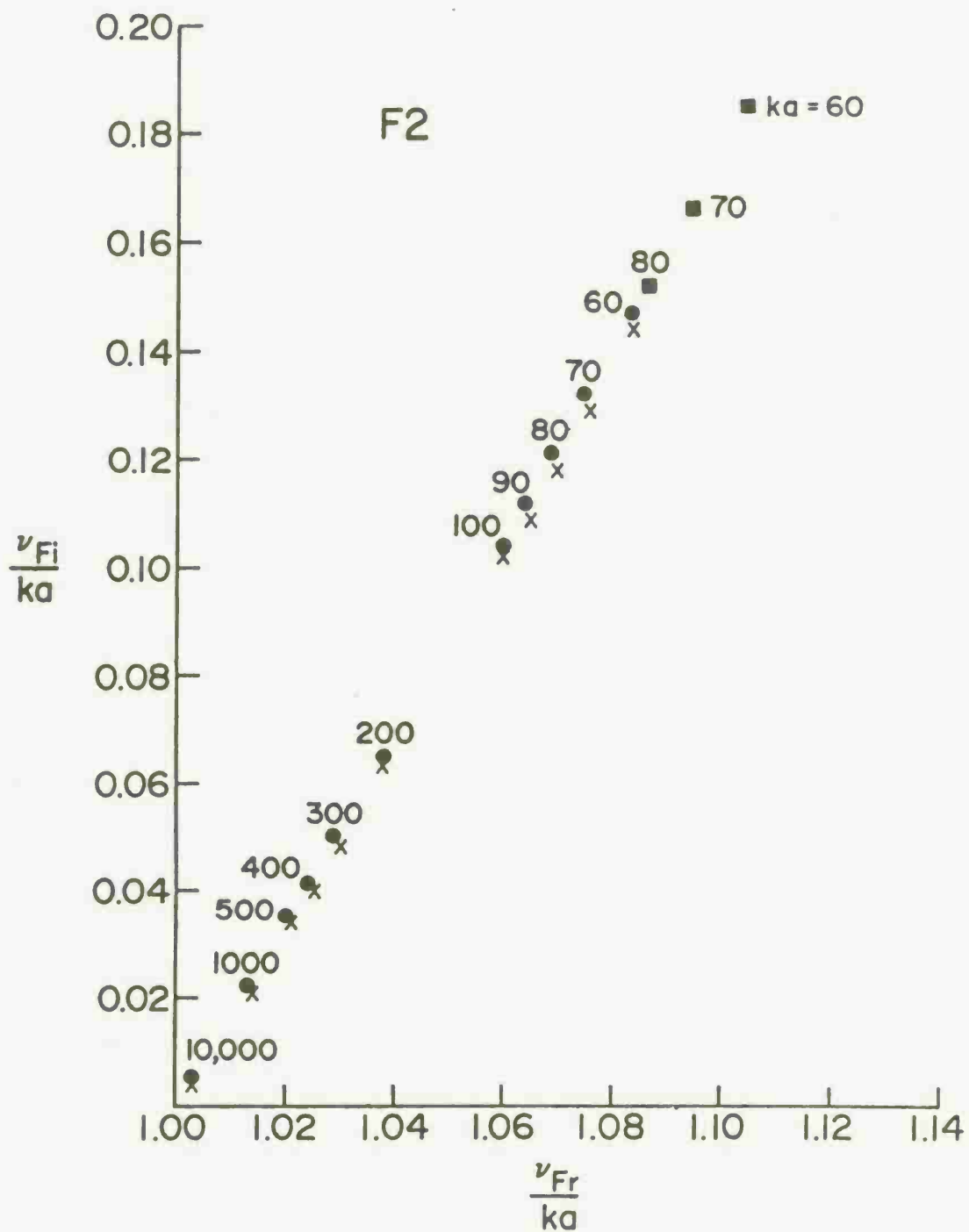
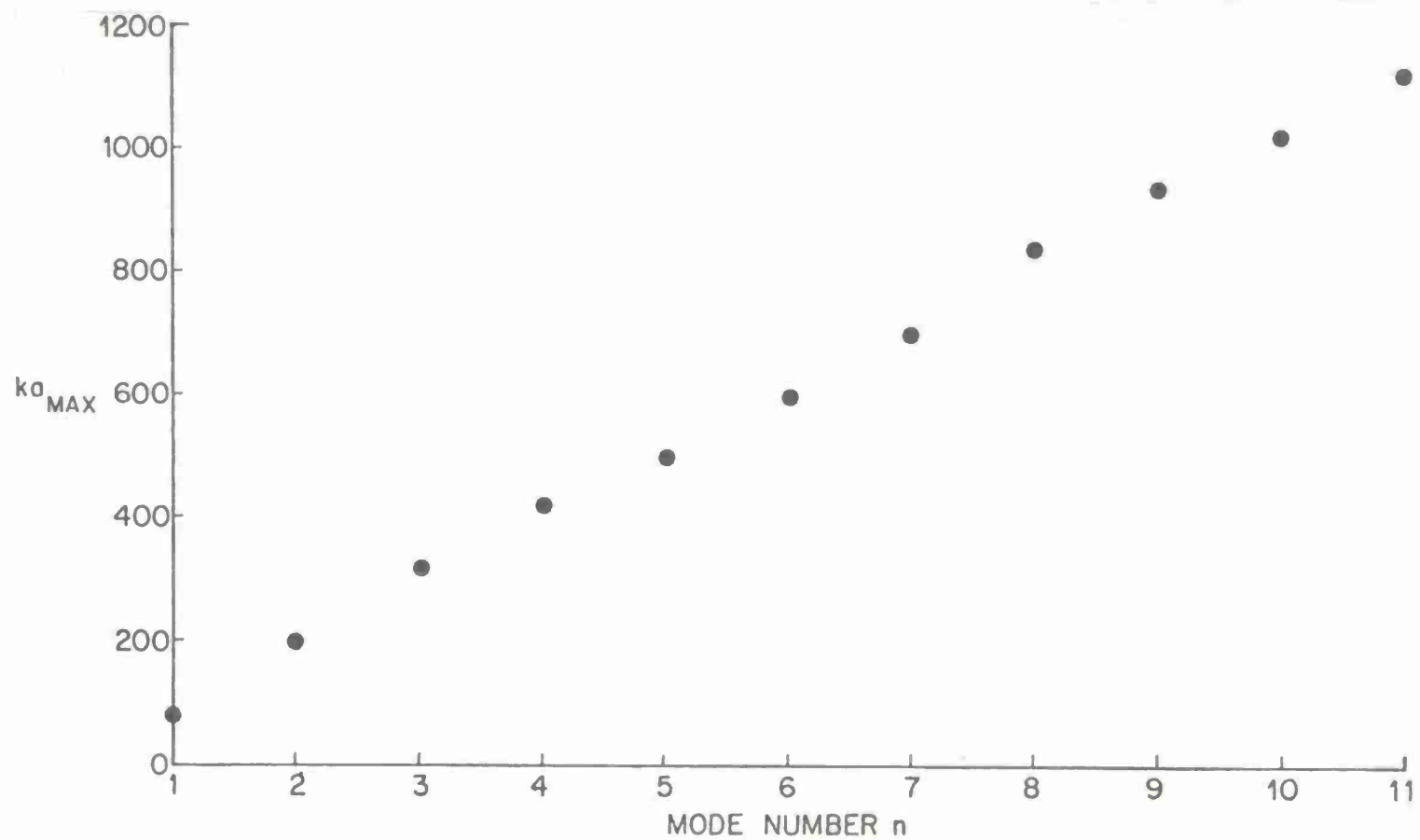


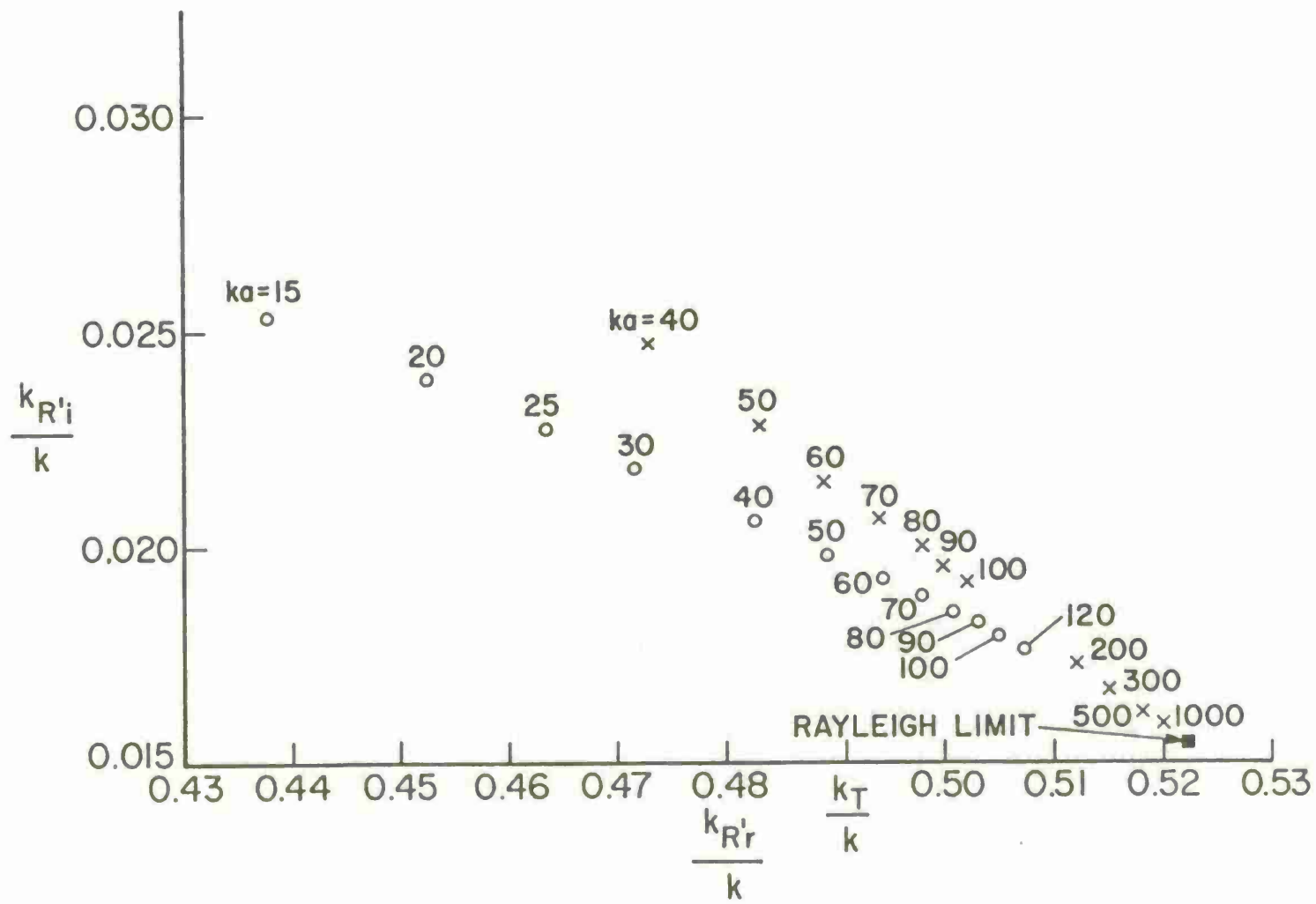
Fig. 3

Fig. 4a









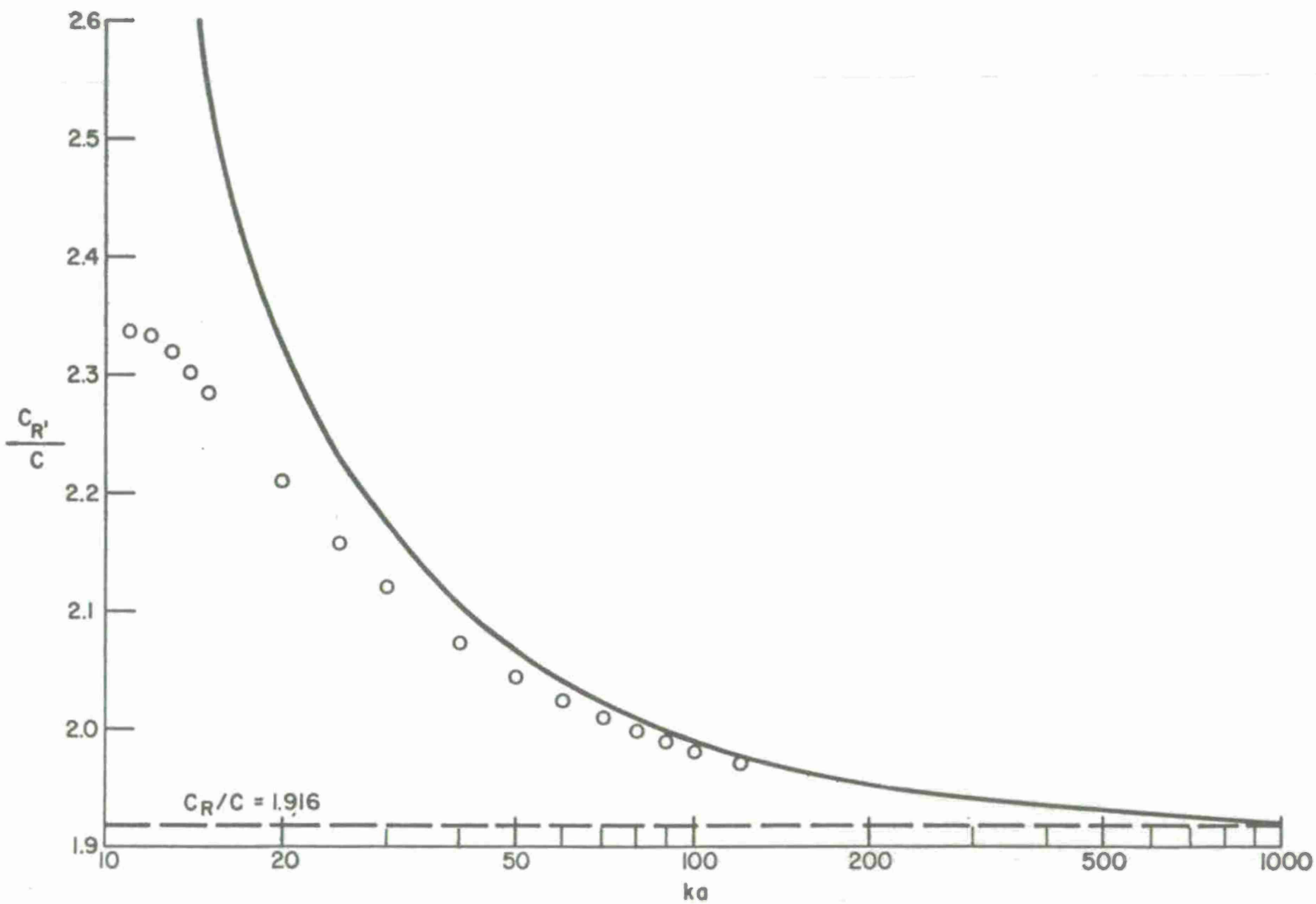
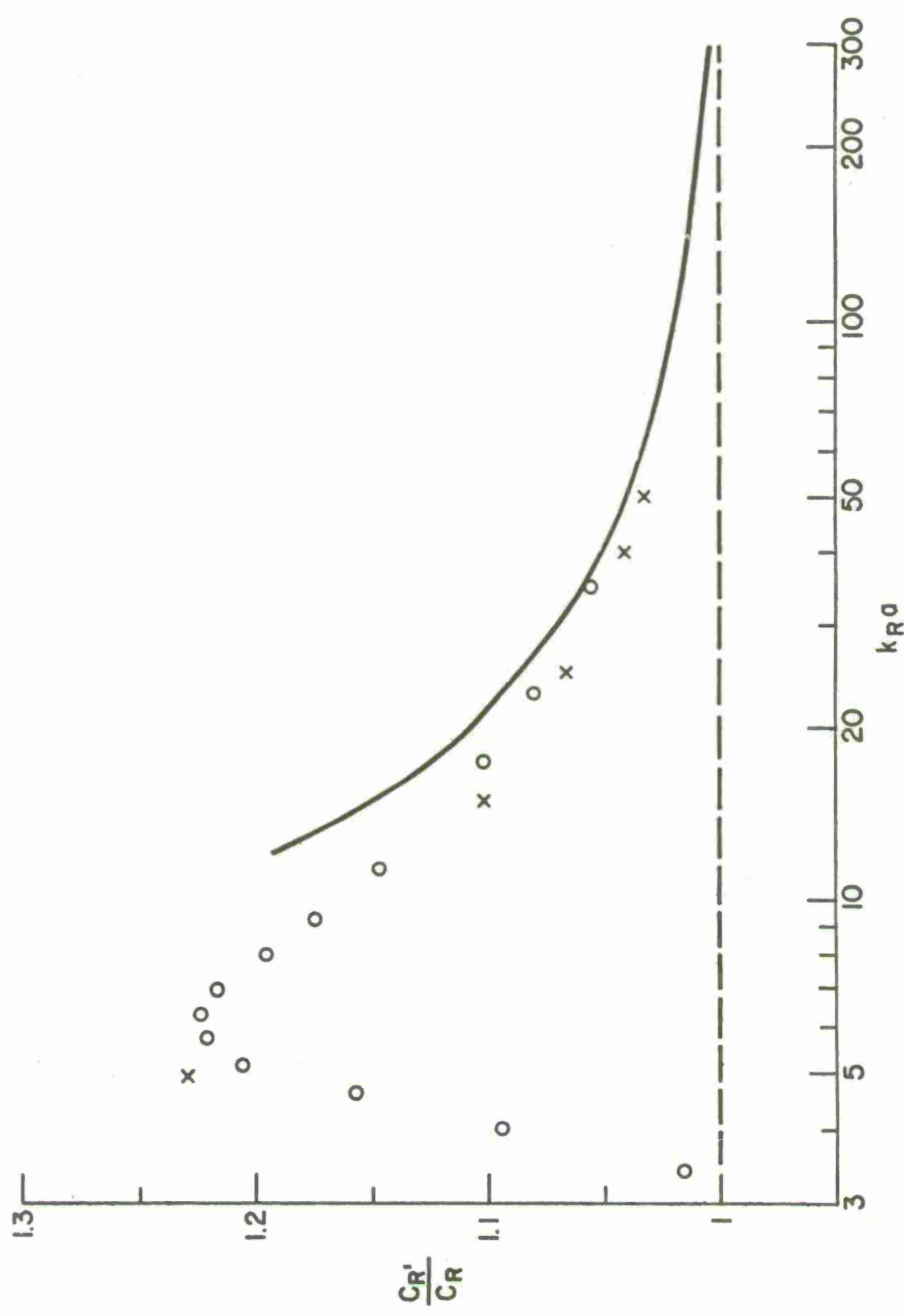
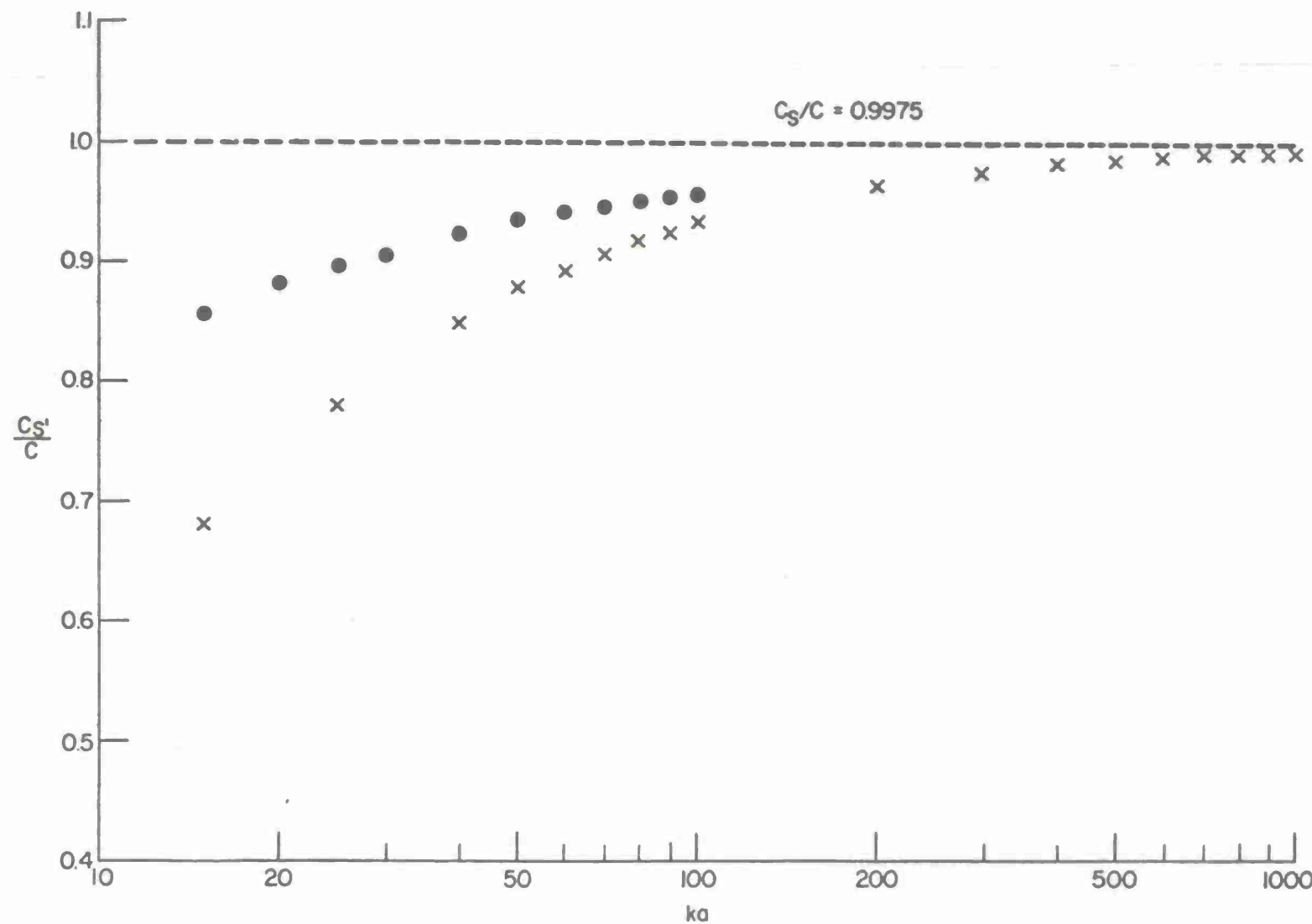


Fig. 7b





73

Fig. 8

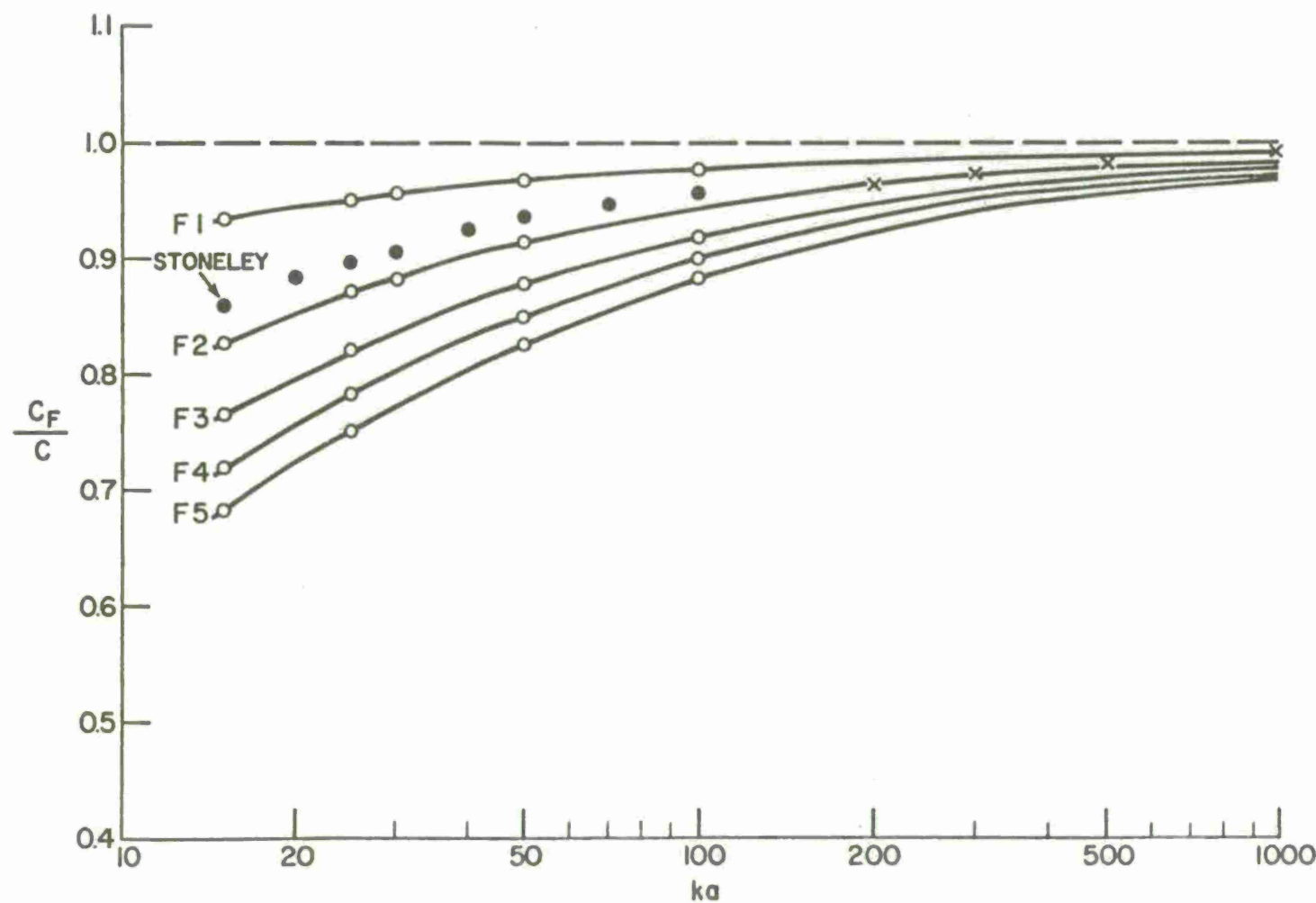
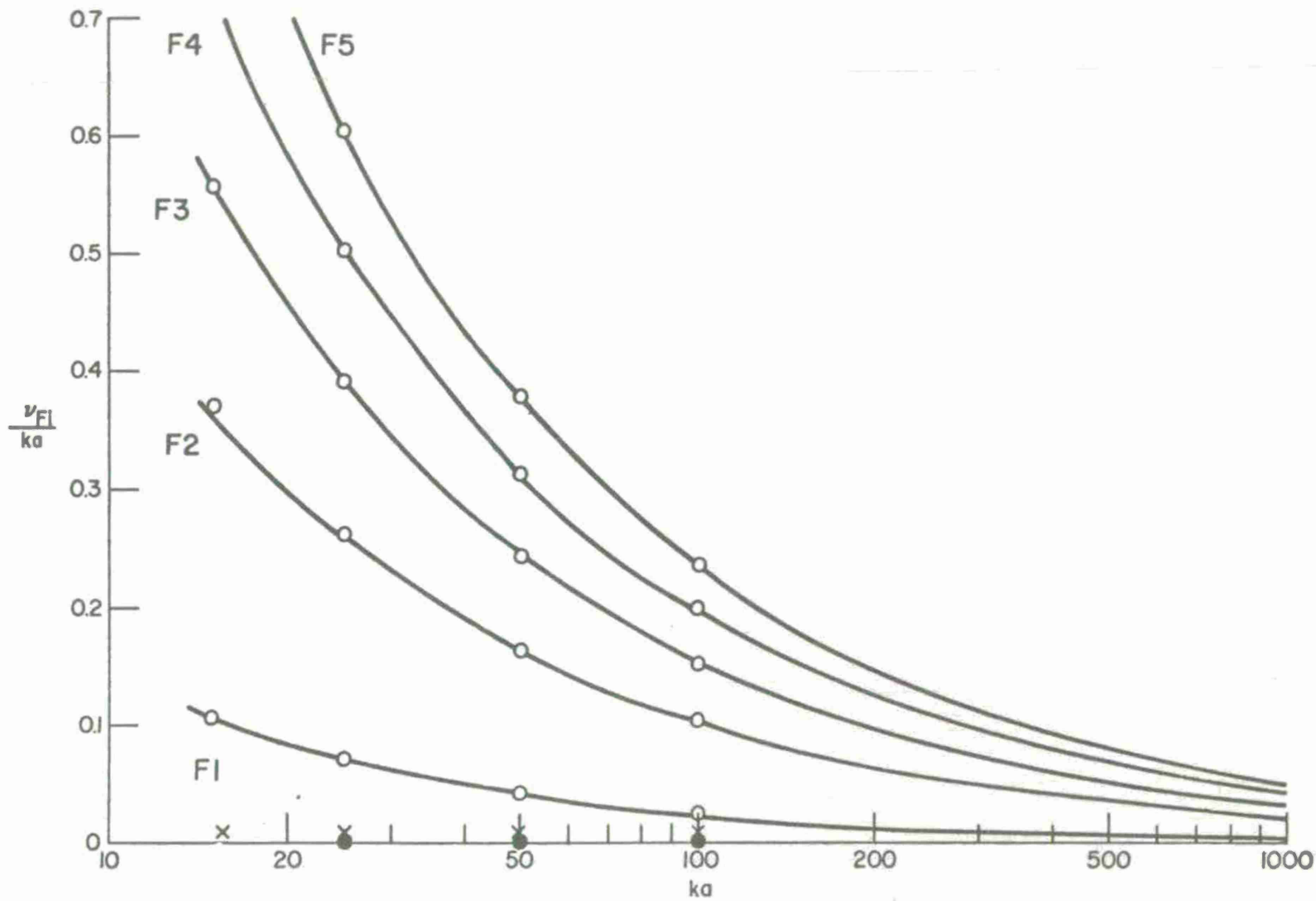
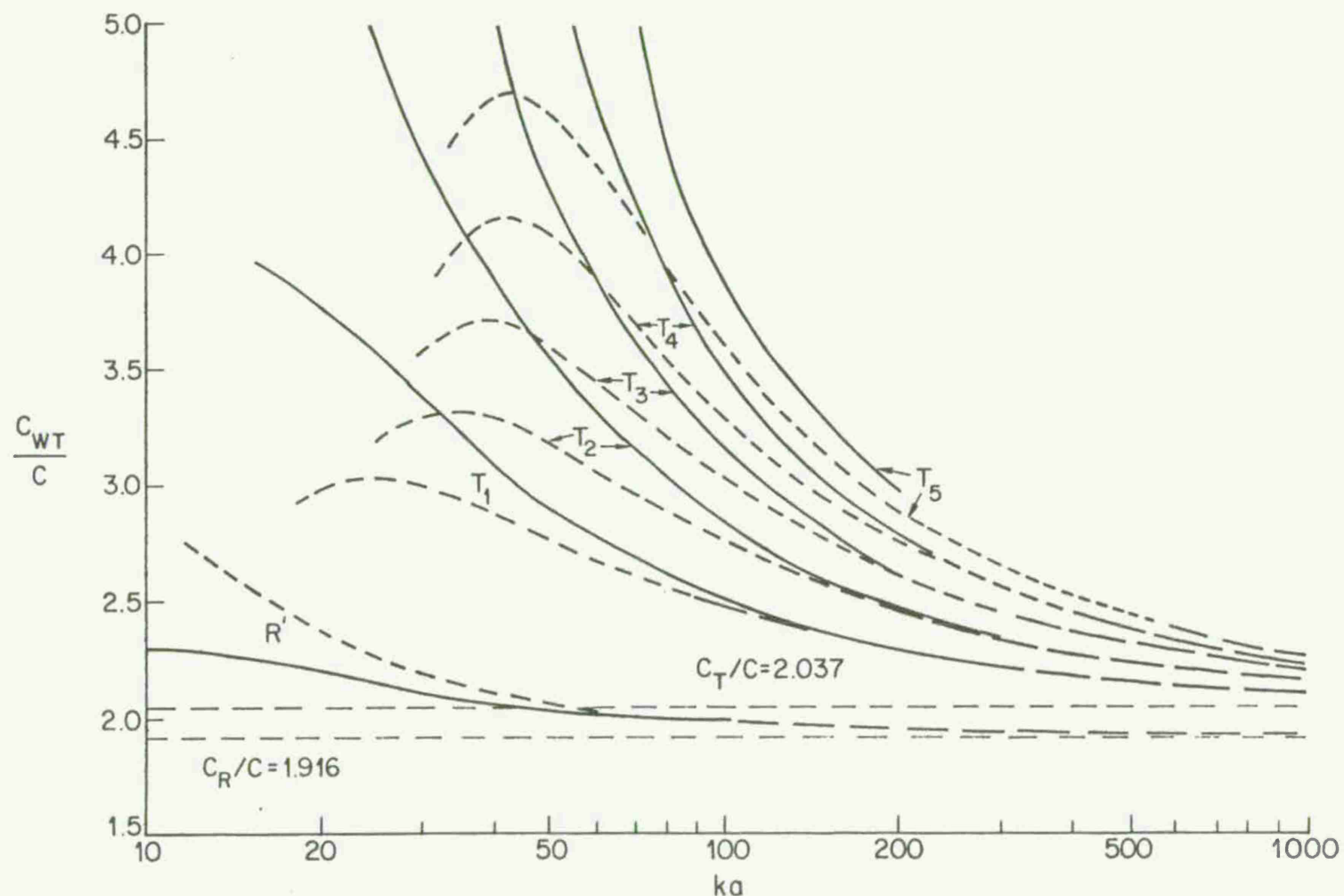


Fig. 9a





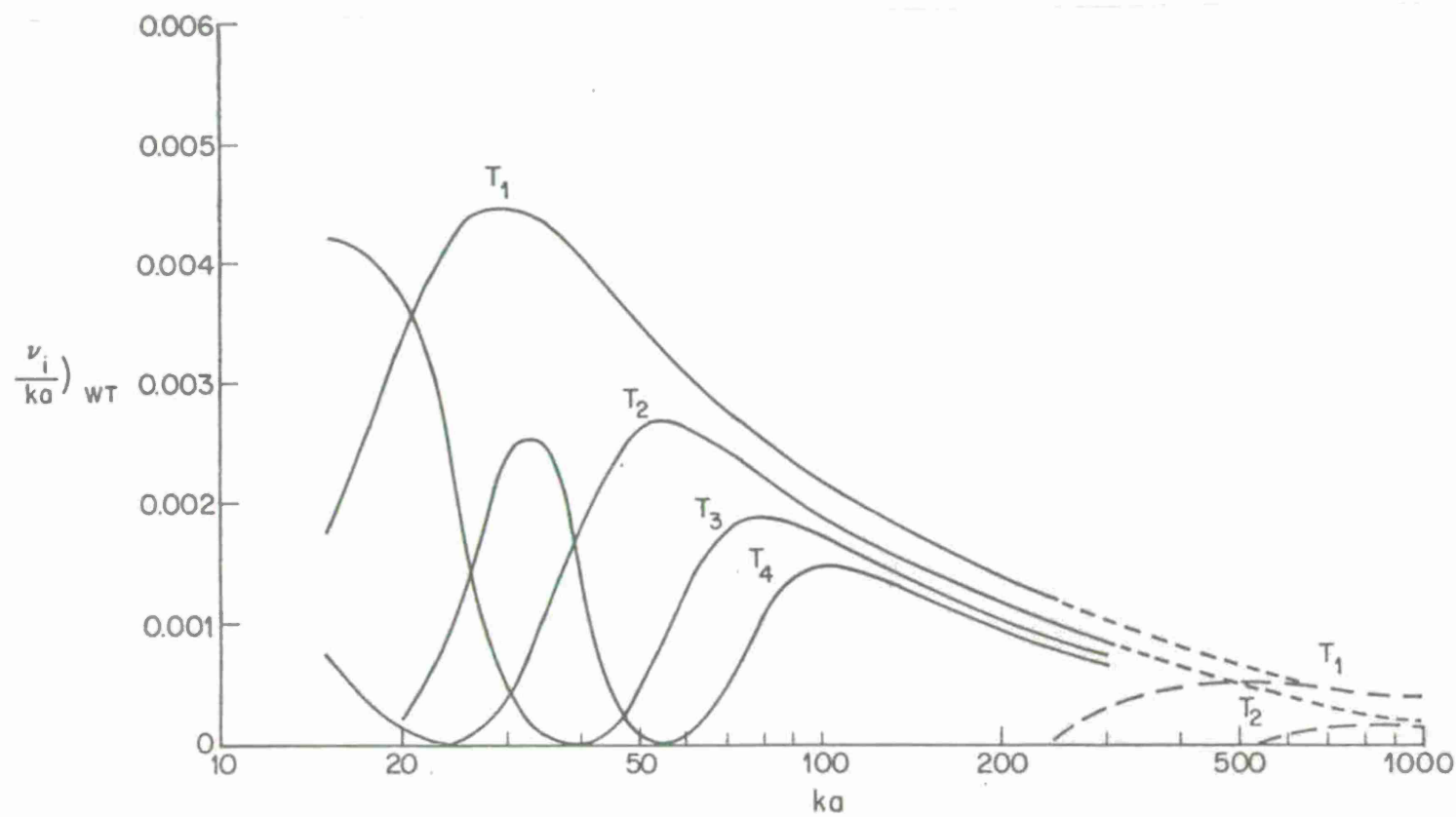


Fig. 10b

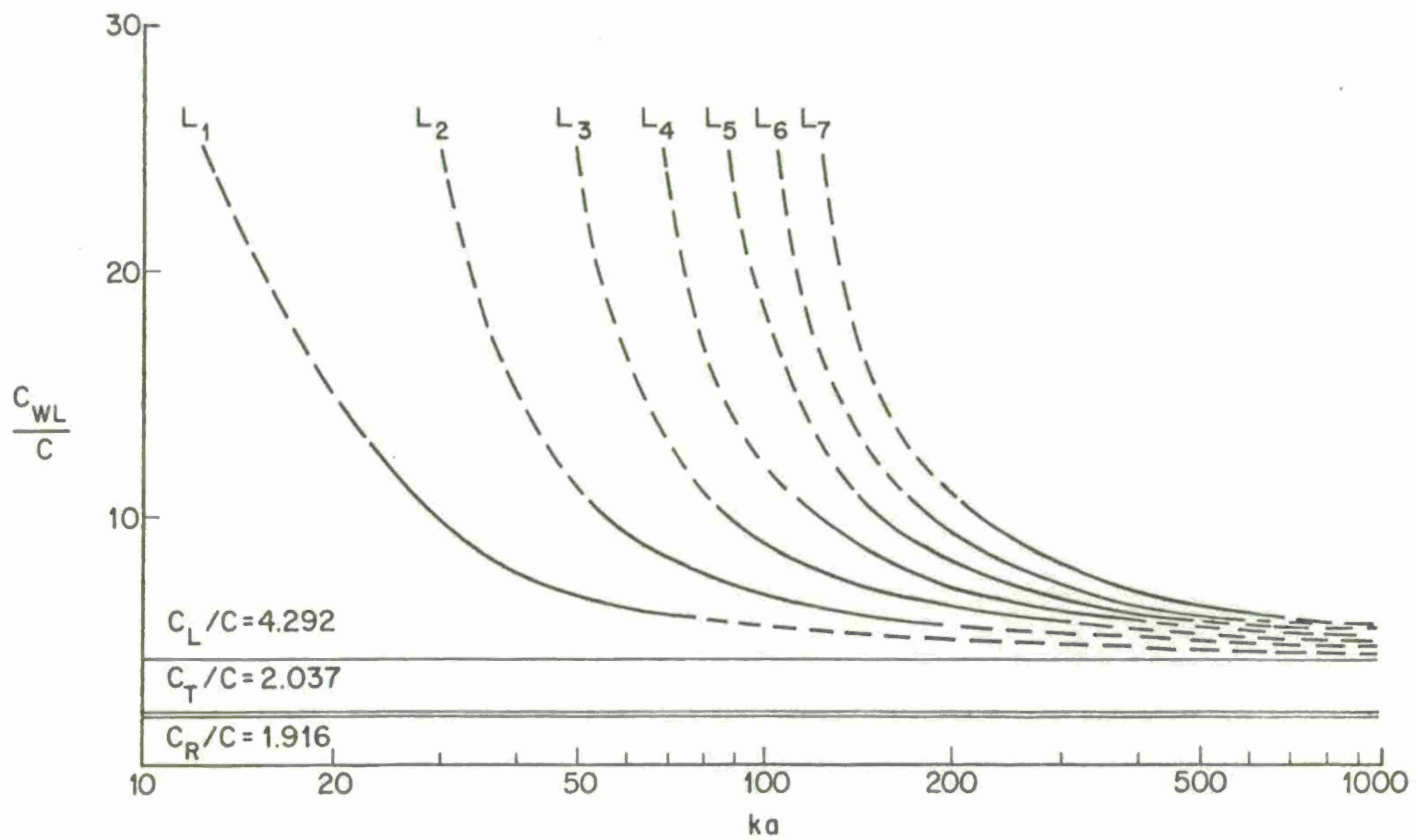
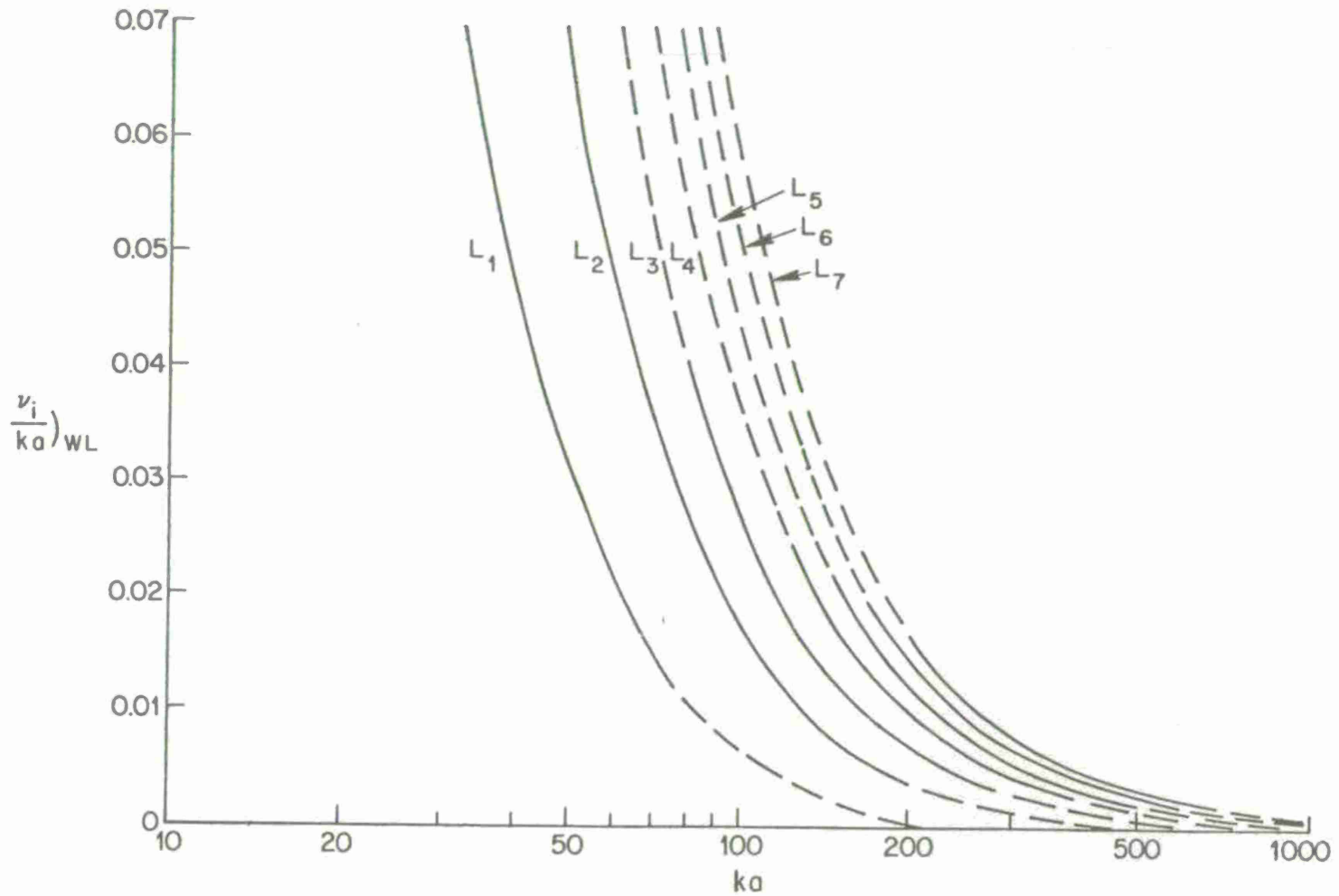
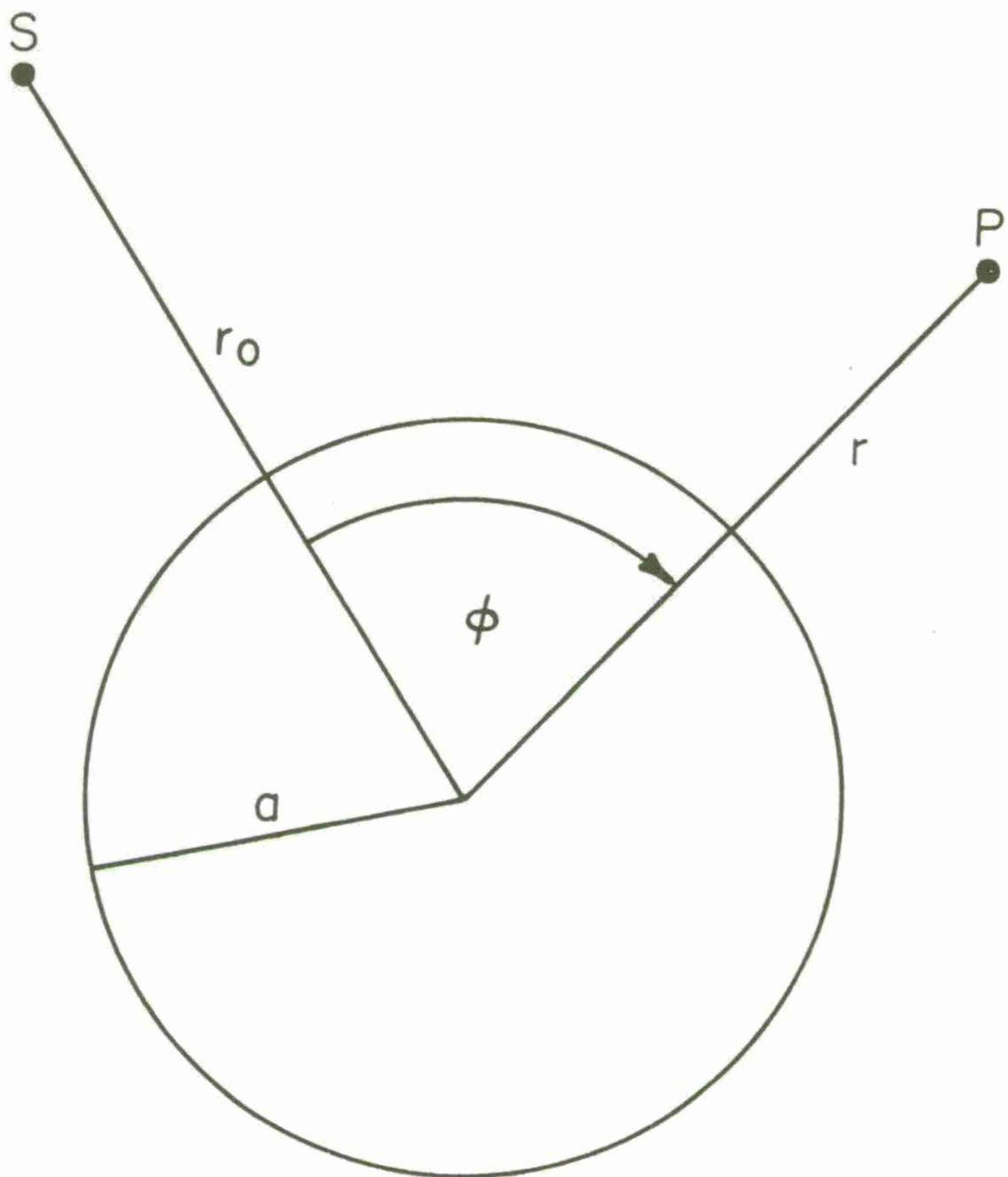
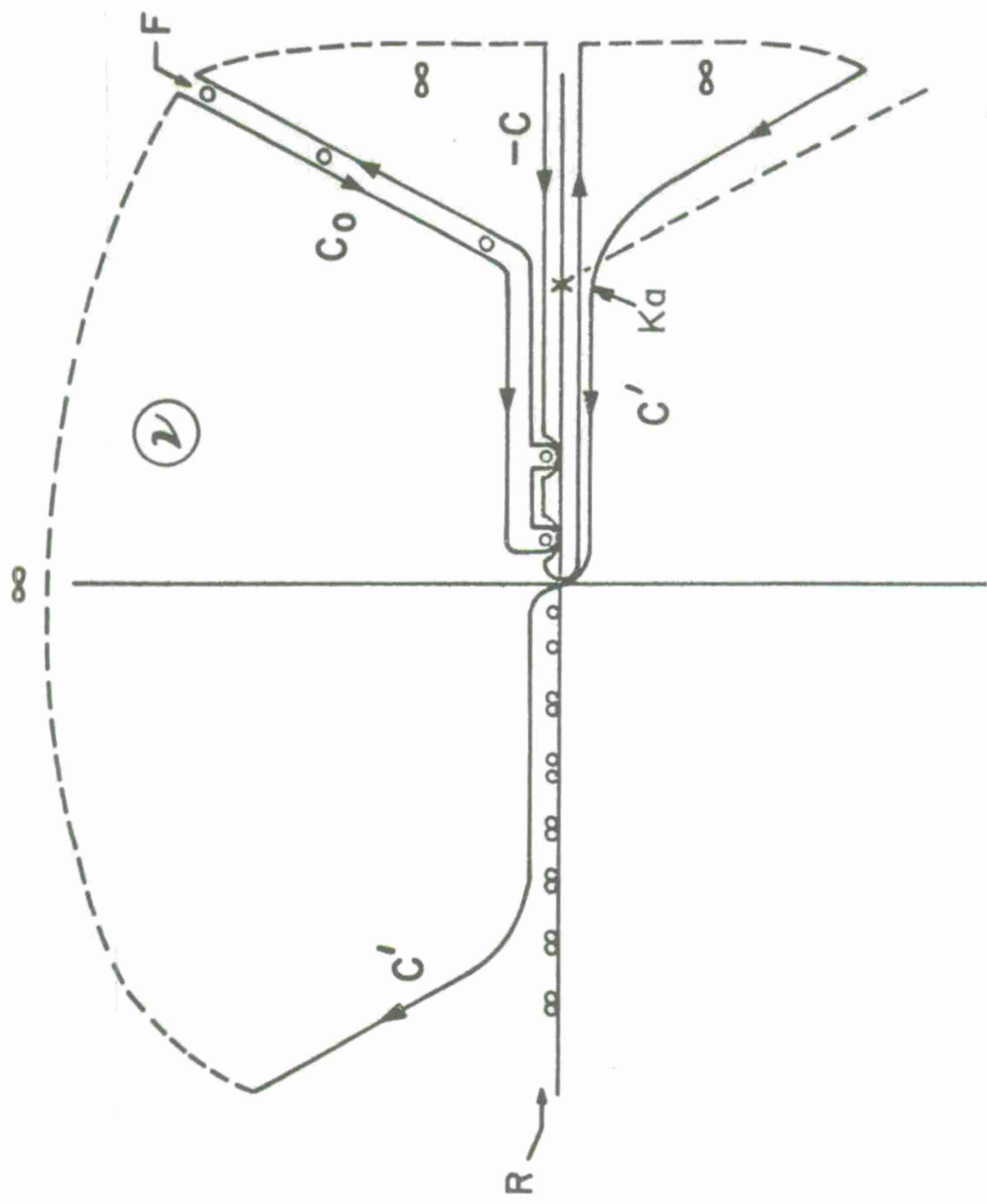


Fig. 11b







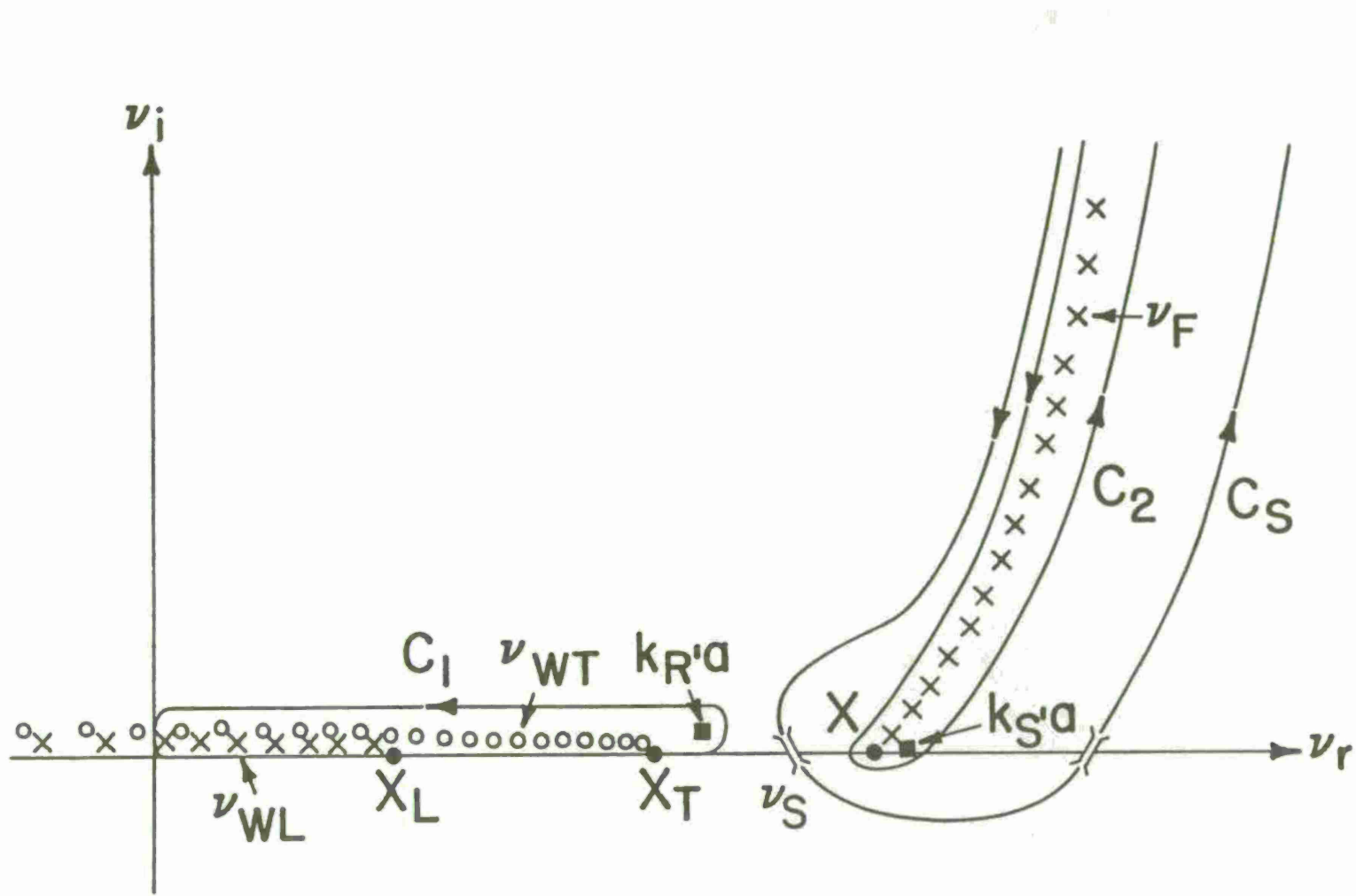
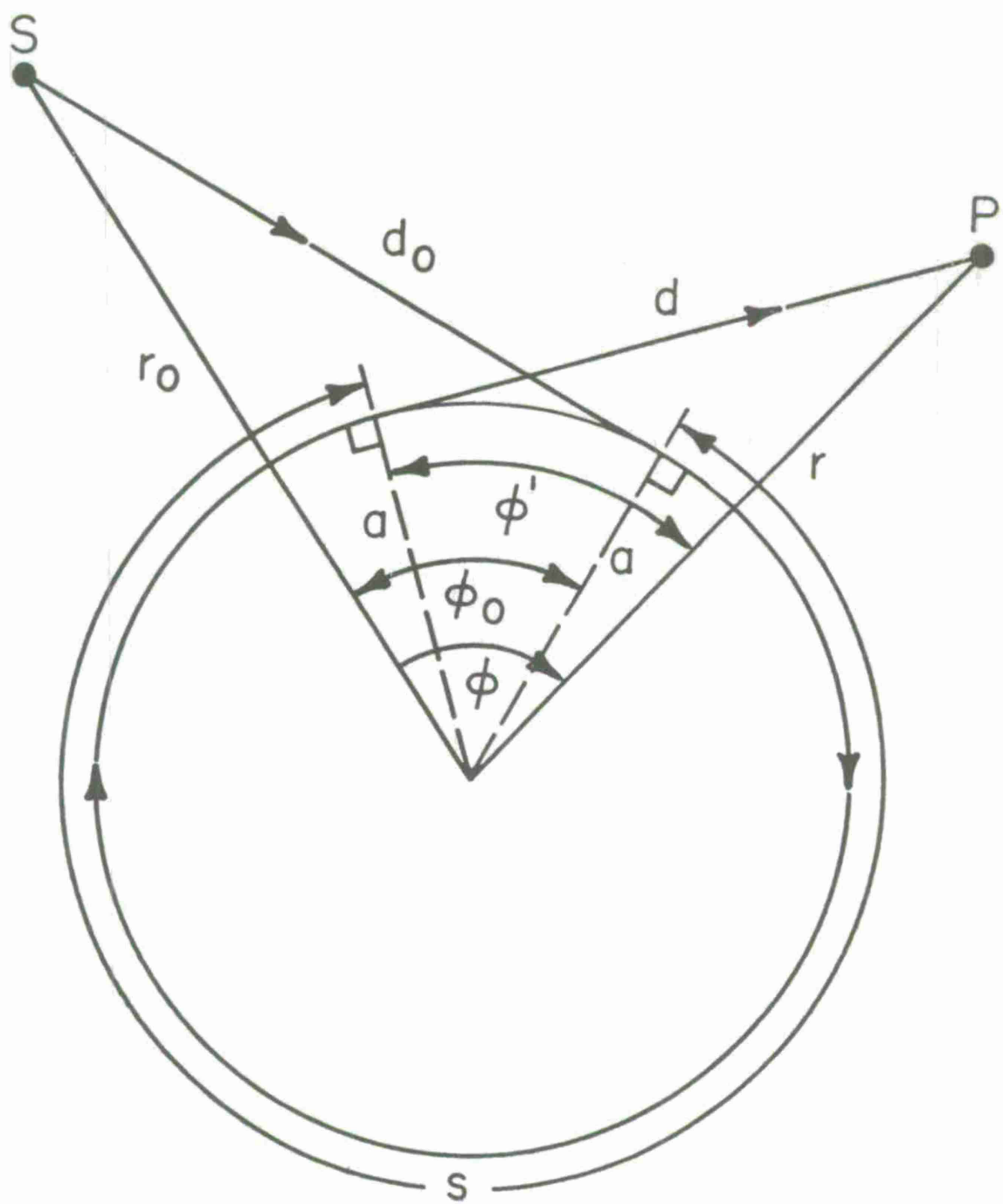
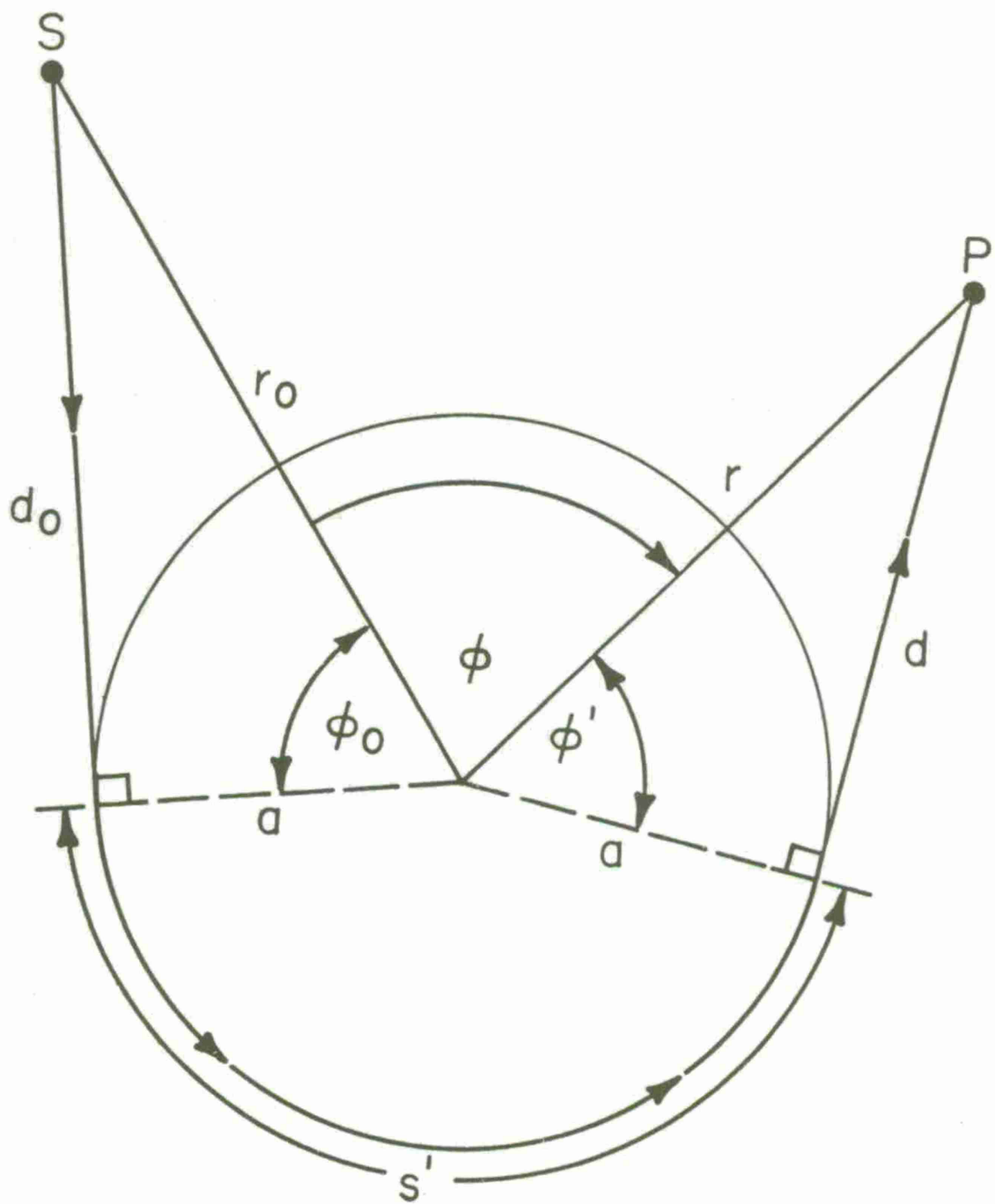
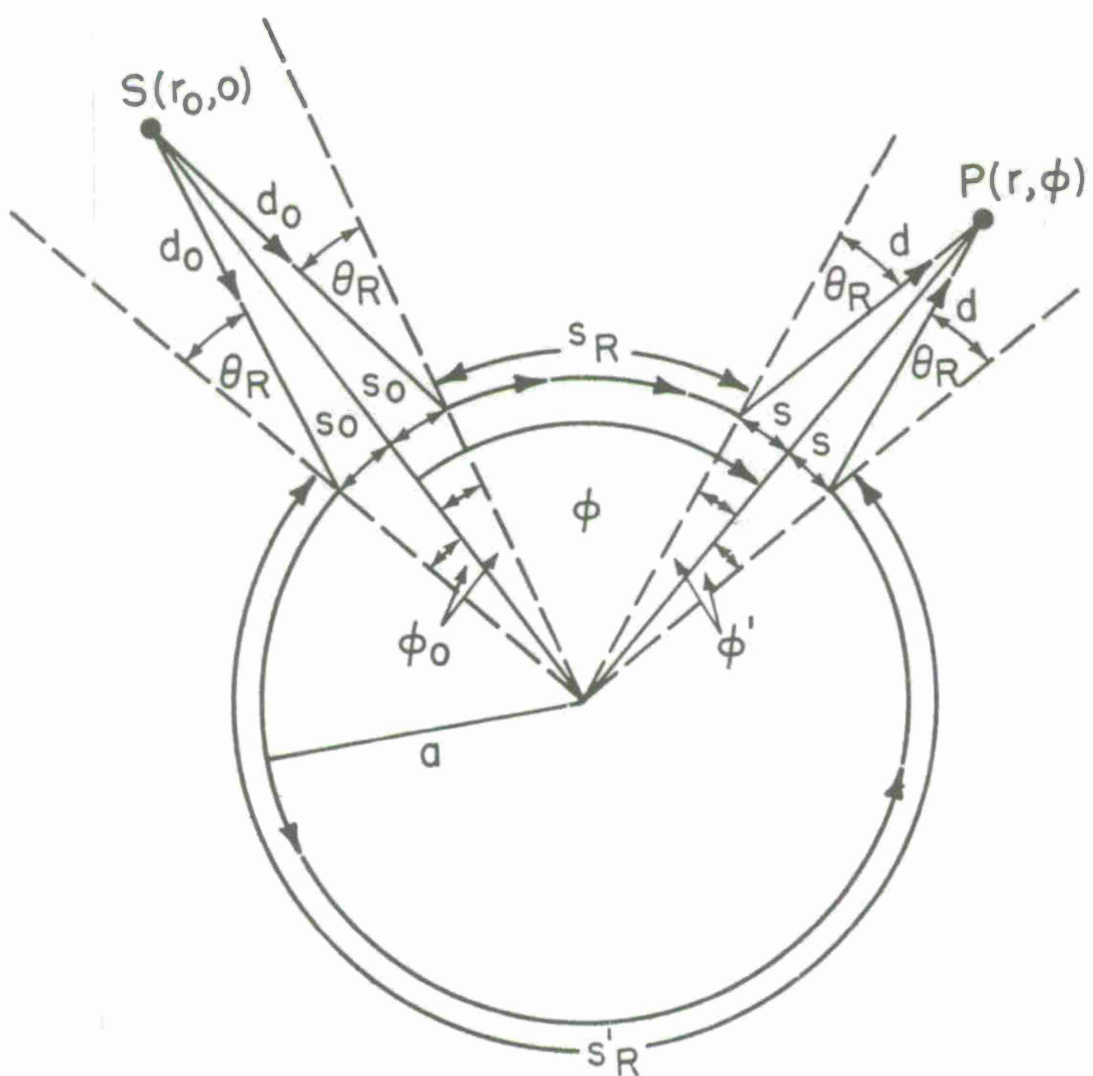
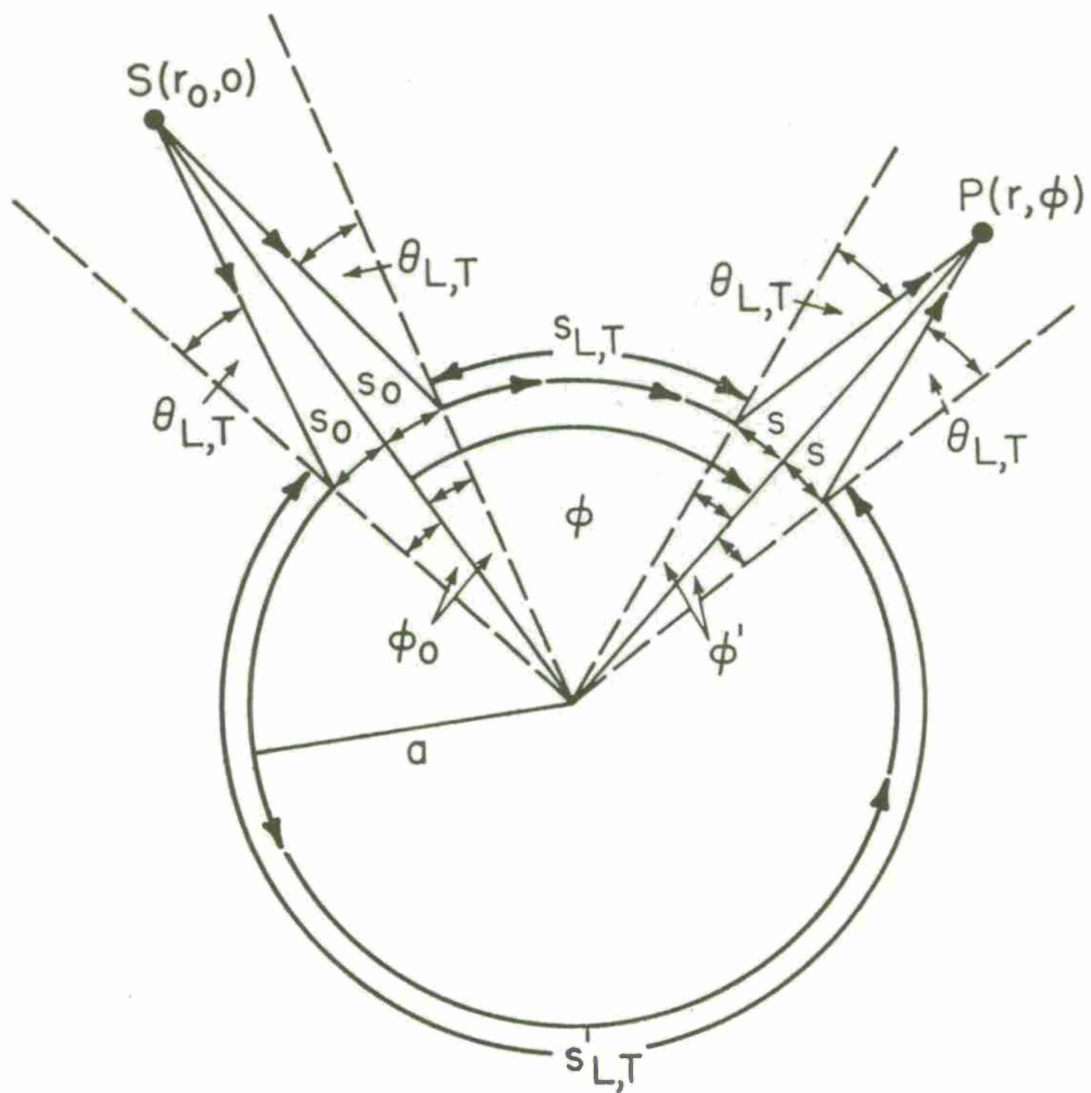


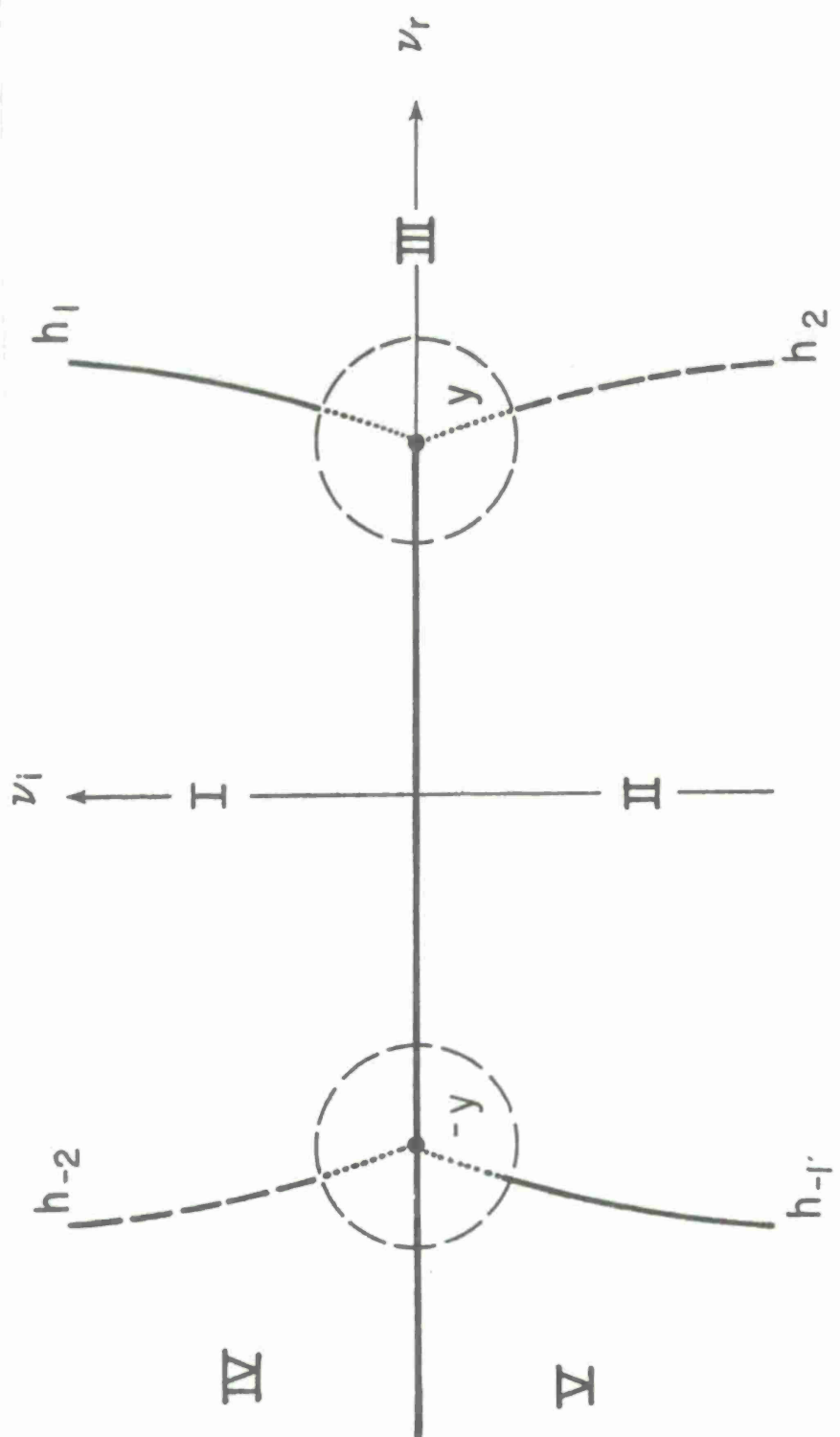
Fig. 14











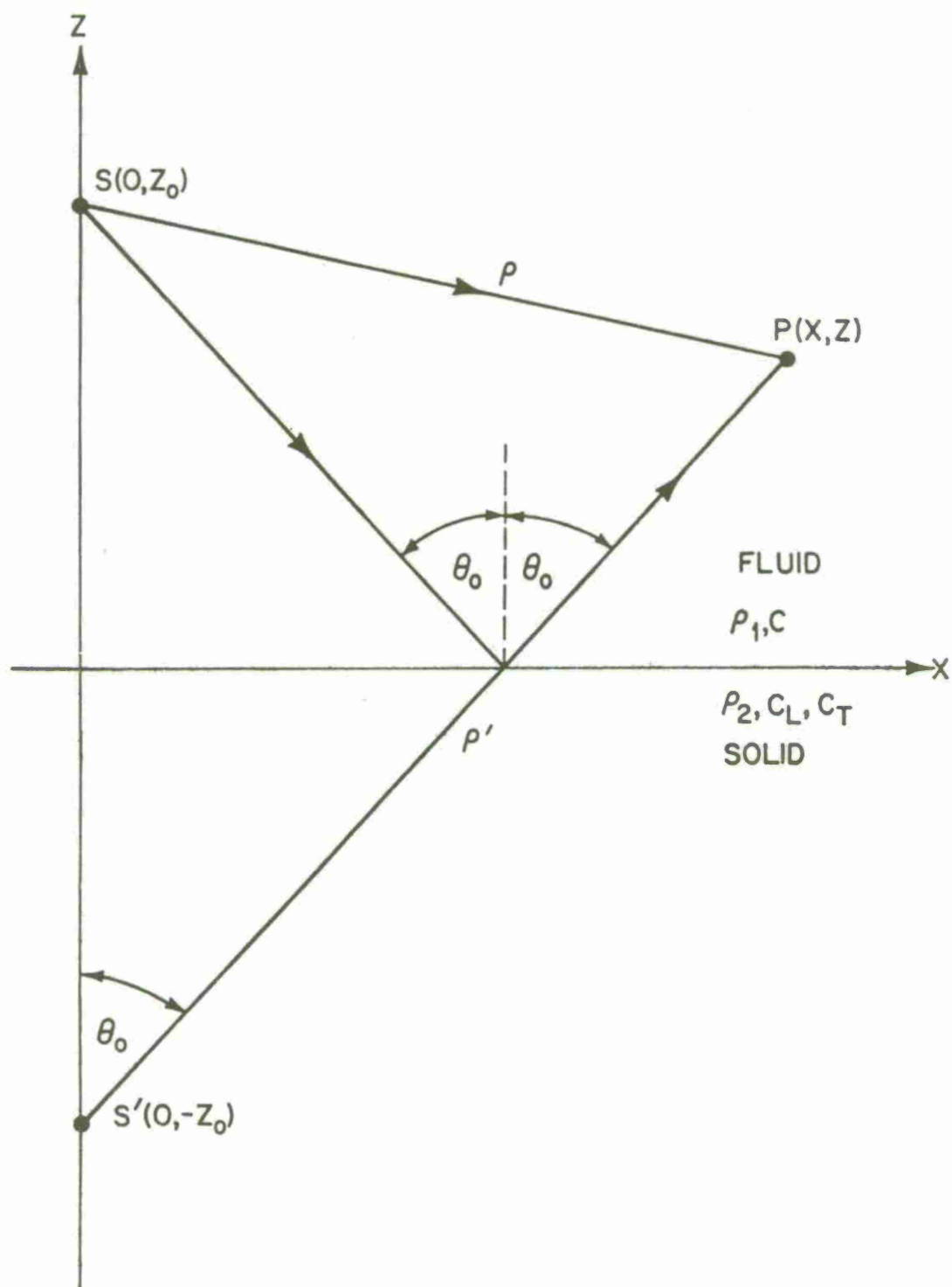
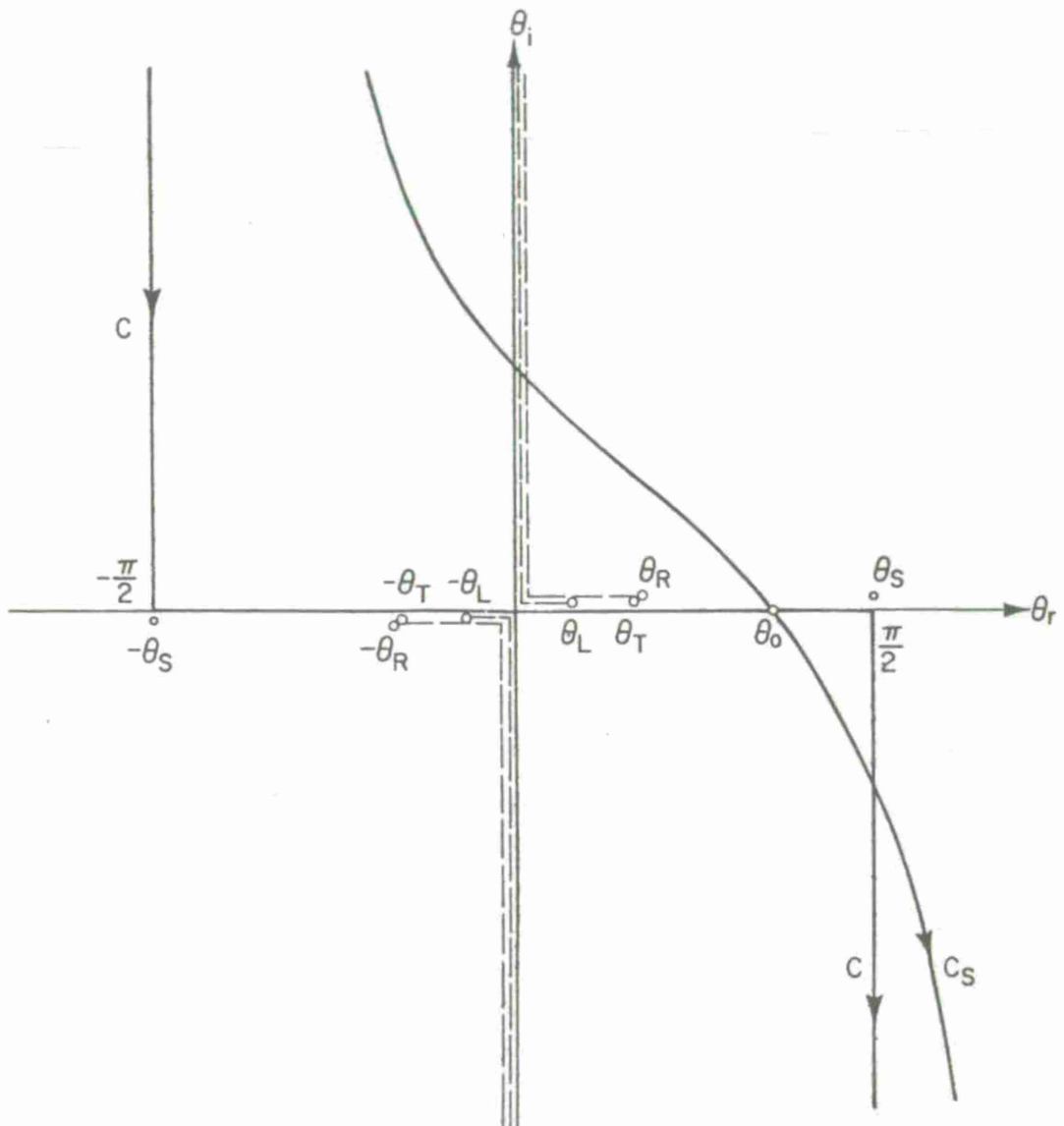
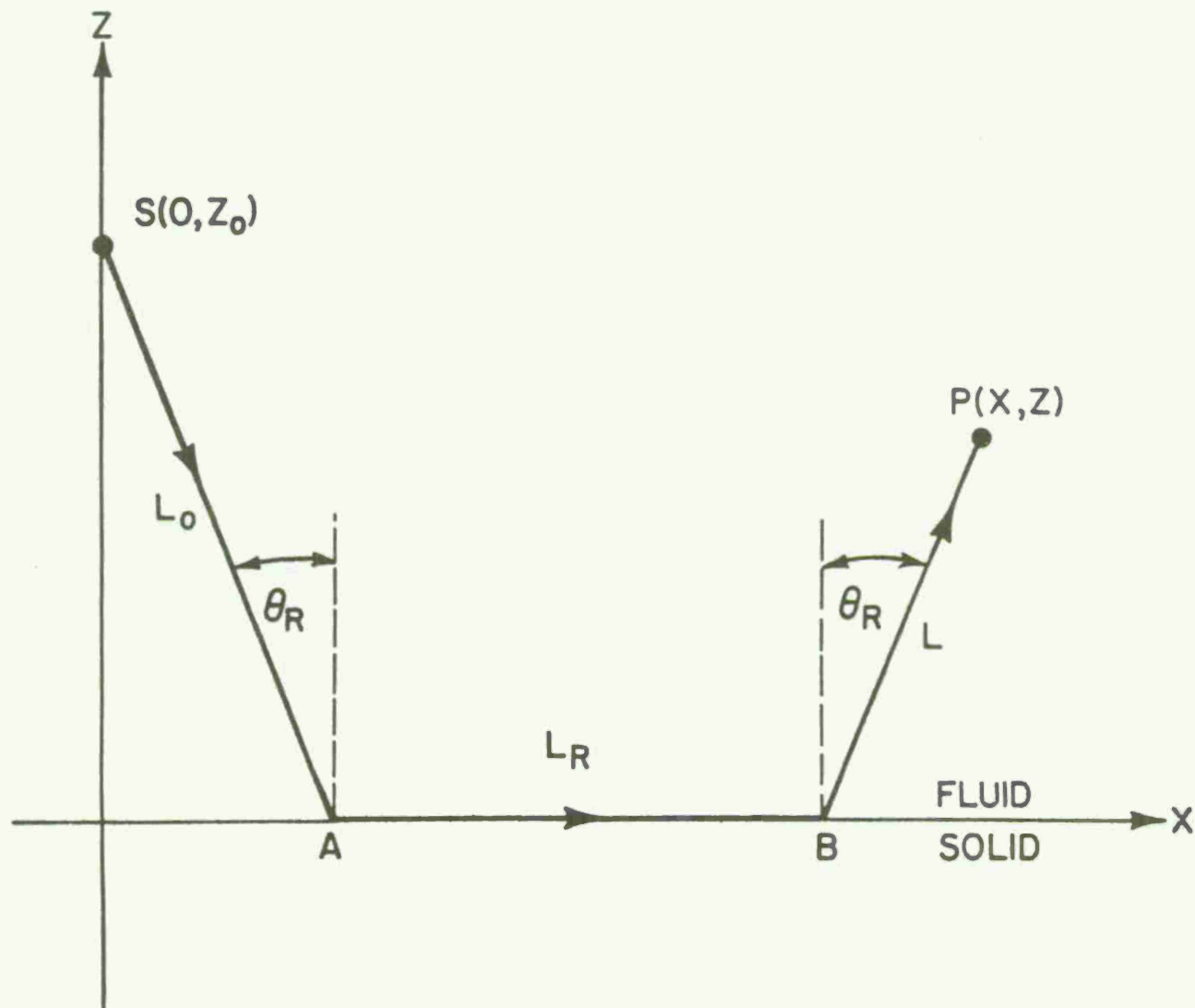
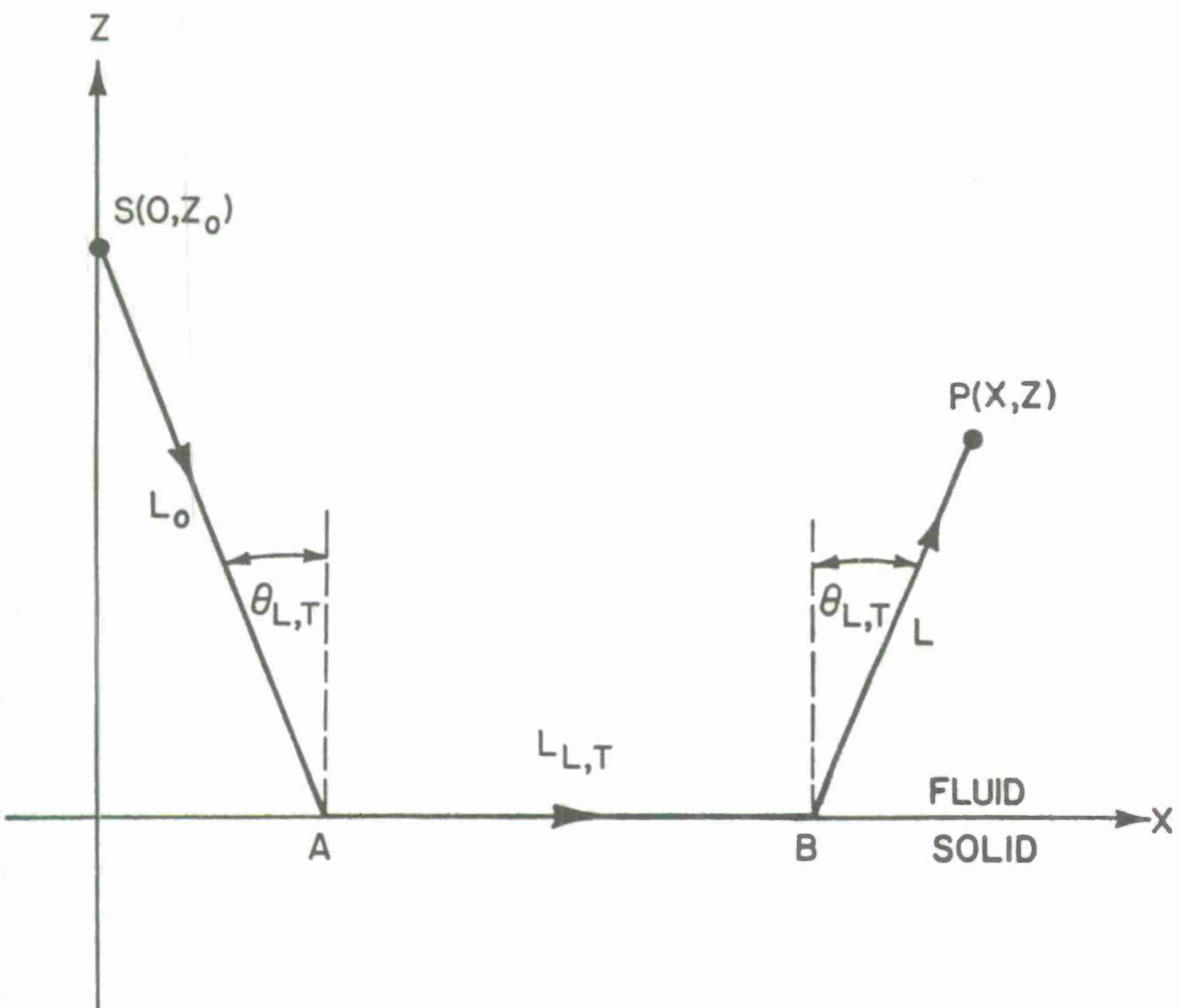


Fig. B2



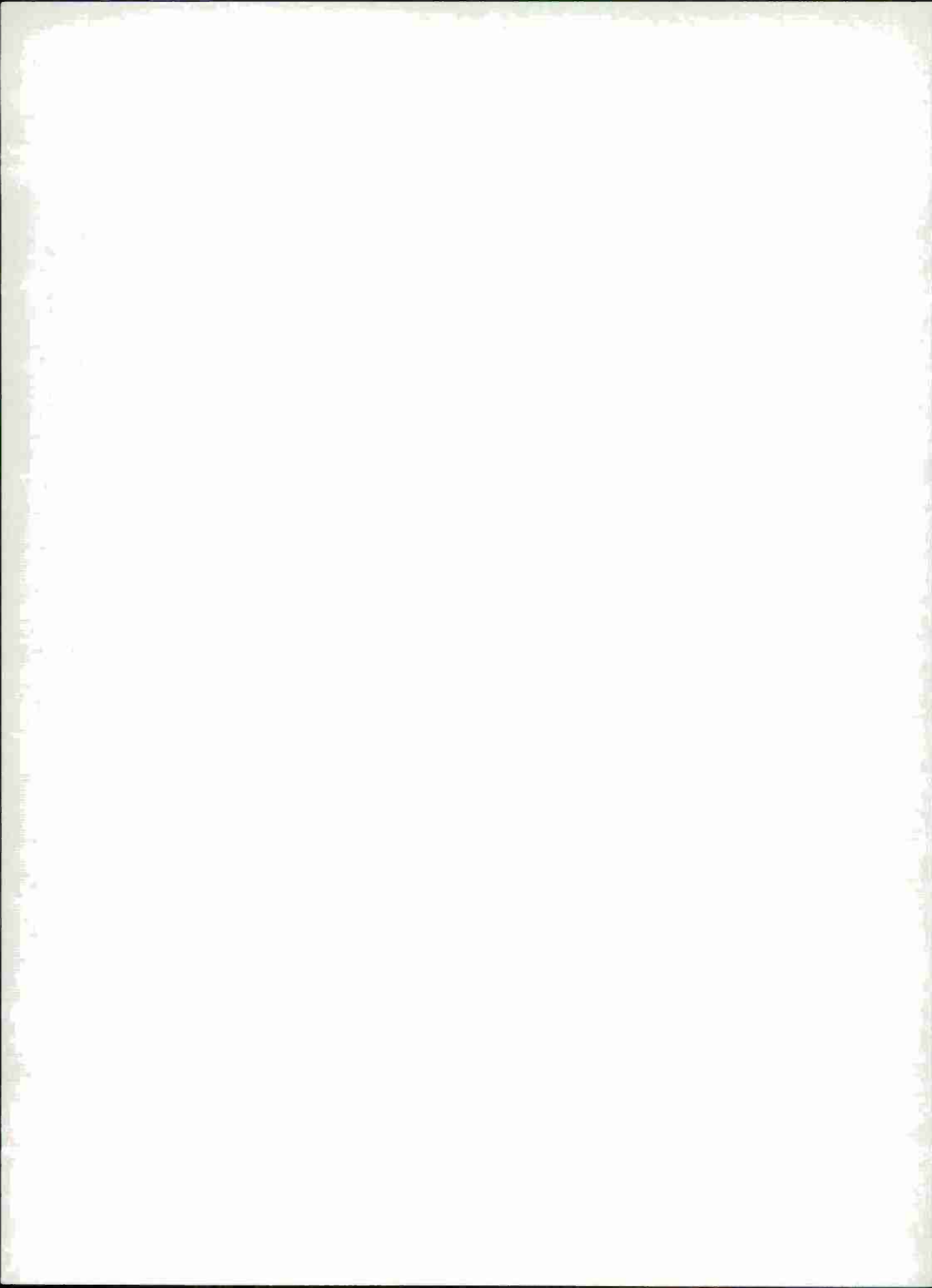


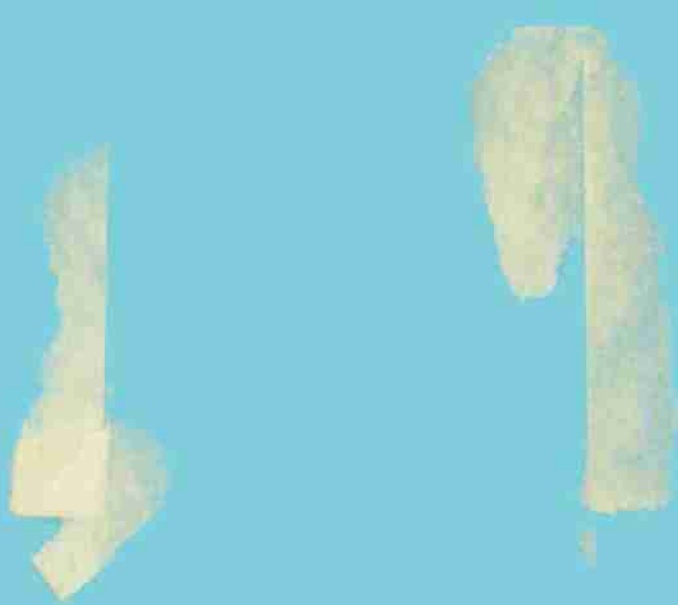


Bibliography

1. H. Überall, "Surface Waves in Acoustics," in Physical Acoustics, Vol. 10, W. P. Mason and R. N. Thurston, editors (Academic Press, New York, 1973).
2. L. M. Brekhovshikh, Waves in Layered Media (Academic Press, New York, 1960).
3. R. Stoneley, Proc. Roy. Soc. (London) A 106, 416-428 (1924).
4. R. D. Doolittle, H. Überall, and P. Uginčius, J. Acoust. Soc. Am. 43, 1-14 (1968).
5. O. D. Grace and R. R. Goodman, J. Acoust. Soc. Am. 39, 173-174 (1966).
6. A. D. Lapin, Soviet Phys.-Acoust. 15, 201-204 (1969).
7. W. Franz, Zeits. Naturforsch. 9a, 705-716 (1954).
8. I. A. Viktorov, Soviet Phys.-Acoust. 4, 131-136 (1958).
9. P. Uginčius, Thesis, The Catholic University of America, Washington, D.C. (1968); NWL Report TR-2128, U.S. Naval Weapons Laboratory, Dahlgren, Va. (1968).
10. E. Strick and A. S. Ginzburg, Bull. Seis. Soc. Am. 46, 281-292 (1956).
11. J. A. Cochran, Numer. Math. 7, 238-250 (1965).
12. A Sommerfeld, Partial Differential Equations in Physics (Academic Press, New York, 1949).
13. W. Streifer and R. D. Kodis, Quart. Appl. Math. 21, 285-298 (1964).
14. W. Streifer and R. D. Kodis, Quart. Appl. Math. 23, 27-38 (1965).
15. W. Streifer, IEEE Trans. Antennas Propagation AP-12, 764-766 (1964).
16. J. W. Dickey, Naval Ship Research and Development Center, Annapolis, Maryland (private communication).
17. G. N. Watson, A Treatise on the Theory of Bessel Functions (Cambridge University Press, 1966).

18. I. A. Viktorov, Rayleigh and Lamb Waves (Plenum Press, New York, 1967).
19. W. Franz, Theorie der Beugung Elektromagnetischer Wellen (Springer-Verlag, Berlin, 1957).
20. D. Brill and H. Überall, J. Acoust. Soc. Am. 50, 921-939 (1971).
21. D. Brill, Thesis, The Catholic University of America, Washington, D.C. (1970).
22. B. Rulf, J. Math. Phys. 8, 1785-1793 (1967).
23. H. M. Nussenzveig, Ann. Phys. 34, 23-95 (1965).
24. M. Abramowitz and I. A. Stegun, Handbook of Mathematical Functions (National Bureau of Standards Applied Mathematics Series 55, Washington, D.C., 1964).
25. T. Tamir and L. B. Felsen, IEEE Trans. Antennas Propagation 13, 410-422 (1965).
26. I. S. Gradshteyn and I. M. Ryzhik, Tables of Integrals, Series, and Products (Academic Press, New York, 1965).
- B1. P. M. Morse and H. Feshbach, Methods of Theoretical Physics, Vol. I, (McGraw-Hill Book Co., Inc., New York, 1953).
- B2. K. G. Budden, The Wave-Guide Mode Theory of Wave Propagation, (Prentice-Hall, Englewood Cliffs, New Jersey, 1961).





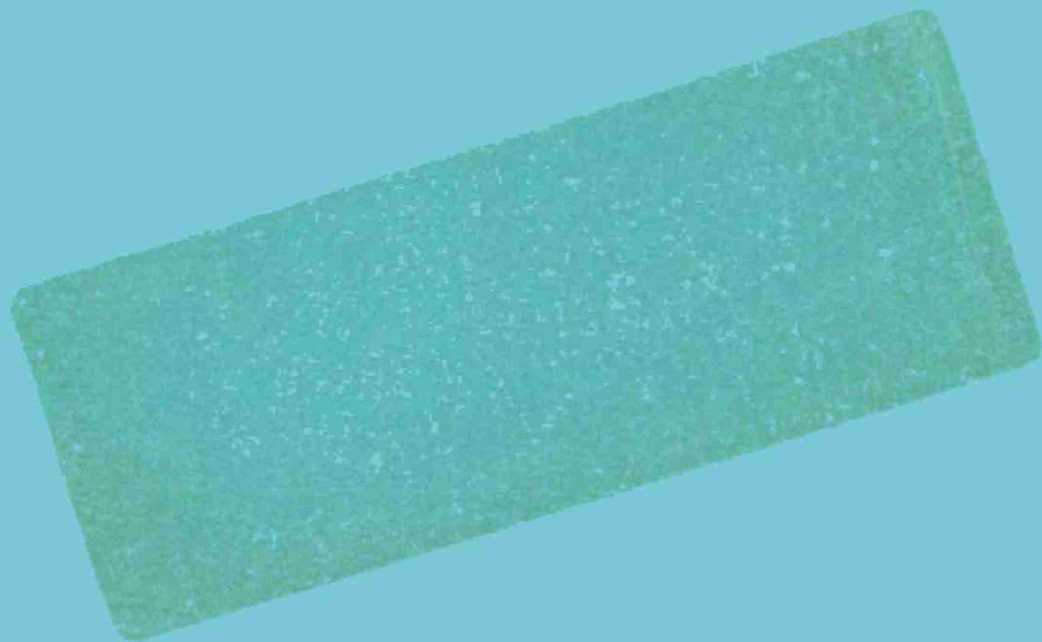
DEPARTMENT OF THE NAVY

NAVAL RESEARCH LABORATORY
Washington, D.C. 20375

OFFICIAL BUSINESS

PENALTY FOR PRIVATE USE, \$300

POSTAGE AND FEES PAID
DEPARTMENT OF THE NAVY
DoD-316



116885